Enhancement of the Dynamic Buckling Load and Analysis of Active Constrained Layer Damping with Extension and Shear Mode Piezoceramic Actuators

Twzen-Shang Geng

Dissertation submitted to the Faculty of the
Virginia Polytechnic Institute and State University
in partial fulfillment of the requirements for the degree of

Doctor of Philosophy
in
Engineering Mechanics

Romesh C. Batra, Chair
Scott L. Hendricks
Michael W. Hyer
Daniel J. Inman
Raymond H. Plaut

April 9, 2002
Blacksburg, Virginia

Keywords: Finite Element Analysis, Buckling Control, Vibration Control, Piezoceramic Actuators, Three-dimensional deformations

Enhancement of the Dynamic Buckling Load and Analysis of Active Constrained Layer Damping with Extension and Shear Mode Piezoceramic Actuators

Twzen-Shang Geng

(ABSTRACT)

We consider geometric and material nonlinearities when studying numerically, by the finite element method, transient three-dimensional electroelastic deformations of a graphite-epoxy square plate sandwiched between two piezoceramic (PZT) layers. Points on the four edges of the bottom surface of the plate are restrained from moving vertically. The two opposite edges of the plate are loaded by equal in-plane compressive loads that increase linearly with time and the other two edges are kept traction free. The plate material is modeled as orthotropic and neoHookean. For the transversely isotropic PZT the second Piola-Kirchhoff stress tensor and the electric displacement are expressed as second degree polynomials in the Green-St. Venant strain tensor and the electric field. Both direct and converse piezoelectric effects are accounted for in the PZT. The plate is taken to have buckled when its centroidal deflection equals three times the plate thickness.

The dynamic buckling load for the plate is found to strongly depend upon the rate of rise of the applied tractions. With the maximum electric field limited to 1kV/mm, the buckling load is enhanced by 18.3% when the PZT elements are activated. For a peak electric field of 30kV/mm, the buckling load increased by 58.5%. When more than 60% of the surface area of the top and the bottom surfaces of the plate are covered by the PZT layers, then square PZT elements placed symmetrically about the plate centroid provide a larger enhancement in the buckling load than rectangular shaped or cross-shaped PZT elements. An increase in the plate thickness relative to

that of the PZT actuators decreases the effectiveness of the PZT in enhancing the buckling load for the plate.

The finite element code was modified to also analyze, in time domain, transient deformations of a viscoelastic material for which the second Piola-Kirchhoff stress tensor is expressed as a linear functional of the strain history of the Green-St. Venant strain tensor. It was used to analyze three-dimensional deformations of a thick laminated plate with layers made of aluminum, a viscoelastic material and a PZT. The following two arrangements of layers are considered. In one case a central PZT layer is surrounded on both sides by viscoelastic layers and aluminum layers are on the outside surfaces. The PZT is poled in the longitudinal direction and an electric field is applied in the thickness direction. Thus shearing deformations of the PZT layer are dominant. In the second arrangement, the aluminum layer is in the middle and the PZT layers are on the outside. The poling direction and the electric field are in the thickness direction; thus its extensional deformations are predominant. Three indices are used to gauge the damping of motion of plate particles, and the effectiveness of PZT actuators in enhancing this damping. It is found that the optimum thickness of the viscoelastic layers for maximum total energy dissipation is the same for each set-up. Also, the total thickness of the PZT layers which results in the maximum value of one of these indices of energy dissipation is the same for the two set-ups. Both arrangements give the largest value of this index for a plate of aspect ratio 10.

Buckling behavior of a sandwich plate containing a soft core is also studied. The effects of the ratio of the elastic moduli of the outer layers to those of the core, and of the core thickness on the buckling load are analyzed. The top and the bottom layers are connected by very stiff blocks on two opposite edges where in-plane compressive time-dependent tractions are applied.

Dedication

To my parents, for their dedication and inspiration

To my brothers and sister, for their belief in me

To my wife and son, for their love and patience

Acknowledgments

I would like to express my gratitude and appreciation to my advisor Dr. Romesh C. Batra for his invaluable guidance and advice throughout my Ph.D. studies. I would also like to thank my committee members Dr. Scott L. Hendricks, Dr. Michael W. Hyer, Dr. Daniel J. Inman, and Dr. Raymond H. Plaut for their support and encouragement. It is an honor to have worked and learned from them.

I would like to thank all the people and friends I have met as part of our group. In particular, I would like to thank Dr. Liang for being the nicest person to deal with and Mr. Hsu-Kuang Ching and Mr. Ravisankar Mattipalli for their friendship. I am also indebted to Mrs. Loretta Tickle for her help in administrative matters and to Mrs. Norma Guynn for her help in typing Chapters 2 and 3 as papers submitted for possible publication to refereed journals. Special thanks are due to my buddies in Chinese Student Association for the enjoyable time we shared together playing basketball and the wonderful time we spent together.

This work was partially supported by the NSF grant CMS9713453 and the ARO grant DAAG55-98-1-0030 to Virginia Polytechnic Institute and State University. I also would like to thank Dr. Edmund G. Henneke and Dr. Don H. Morris for their offering me as a graduate teaching assistantship in the Department of Engineering Science and Mechanics.

Most importantly, I would like to express my deep gratitude and sincere appreciation to my family; my parents for their dedication and inspiration that enabled me to reach this milestone in my life; my brothers and sister, especially my sister Veronica and her husband Dr. Zhu, for their continued

support and belief in me. I am also deeply indebted to my wonderful wife for her love, patience and kindness. It is her continued support and encouragement which kept my belief that there will be an end someday for this work.

Contents

List of Figures

Chapter 1

Introduction

Whereas in the past material systems and structures were designed based on their passive response to applied loads, recently, the construction and operation of space structures have generated an interest in using piezoelectric materials and shape memory alloys to form "smart" structures. Some of the piezoceramics (PZT*s) attached to a structure can be used as sensors and others as actuators to control their deformations and/or to produce a desired response. The shape memory alloy actuators can generate actuation strains of 8% when energized by a relatively low energy and the PZT actuators generally require high electric fields to produce noticeable actuation strains. However, the response time of a PZT is in microseconds, and that of SMA actuators is much larger than that of a PZT.

The piezoelectric phenomenon was discovered by the Curie brothers in 1880 [58]. They found that stresses applied on certain materials were accompanied by the production of electric surface charge, which we call direct piezoelectric effect today. The following year, Lippmann [58], using thermodynamic principles, predicted the converse piezoelectric effect: an imposed voltage produces mechanical deformations. Here we investigate the use of PZTs in enhancing the dynamic buckling load of a homogeneous orthotropic elastic plate. The plate's material is modeled as neo-Hookean and that of the PZT by a constitutive relation that expresses the second Piola-Kirchhoff

*The abbreviation PZT is used to denote a generic piezoceramic material rather than a specific one.

stress tensor as a second degree polynomial in the electric field and the Green-St. Venant strain tensor, e.g. see Yang and Batra [1]. Thus the effect of large electric fields applied to the PZT elements can be adequately modeled. The motivation for this is provided by the experimental work of Crawley and Anderson [2] who observed a nonlinear relationship between the applied voltage and the normal strain induced in an unconstrained PZT plate for electric fields exceeding 100 V/mm. We use the three-dimensional theory and account for the effect of inertia forces, geometric nonlinearities (nonlinear strain-displacement relations) and material nonlinearities in ascertaining the buckling load of a rectangular plate. The plate is loaded on two opposite edges by axial loads that increase linearly with time while the other two edges are traction free. The problem is analyzed by the finite element method with the computer code developed by Batra and Liang [3].

The flexural rigidity of a plate and hence its buckling load can be passively increased by adding stiffeners to it. However, situations such as aesthetics, limited availability of space, packaging requirements, interference with other structural components or weight may restrict the use of stiffeners. In these cases, it may be more beneficial and sometimes absolutely necessary to resort to active methods, such as the one studied here, to enhance the buckling load for the plate.

Previous work on the enhancement of the buckling load of an elastic rectangular plate by using PZT elements includes that of Chandrashekhara and Bhatia [4], Murali Krishna and Mei [5], and Thompson and Griffin [6]. Chandrashekhara and Bhatia [4] used the first-order shear deformation theory, linear kinematics, linear constitutive relations for the PZT and the material of the plate and assumed that the plate buckles when its centroidal transverse deflection equals the plate's thickness. The axial loads applied on two opposite edges of the plate were taken to increase linearly with time. Their numerical results computed for a square thin plate with the length/thickness ratio of 100 showed that the actuation of the PZT elements increased the buckling load by 4.6%. Murali Krishna and Mei [5] also used the finite element method to analyze the problem but employed the von Karman large deflection plate theory and the PZT and the PVDF (PolyVinylidene Flouride Film) actuators. They showed that the voltage to be applied to the PZT elements in order to buckle the plate with all four edges clamped was higher than that required when all edges were simply supported. Thompson and Griffin [6] employed titanium-nickel shape memory alloy (SMA) ac-

tuators to control the buckling of a stiffened aluminum plate. They used the commercial code ABAQUS, modeled the structure by plate/shell elements and the actuators by beam elements. The change in the buckling load was found to be almost proportional to the magnitude of the actuation level, and an 8% strain in the SMA actuators enhanced the buckling load by 14%.

Baz and Tempe [7] have designed a closed-loop computer-controlled system employing a titanium-nickel SMA helical spring to increase the buckling load of a long slender beam loaded by an axial compressive load at the rate of 0.0917 N/s. Thompson and Laughlan [8] experimentally showed that the buckling load of graphite-epoxy strips can be increased from 19.8% to 37.1% by using PZT actuators. DeFaria and deAlmeida [9] employed the von Karman nonlinear strain-displacement relations and linear constitutive relations for both the PZT and the beam material. They developed a strategy to exploit the PZT actuation so that the response of a slightly crooked beam is very close to that of a perfect beam. Berlin and Sussman [10] stabilized the first buckling mode through the use of tendons. Meressi and Paden [11] analytically proved that PVDF actuators mounted continuously along the length of a column could be used to stabilize the first mode of the column. Jefferis [12] used an electromagnet to achieve the same goal. Berlin [13] demonstrated the use of induced-strain actuation to control the buckling of a thin steel column and thereby achieved an increase of 5.6 times in the load bearing capacity of the column. Berlin et al. [14] have also established the effectiveness of networked arrays of MEMS-based sensors and filamentary PZT actuators to control the buckling instability of a column for loads up to 2.94 times the critical buckling load.

In contrast to the dynamic buckling problem studied here in which the applied axial loads increase linearly with time, other investigators (e.g. see [15]) have considered axial impulses of finite duration applied to the edges of the plate. Typically, the axial velocity or the axial load in the form of a half sine wave is considered. The amplitude and the time period of the sine wave are varied till the plate buckles. The dynamic buckling load is determined by adopting the stability criterion of Budiansky and Hutchinson [13] according to which the structure is unstable if one of the characteristic values associated with its deformations increases rapidly with the amplitude of the applied load. Cui et al. [17] determined the deflection of a rectangular elastic-plastic plate

loaded by axial loads of fixed duration and defined the buckling load as the one for which the slope of the deflection vs. the load curve suddenly increased. These authors also give a brief historical perspective of the dynamic buckling of plates.

Dynamic loads can rarely be represented by a half sine wave or a half rectangular wave of short duration; they usually increase suddenly and then slowly die out. Here we assume that the applied load increases linearly with time and the plate buckles during the time the load is increasing.

Results presented herein show that PZT elements bonded to the top and the bottom surfaces of a rectangular plate when suitably activated can enhance the buckling load of a graphite-epoxy plate by 58.5%.

We now briefly review the literature on constrained layer damping treatments. Several investigators (e.g. Azvine et al. [24], Baz [28], Baz and Ro ([30-33]), Edberg and Bicos [38], Plump and Hubbard [43], Shen [44], Van Nostrand et al. [49] have analyzed Active Constrained Layer Damping (ACLD) treatments for quickly annulling vibrations of a structure. The energy dissipated per unit volume of the viscoelastic material is usually higher in the ACLD treatment than that in the Passive Constrained Layer Damping (PCLD) treatment. Usually an ACLD treatment consists of a viscoelastic layer with one face bonded to the host structure and the other to a PZT layer. Deformations of the PZT layer are controlled by applying a suitable voltage difference across its faces which in turn enhances shear deformations of the viscoelastic layer. In a PCLD treatment, there is no actuator to enhance shearing deformations of the viscoelastic layer either embedded in the host structure or bonded to its outer surface. Ideally, the damping treatment should dissipate energy efficiently but not noticeably alter the dynamic characteristics of the host structure.

We note that Van Nostrand [49] concluded that active actions will be degraded by the passive constraining layer. Bailey et al. [25] stated that it is more effective to apply piezoelectric materials directly on the structure rather than embed a viscoelastic layer between the two. Liao and Wang [41] have shown that a viscoelastic layer reduces the transmissibility and hence the direct control authority from the active source to the host structure. They [42] have identified ranges of viscoelastic material properties which will provide satisfactory transmissibility of active actions, and

the overall performance will exceed that of purely passive and active systems.

Previous studies of ACLD treatments have employed extension mode PZT actuators in which the electric field and the poling direction are along the thickness of the PZT layer. The thickness of the PZT changes and the transverse displacements induced due to the Poisson effect in the PZT increase shear deformations of the viscoelastic layer. Alternatively, one could exploit shear mode deformations of the PZT in which it is poled in a longitudinal direction and the electric field is applied across its thickness. Note that different piezoelectric constants are effective in the extension and in the shear mode actuation. Shear mode PZTs are commercially available[†] and were studied by Sun and Zhang [46] and Zhang and Sun [57] for controlling deformations of a laminated structure. Vel and Batra ([50], [51]) have given exact solutions for static deformations of simply supported laminated structures incorporating shear mode actuators; closed-form solutions for shear mode PZT beams were given by Boriseiko et al. [33]. Here we compare their effectiveness in ACLD treatments with that of extension mode actuators. As pointed out by Sun and Zhang [46] an advantage of shear mode actuators is that for the same tip deflection the maximum bending stress induced in them is less than that in the extension mode actuators; it was also verified by the analytical solutions of Vel and Batra ([52], [53]). Also, they are embedded within the structure and hence are not exposed to environmental effects.

Analysis of dynamic problems involving ACLD treatments requires a mathematical model (i.e. governing equations, and initial and boundary conditions) of the system. Such problems have been studied by the finite element method (e.g. see Baz and Ro ([31], [32]), Van Nostrand et al. [49]) or by distributed-parameter methods (e.g. see Azvine et al. [24], Baz [28], Baz and Ro ([29], [30]), Plump and Hubbard [43], Shen [44]) which employ shear models of Mead and Markus [39] and DiTaranto [37]. Nearly all of these studies are limited to beam like structures and therefore make kinematic assumptions of the beam theory. On the contrary we study here three-dimensional deformations of very thick clamped plates/beams and account for geometric nonlinearities. Furthermore, the constitutive relation for the PZT has second-order terms in the electric field to incorporate nonlinear dependence of strains upon the electric field observed by

[†]Electro Ceramic Div., Morgan Matroe, Bedford, OH.

Crawley and Anderson [36]. However, temperature dependence of the material properties and heat generated due to viscous dissipation and the electric field have not been considered. Thus the temperature is assumed to be constant throughout the deformation process.

Sandwich construction consists of two flat sheets firmly attached to a core. For its high bending stiffness and high strength to weight ratio, sandwich construction has been successfully used in aviation and aerospace industries, marine, and mechanical and civil engineering applications. There are two kinds of sandwich constructions: truss-core and soft core. Lok and Cheng [59] used an equivalent 2-D, homogeneous, orthotropic, thick-plate continuum to represent the dynamic flexural behavior of a 3-D, thin-walled truss-core sandwich panel. They derived a closed-form solution to study the free and forced vibration response of the sandwich panel. For a soft core sandwich plate, Hao et al. [60] modeled the sandwich construction as a three-dimensional solid body. They showed that the model that smears the facesheets and the core overestimates the initial buckling load and predicts unstable postbuckling behavior. Sokolinsky and Frostig [61] studied the effect of boundary conditions on the critical load and the corresponding mode shape of sandwich panels with a soft core. They showed that the core properties affect the buckling load and the corresponding modes of the panel in such a way that the structures with identical boundary conditions but with different cores may undergo different types of buckling such as overall and local as well as interactive loss of stability. Frostig and Sokolinsky [62] studied buckling behavior of sandwich panels with a transversely flexible core that are debonded at one of their face sheet-core interfaces. They showed the effects of the length and the location of the delamination, face sheet rigidities, boundary conditions, and the existence or the nonexistence of the contact on the critical loads and buckling modes. However, the effects of the ratio of the elastic moduli of the outer panels to those of the core and of core thickness on the uncoupling of deformations of the two outer layers have not been investigated. We have focused on investigating these effects.

Chapter 2

Enhancement of the Dynamic Buckling Load for a Plate by using Piezoceramic Actuators *

2.1 Formulation of the Problem

We use rectangular Cartesian coordinates to describe the transient electromechanical finite deformations of a system consisting of a plate with PZT elements perfectly bonded to its top and bottom surfaces; a schematic sketch of the problem studied is shown in Fig. 2.1. In the referential description of motion and in the absence of body forces and distributed charges, equations governing these deformations are

$$T_{iL,L} = \rho_0 \ddot{u}_M \delta_{iM},\ i = 1,2,3;\ L = 1,2,3, \tag{2.1}$$

$$D_{L,L} = 0. \tag{2.2}$$

*A slightly different version of this chapter has appeared in **Smart Materials and Structures**, Vol.10(5), pp. 925-933, 2001.

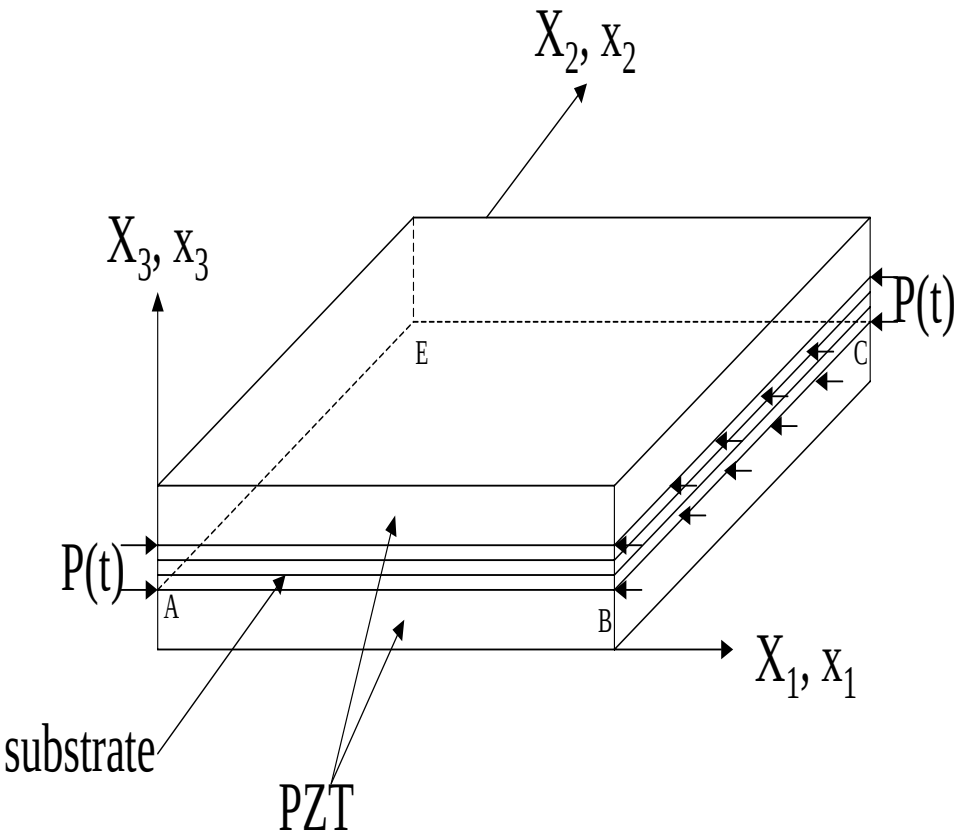

Figure 2.1: Schematic sketch of the problem studied.

Here T_{iL} is the first Piola-Kirchhoff stress tensor sometimes also called the nominal or the engineering stress tensor, ρ_0 is the mass density in the reference configuration, u_M the displacement of a point, D_L the electric displacement, a superimposed dot indicates the material time derivative, δ_{iL} is the Kronecker delta, and a comma followed by an index L signifies partial differentiation with respect to the position X_L occupied by a material point in the reference configuration. A repeated index implies summation over the range of the index. The lower and upper case indices denote the component of a tensor with respect to coordinates in the present and the reference configurations respectively. Equation (2.1) expresses the balance of linear momentum in the absence of body forces, and equation (2.2) the balance of electric charges when there are no distributed charges present. However, as is usually done, the inertia term associated with the balance of electric charge has been neglected. Because we have used the referential description of motion, the equation expressing the balance of mass is not needed to find the displacements of a point; it will be required if the present mass density is to be determined.

Balance laws (2.1) and (2.2) are to be supplemented by constitutive relations. The material of the plate is assumed to be homogeneous and orthotropic and is modeled as neo-Hookean. That is

$$S_{LM} = C_{LMPQ} E_{PQ} \tag{2.3}$$

where $\mathbf{S}$ is the second Piola-Kirchhoff stress tensor, $\mathbf{E}$ the Green-St. Venant strain tensor, and $\mathbf{C}$ the fourth-order elasticity tensor with 9 independent components for an orthotropic material. Since $S_{LM} = S_{ML}$ and $E_{PQ} = E_{QP}$, each can be expressed as a six-dimensional vector. In this notation, $\mathbf{C}$ will be a 6×6 symmetric matrix. Batra [18] has compared the response predicted by four linear constitutive relations like equation (2.3) for finite deformations of isotropic elastic materials. He showed that the analogue of constitutive relation (2.3) for isotropic materials predicts a stiffening behavior. That is, in simple extensional and shearing deformations, the tangent modulus increases with an increase in a measure of the deformation. For the problems studied herein, this stiffening of the material is negligible because the maximum strain induced in the structure is less than 11%. The PZT is modeled as a homogeneous transversely isotropic material with the axis of transverse

isotropy along the unit vector $\mathbf{a}$. We anticipate applying large electric fields $\mathbf{W}$ to it along the direction $\mathbf{a}$. Thus we incorporate second-order terms in $\mathbf{E}$ and $\mathbf{W}$ in its constitutive relation. Yang and Batra [1] have derived the following second-order constitutive relations for a PZT that is stress free in the reference configuration.

$$\begin{aligned}\mathbf{S} = &(2c_1I_1 + c_3I_2 + e_1I_3 + 3\lambda_1I_1^2 + 2\lambda_3I_1I_2 + \lambda_4I_2^2 + \lambda_5II_1 + \lambda_7II_2 + 2\nu_1I_1I_3 + \nu_2I_3^2\\ &+ \nu_7II_3 + \nu_9II_4 + \nu_{14}I_2I_3)\mathbf{a}\otimes\mathbf{a} + (2c_2I_2 + c_3I_1 + e_2I_3 + 3\lambda_2I_2^2 + \lambda_3I_1^2\\ &+ 2\lambda_4I_1I_2 + \lambda_6II_1 + \lambda_8II_2 + 2\nu_2I_2I_3 + \nu_4I_3^2 + \nu_8II_3\\ &+ \nu_{10}II_4 + \nu_{14}I_1I_3)\mathbf{1} + (c_4 + \lambda_5I_1 + \lambda_6I_2 + \nu_5I_3)(\mathbf{a}\otimes\mathbf{E}\cdot\mathbf{a} + \mathbf{a}\cdot\mathbf{E}\otimes\mathbf{a})\\ &+ 2(c_5 + \lambda_7I_1 + \lambda_8I_2 + \nu_8I_3)\mathbf{E} + (e_3 + \nu_9I_1 + \nu_{10}I_2 + \nu_{11}I_3)(\mathbf{a}\otimes\mathbf{W} + \mathbf{W}\otimes\mathbf{a})\\ &+ 3\lambda_9\mathbf{E}^2 + \nu_{12}\mathbf{W}\otimes\mathbf{W} + \nu_{13}(\mathbf{a}\otimes\mathbf{E}\cdot\mathbf{W} + \mathbf{W}\cdot\mathbf{E}\otimes\mathbf{a} + \mathbf{W}\otimes\mathbf{E}\cdot\mathbf{a} + \mathbf{a}\cdot\mathbf{E}\otimes\mathbf{W}),\end{aligned}$$

$$\begin{aligned}-\boldsymbol{\pi} = &(2\epsilon_1I_3 + e_1I_1 + e_2I_2 + 3\mu_1I_3^2 + \mu_2II_3 + \nu_1I_1^2 + 2\nu_2I_3I_1 + \nu_3I_2^2 + 2\nu_4I_3I_2\\ &+ \nu_5II_1 + \nu_6II_2 + \nu_{11}II_4 + \nu_{14}I_1I_2)\mathbf{a} + 2(\epsilon_2 + \mu_2I_3 + \nu_7I_1 + \nu_8I_2)\mathbf{W}\\ &+ 2(e_3 + \nu_9I_1 + \nu_{10}I_2 + \nu_{11}I_3)\mathbf{E}\cdot\mathbf{a} + 2\nu_{12}\mathbf{E}\cdot\mathbf{W} + 2\nu_{13}\mathbf{E}^2\cdot\mathbf{a},\end{aligned} \tag{2.4}$$

where

$$\begin{aligned}&I_1 = \mathbf{a}\cdot\mathbf{E}\mathbf{a}, \quad I_2 = \operatorname{tr}\mathbf{E}, \quad I_3 = \mathbf{a}\cdot\mathbf{W}, \quad II_1 = \mathbf{a}\cdot\mathbf{E}^2\mathbf{a},\\ &II_2 = \operatorname{tr}\mathbf{E}^2, \quad II_3 = \mathbf{W}\cdot\mathbf{W}, \quad II_4 = \mathbf{a}\cdot\mathbf{E}\mathbf{W} + \mathbf{W}\cdot\mathbf{E}\mathbf{a}.\end{aligned} \tag{2.5}$$

Here $\boldsymbol{\pi}$ is the polarization vector that is related to the electric displacement $\mathbf{D}$, the electric field $\mathbf{W}$ and the electric potential ϕ through

$$\pi_L = D_L - \varepsilon_0 J X_{L,i} X_{K,i} W_K,\ W_K = -\phi_{,K}\ , \tag{2.6}$$

where ε_0 is the permittivity of the free space, $J = \det(x_{i,K})$, $\mathbf{x}$ is the present position of the

material point that occupied place $\mathbf{X}$ in the reference configuration, and a comma followed by index i denotes partial differentiation with respect to x_i. Furthermore, in equations (2.4) and (2.5), $\mathbf{1}$ is the identity tensor, $c_1, \ldots, c_5,\ \lambda_1, \ldots, \lambda_8$, $\nu_1, \ldots, \nu_{14}$, e_1, e_2, e_3, μ_1 and μ_2 are material constants, $\mathbf{a} \cdot \mathbf{b}$ denotes the inner product between vectors $\mathbf{a}$ and $\mathbf{b}$, and the tensor product, $\mathbf{a} \otimes \mathbf{b}$, between them is defined as $(\mathbf{a} \otimes \mathbf{b})\mathbf{c} = (\mathbf{b} \cdot \mathbf{c})\mathbf{a}$ for every vector $\mathbf{c}$. The neo-Hookean relation for the PZT is obtained from equations (2.4) and (2.5) by keeping terms linear in $\mathbf{E}$ and $\mathbf{W}$. We note that Batra and Yang [19] have also derived second order constitutive relations for porous PZT materials.

Tensors $\mathbf{S}$ and $\mathbf{T}$ are related to each other through

$$T_{iK} = x_{i,L} S_{KL}, \tag{2.7}$$

and to the Cauchy or the true stress tensor $\boldsymbol{\sigma}$ by

$$\sigma_{ij} = J^{-1} x_{i,L} x_{j,M} S_{LM}\,. \tag{2.8}$$

The Green-St. Venant strain tensor, $\mathbf{E}$, is expressed in terms of the mechanical displacements $\mathbf{u} = \mathbf{x} - \mathbf{X}$ as follows.

$$E_{KL} = (u_{K,L} + u_{L,K} + u_{M,K} u_{M,L})/2. \tag{2.9}$$

We note that the classical infinitesimal theory follows from equations (2.1) through (2.9) by neglecting in them the contributions from the second-order terms in $u_{M,K}$ and W_K. In the linear theory, the three stress tensors $\mathbf{S},\ \mathbf{T}$ and $\boldsymbol{\sigma}$ coincide with each other.

The perfect bonding condition at the common interface Γ_{int} between the PZT and the plate can be stated as

$$[u_K] = 0,\ [T_{iL}]N_L = 0,\ [\phi] = 0,\ [D_L]N_L = 0 \text{ at } \Gamma_{\text{int}} \tag{2.10}$$

where $\mathbf{N}$ is a unit normal to Γ_{int}, and $[f]$ denotes the jump in the values of f across the interface.

Equations (2.10) imply that the mechanical displacements, surface tractions, the electric potential and the normal component of the electric displacement are continuous across the common interface Γ_{int}.

The plate and the PZT particles are assumed to be initially at rest and stress free in the reference configuration. Thus initial displacements and velocities of all material particles are zeroes. With reference to the schematic sketch and the coordinate axes depicted in Fig. 2.1, the boundary conditions can be stated as follows:

$$
\begin{aligned}
&T_{i1} = -p(t)\delta_{i1} && \text{on plate surfaces } X_1 = 0, L_1,\\
&T_{i2} = 0 && \text{on plate surfaces } X_2 = 0, L_2,\\
&u_3 = 0 && \text{at points on lines } AB,\ BC,\ CE \text{ and } EA \text{ of the plate},\\
&D_L N_L = 0 && \text{on the plate and PZT surfaces } X_1 = 0, L_1, \text{ and } X_2 = 0, L_2,\\
&\phi = 0 && \text{on the PZT surfaces bonded to the plate},\\
&\phi = \phi_a && \text{on the top surface of the upper PZT layer},\\
&\phi = \phi_b && \text{on the bottom surface of the lower PZT layer}.
\end{aligned}
\tag{2.11}
$$

That is, the square plate is supported on edges $AB,\ BC,\ CE$ and EA, and is loaded on the two opposite edge surfaces by in-plane time dependent axial compressive loads with the other two edge surfaces of the plate free of in-plane tractions. The surfaces of the plate bonded to the PZTs are electroded with electrodes of negligible thickness. All surfaces, except where electric potentials are prescribed, are electrically insulated. Note that at points on lines AB and CE, the displacement in the X_3-direction and surface tractions in the X_1 and X_2 directions vanish. At points on lines BC and EA, the displacement in the X_3 direction and surface tractions in the X_2 direction vanish.

2.2 Numerical Solution and Discussion of Results

The aforestated problem is solved numerically by using the finite element method. The domain occupied by the plate and the PZT layers is divided into the union of disjoint 8-node brick elements. Following the procedure used to derive the Galerkin formulation of the problem, e.g., see Hughes [20], we obtain from equations (2.1) and (2.2) the following set of coupled nonlinear ordinary differential-algebraic equations.

$$\begin{aligned} &\mathbf{M}\ddot{\mathbf{d}} = \mathbf{F}^{\text{ext}}(t) - \mathbf{F}^{\text{int}}(\mathbf{d}(t), \phi(t)), \\ &\mathbf{P}_{\text{int}}(\mathbf{d}(t),\ \phi(t)) = \mathbf{P}_{\text{ext}}(t). \end{aligned} \tag{2.12}$$

Here $\mathbf{M}$ is the mass matrix, $\mathbf{d}$ the vector of nodal mechanical displacements in both the plate and the PZT layers, ϕ the vector of nodal electric potentials in PZT elements only, $\mathbf{F}^{\text{ext}}$ and $\mathbf{F}^{\text{int}}$ are vectors of nodal forces equivalent respectively to externally applied surface tractions and internal stresses and electric fields developed in the body at time t, $\mathbf{P}_{\text{int}}$ is the nodal charge vector equivalent to the internal polarization in PZT elements, and $\mathbf{P}_{\text{ext}}$ is the externally applied nodal charge vector. A finite element code based on equations (2.12) has been developed and validated by Batra and Liang [3]. It uses the $2 \times 2 \times 2$ integration rule to evaluate the element mass matrix and the element load vectors. The mass matrix is lumped by using the row-sum technique. Equation $(2.12)_1$ is solved by the central-difference method which is explicit, conditionally stable, and for linear one-dimensional problems gives exact time periods for the waves. After every time step, the nonlinear equations $(2.12)_1$ are discretized and we set

$$\Delta t = 1.8/\omega_{\max}\ . \tag{2.13}$$

The maximum frequency, $\omega_{\max}$, of the discretized structure is computed after every time step. Within each time step, the nonlinear algebraic equations $(2.12)_2$ are solved by the Newton-Raphson iterative method.

Recalling that the size of the time step varies as the solution evolves, we used the following relation

(2.14) to compute nodal displacements at time t_{n+1} from a knowledge of their values at times t_{n-1} and t_n.

$$\mathbf{d}(t_{n+1}) = \Delta t_2 \mathbf{M}^{-1}\left[(\mathbf{F}^{\text{ext}}(t_{n+1}) - \mathbf{F}^{\text{int}}(t_{n-1}))\frac{\Delta t_1 + \Delta t_2}{2} + \left(\frac{1}{\Delta t_1} + \frac{1}{\Delta t_2}\right)\mathbf{d}(t_n) + \frac{\mathbf{d}(t_{n-1})}{\Delta t_1}\right] . \tag{2.14}$$

Here $\Delta t_1 = t_n - t_{n-1}$ and $\Delta t_2 = t_{n+1} - t_n$. Values of $\mathbf{d}(-\Delta t_1)$ are found from those of $\mathbf{d}(0)$, $\dot{\mathbf{d}}(0)$ and $\ddot{\mathbf{d}}(0)$, by using a one-step method with $\ddot{\mathbf{d}}(0)$ computed from equation $(2.12)_1$. We used Batra and Liang's [3] finite element code to study the buckling problem.

2.2.1 Buckling of a Column

In an attempt to delineate the difference in the buckling loads under quasistatic and dynamic deformations, and to establish our methodology of determining the buckling load in transient deformations, we first study the problem for a slender column. The $40\text{mm} \times 1\text{mm} \times 1\text{mm}$ steel column modeled as an isotropic material with Young's modulus $E = 200$ GPa, the shear modulus $G = 79$ GPa, and the mass density $\rho = 7860$ kg/m^3 is loaded only on the top and bottom surfaces by equal and opposite axial compressive tractions that increase linearly with time t. The column was divided into 40 uniform cubic elements along its length. The initial shape of the column was taken to be a half sine wave with amplitude equal to 1% of the thickness of the column. The axial load applied at the ends of the column was assumed to increase linearly with the time t. The Euler buckling load for static deformations of the steel column is 25.7N. For the dynamic problem, the column was assumed to buckle when the lateral deflection at the midspan equaled three times the width of the column, or 3 mm for the problem being studied. As shown below in Table 1, the buckling load computed according to this criterion was found to strongly depend upon the rate of rise of the axial load.

Table 1. Dependence of the buckling load for a pinned-pinned column upon the loading rate.

Loading rate (kN/s)	Buckling load (N)	Dynamic load amplification factor (DLAF)
1000	220.8	8.59
200	89.6	3.49
100	66.6	2.59
20	43.4	1.69

The DLAF [21] equals the buckling load under dynamic loading divided by the Euler buckling load under quasistatic conditions. The computed results clearly indicate that the DLAF decreases with a decrease in the rate of loading. In order to assess the effect of inertia forces on the DLAF, we artificially reduced the mass density of the column's material to 786 kg/m^3, i.e., to 10% of its true value. In this case, loading rates of $10^6,\ 2\times10^5,\ 10^5$ and 2×10^4 N/s resulted in DLAFs of 4.42, 2.21, 1.84 and 1.56 respectively. Thus the DLAF decreases monotonically as the effect of inertia forces is diminished, and our criterion to ascertain the dynamic buckling load is reasonable. Because of the geometric nonlinearities considered, the buckling load for quasistatic loading need not equal the Euler buckling load.

2.2.2 Buckling of an Orthotropic Plate

In the second example problem, a square graphite-epoxy plate of side 10 mm and thickness 0.25 mm with fibers oriented parallel to the X_1-axis was divided into $20\times20\times2$ uniform elements. The values of nonvanishing elastic moduli are

$$C_{1111}=152.35\ \text{GPa},\ C_{2222}=C_{3333}=9.99\ \text{GPa},\ C_{2323}=C_{1313}=7.1\ \text{GPa},$$

$$C_{1122} = C_{1133} = 3.92\,\text{GPa},\ C_{2233} = 3.07\,\text{GPa},\ C_{1212} = 2.5\,\text{GPa},$$

and the mass density, ρ, equaled 1600 kg/m^3. For infinitesimal deformations, these correspond to

$$E_1 = 150\,\text{GPa},\ E_2 = E_3 = 9\,\text{GPa},\ \tilde{\nu}_{12} = \tilde{\nu}_{23} = \tilde{\nu}_{31} = 0.3,$$
$$G_{12} = G_{31} = 7.1\,\text{GPa},\ G_{23} = 2.5\,\text{GPa}.$$

Here E_1 equals Young's modulus in the direction of the fibers, $E_2,\ E_3$ Young's moduli in the transverse directions, $G_{12},\ G_{23},\ G_{31}$ shear moduli and $\tilde{\nu}_{12},\ \tilde{\nu}_{23},\ \tilde{\nu}_{31}$ Poisson's ratios. For the simply supported plate loaded only on the edge surfaces $X_1 = 0$, 10 mm by uniformly distributed axial compressive forces along the X_1-direction, the classical plate theory gives a buckling load of 23,064 N/m; e.g. see Jones [22]. In the numerical solution of the problem by the finite element method, the initial shape of the midsurface of the plate in the X_1 and X_2 directions was taken to be a half sinusoidal curve with an amplitude equal to 0.33% of the plate's thickness. The plate was assumed to have buckled when the transverse displacement (i.e. the displacement in the X_3 direction) equaled three times its thickness. For loading rates of 3.2×10^7 and 1.6×10^7 N/m/s, the buckling loads were found to be 38,500 and 32,400 N/m respectively which resulted in the DLAFs of 1.67 and 1.41.

2.2.3 Enhancement of the Dynamic Buckling Load for a Plate with PZT Elements

For the square graphite-epoxy plate described in Section 2.2.2, we now investigate the increase in the buckling load caused by the bonding of 0.125 mm thick PZT-G1195 actuators to its top and bottom surfaces; cf. Fig. 2.1. The PZT layers are poled in the X_3-direction. The attachment of the PZT layers to the graphite-epoxy plate will alter the buckling load. Nonzero values assigned to

material parameters for the PZT-G1195 are listed below (see Tiersten [22]).

$$
\begin{aligned}
&c_1 = 29\,\mathrm{GPa},\ c_2 = 38.1\,\mathrm{GPa},\ c_3 = -2\,\mathrm{GPa},\ c_4 = -21\,\mathrm{GPa},\ c_5 = 35.9\,\mathrm{GPa},\\
&e_1 = 13.4757\,\mathrm{C/m^2},\ e_2 = -39.8583\,\mathrm{C/m^2},\ \rho = 7,500\,\mathrm{kg/m^3},\\
&\nu_4 = -90.3\times 10^{-6}\,\mathrm{N/V^2},\ \nu_{12} = 30.54\times 10^{-6}\,\mathrm{N/V^2},\\
&\epsilon_0 = 8.8419\times 10^{-12}\,\mathrm{N/V^2},\ \epsilon_1 = 1.081\times 10^{-9}\,\mathrm{N/V^2},\ \epsilon_2 = -2.22558\times 10^{-9}\,\mathrm{N/V^2}.
\end{aligned}
\tag{2.15}
$$

With these values of material parameters, constitutive relations (2.4) for the PZT contain second-order terms in the electric field $\mathbf{W}$ but only first-order terms in the Green-St. Venant strain tensor $\mathbf{E}$. There is no test data available to find values of other material parameters. As shown in Fig. 2.1, uniformly distributed axial tractions are applied on the edge surfaces $X_1 = 0,\ 10\,\mathrm{mm}$ of the graphite-epoxy plate. Because of the symmetry of the plate and the loading conditions about the centroidal axes of the plate that are parallel to X_1 and X_2-axes, only a quarter of the plate was analyzed. The quarter of the graphite-epoxy plate was divided into uniform brick elements of size $0.5\times 0.5\times 0.042$ mm, and each one of the two PZT layers into uniform brick elements of size $0.5\times 0.5\times 0.125$ mm. A finer mesh could not be used because of the excessive CPU time required to reach the buckled state of the plate. A typical time step size used was 10^{-8}s and the plate buckled at $t \simeq 3\times 10^{-4}$s. The initial shape of the plate was assumed to be sinusoidal in both X_1 and X_2 directions as described in Section 2.2.2. For the loading rate of $1,600\mathrm{GN/m/s}$ and no voltage applied to the PZTs, the following Table 2 lists the computed buckling load for the graphite/epoxy plate with the two PZT layers.

Table 2. Dependence upon the initial imperfection of the buckling load for the graphite-epoxy plate with PZT layers affixed to its top and bottom surfaces and loaded at the rate of 1,600 GN/m/s.

$\frac{\text{Initial centroidal deflection}}{\text{plate thickness}} \times 100$	Dynamic Buckling Load kN/m
0.33	403.6
0.66	387.6
1.0	377.8
1.33	360.6

For the amplitude of the initial sinusoidal shape of the plate equal to 0.166% of the plate thickness, the plate buckled with the centroidal deflection in a direction opposite to that of the initial shape of the plate. In the results presented below, the amplitude of the initial sinusoidal shape of the plate was set at 0.33% of the plate thickness. We note that within the buckled plate, the maximum principal strain and the maximum shear strain at any point were computed to be 7% and 11% respectively. Thus a neo-Hookean material model for the plate should give acceptable results.

At the loading rate of 1,600 GN/m/s, the inertia effects will play a significant role. Also, the CPU time required to determine the buckling load is less at such high loading rates since the time step size is determined by the time taken for an elastic wave to travel through the smallest element in the mesh. Since our goal is to establish the enhancement of the buckling load by using PZT actuators, the value of the loading rate will not affect much the percentage gain achieved by using the PZT actuators.

When a uniform electric potential ϕ_a of 10, 20 and 30 volts was applied only to the upper surface of the PZT layer bonded to the grounded top surface of the graphite-epoxy plate, the buckling load increased to 415.3kN/m, 456kN/m, and 403.8kN/m respectively. These represent an improve-

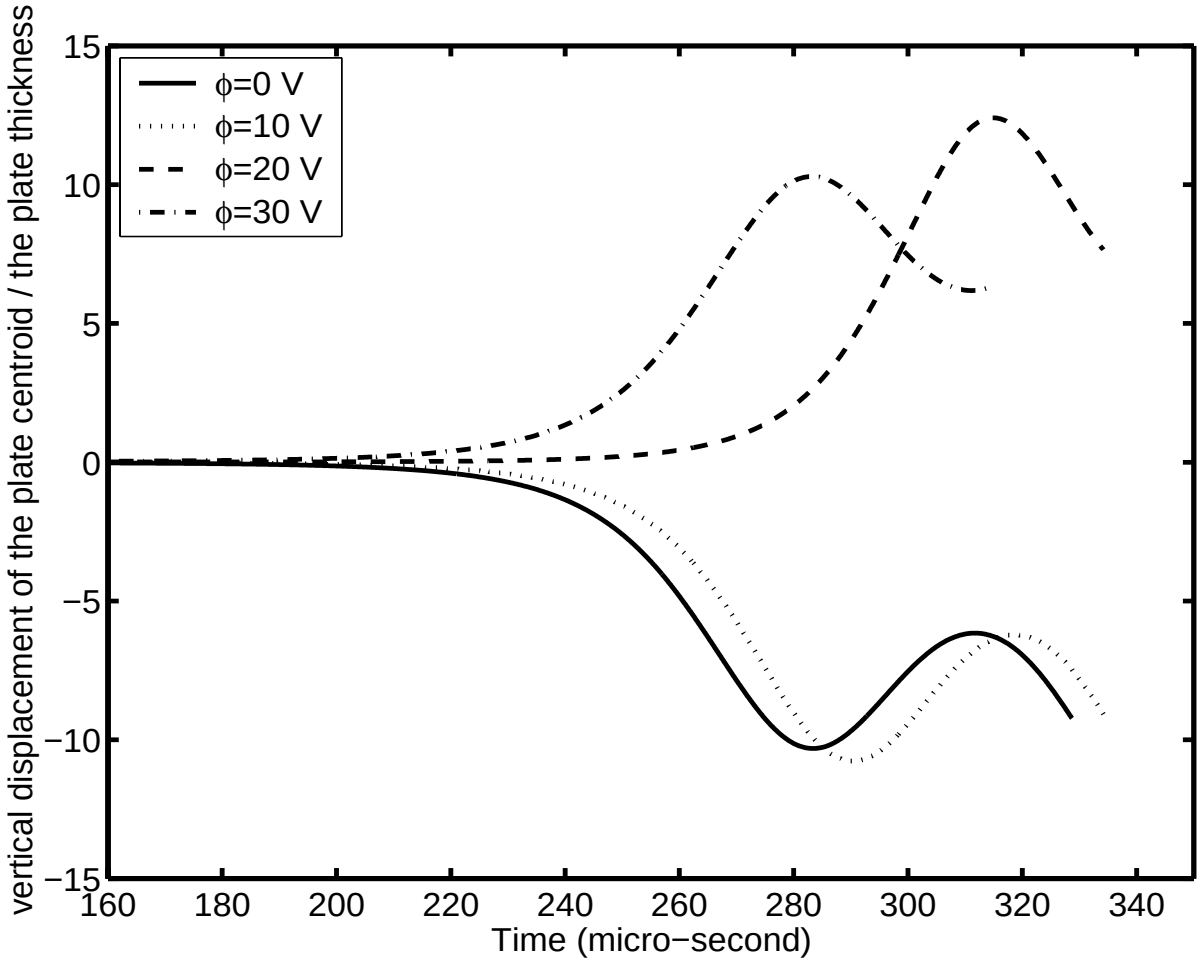

Figure 2.2: Time history of the deflection of the centroid of the axially loaded square graphite-epoxy plate when a voltage of 10, 20 and 30 volts is applied to the upper surface of the PZT layer bonded to the top grounded surface of the plate.

ment of 2.95%, 12.99% and 0.05% over that for the no actuation case. Figure 2.2 depicts the time history of the deflection of the centroid of the graphite-epoxy plate for the four cases studied. It is clear that for $\phi_a = 20V$ and $30V$, the centroid of the plate deflects in a direction opposite to that when $\phi_a = 0$ and $10V$. This exercise suggests that increasing the voltage difference applied to the two surfaces of the upper PZT layer does not necessarily increase the buckling load. Large electric fields applied across a PZT plate can either depole it or change the direction of polarization; these effects were not accounted for in our study.

In the preceding exercise, the upper PZT was actuated irrespective of the direction of the deflection of the centroid of the plate. An improvement in the buckling load can be attained by applying a voltage difference to either the upper PZT actuator or the lower one depending upon which way the plate deflects. For positive deflection (downwards) of the centroid of the graphite-epoxy plate, an electric potential equal to $10^7|u_c|$ volts was applied to the top surface of the upper PZT, and for negative deflection of the centroid of the plate, an electric potential of $-10^7|u_c|$ volts was applied to the bottom surface of the lower PZT layer. The displacement, u_c, of the centroid of the graphite-epoxy plate is measured in meters. As should be evident from the results plotted in Fig. 2.3, the buckling load is considerably enhanced, and it equals $639.7\ \mathrm{kN/m}$ which is 58.5% larger than that when PZT layers are not activated.

The 58.5% improvement in the buckling load resulted by applying a maximum electric field of 30 kV/mm which is quite large. We subsequently limited the maximum electric field to 1 kV/mm, and experimented with applying the electric fields at the rate of $10^6,\ 10^7$ and $10^8 \times |u_c|$ volts as stated above. For these three cases, the buckling load was found to increase by 1.14, 31.11 and 18.26% respectively suggesting that for the present problem, applying electric potential equal to $10^7|u_c|$ volts is the best option out of the three considered. In each case the plate deflected in the same direction.

A close study of the time history of the evolution of the centroidal deflection of the plate given in Fig. 2.2 reveals that our definition of the dynamic buckling load differs slightly from that of Budiansky and Hutchinson [16] and Cui et al. [17]. Whereas the definition adopted herein

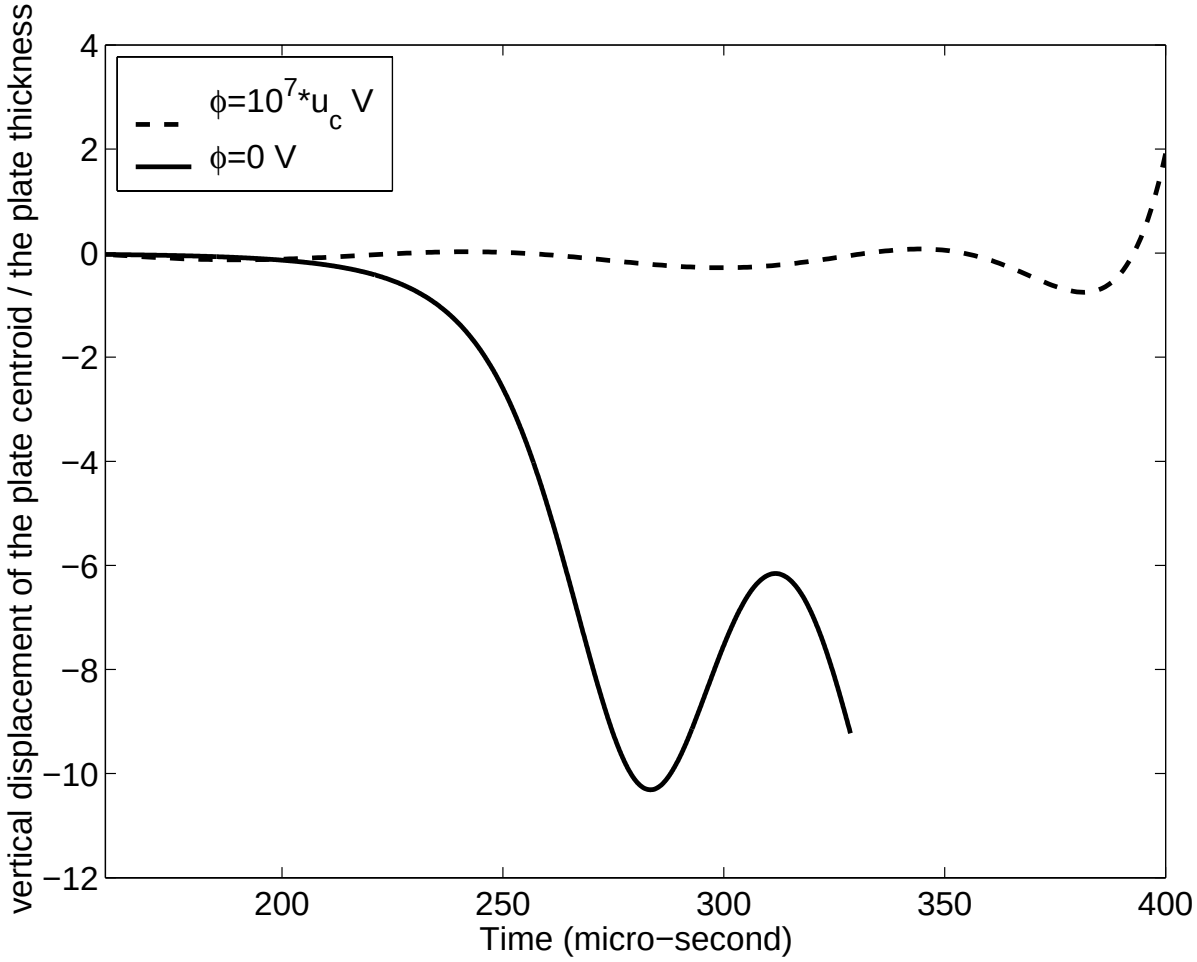

Figure 2.3: Time history of the deflection of the square graphite-epoxy plate's centroid when a voltage of $\pm 10^7 |u_c|$ is applied either to the bottom surface of the lower PZT layer or to the upper surface of the top PZT layer.

determines the buckling load uniquely, that of Budiansky and Hutchinson [16] corresponds to the load when the centroidal deflection begins to increase rapidly. The buckling load computed from the Budiansky and Hutchinson's definition will be slightly smaller than that obtained with the present definition. Cui et al. [17] equate buckling load to the point of intersection of the tangent to the rapidly rising part of the curve with the horizontal axis. This will also give a smaller buckling load than that obtained with the present definition. Irrespective of the definition of the buckling load, the activation of the PZT layers will enhance the axial load at which the plate buckles.

In the constitutive relation (2.4) for a transversely isotropic PZT, there are eight terms with coefficients $\nu_2,\ \nu_4,\ \nu_7,\ \nu_8,\ \nu_{11},\ \nu_{12},\ \mu_1$ and μ_2 that multiply quadratic terms in $\mathbf{W}$. Because of a lack of test data to determine values of these parameters we had set six of them equal to zero. In Table 3 we list the buckling loads for different values of the two nonzero parameters.

Table 3. Dependence of the buckling load on values of material parameters ν_4 and ν_{12}.

Material parameters		Buckling load
$-10^5\nu_4$	$-10^5\nu_{12}$	kN/m
9.03	0	601
	0.0305	599
	3.05	529
	305	189
0	3.05	405
0.0903		334
9.03		529
903		407

With all of the quadratic terms in $\mathbf{W}$ neglected in the constitutive relation (2.4), the buckling load equaled 322 kN/m. Thus the consideration of the two quadratic terms in the constitutive relation (2.5) generally enhances the dynamic buckling load, and the buckling load increases with

a decrease in the magnitude of ν_{12}. However, the dependence of the buckling load on the values of ν_4 is not monotonic.

Effect of the Size of the PZT Actuators

Batra and Liang [23] found through numerical experiments the optimum location of a rectangular PZT actuator to annul different modes of vibration of a simply supported rectangular plate. The difference in the electric potential across the two faces of the PZT actuator is minimum if the centroid of the actuator is located at the point where the amplitude of vibration is maximum. Even though the plate does not necessarily undergo a steady vibratory motion in the present problem, we postulate that the PZT actuator is optimally located when its centroid coincides with the centroid of the plate. This is because the initial shape of the plate is assumed to vary sinusoidally in both X_1 and X_2 directions with the maximum deflection occurring at the center of the plate surface. Its buckled shape exhibited in Fig. 2.4, closely resembles that of a plate vibrating in mode (1,1). For this deformed shape, among all the Gauss points in the PZTs, the maximum principal strain occurs at the point (0.48556 cm, 0.48556 cm, 0.03385 cm) and the value is -0.0153. Among all the Gauss points in the PZTs, the maximum principal stress occurs at the point (0.48556 cm, 0.48556 cm, 0.03385 cm) and the value is -1.8067 GPa. A comparison of the results plotted in Figs. 2.5 and 2.6 reveals that the rotations of the normals to the midsurface of the plate about the X_2-axis is more than that about the X_1-axis. It is most likely due to null tractions applied on the surfaces $X_2 = 0$ and $X_2 = 10$ mm. The four different shapes of the PZT actuators, namely, square, cross, rectangular fully extended in X_1-direction and rectangular fully extended in X_2-direction, are shown in Fig. 2.7. The buckling load of the plate with the PZT patches bonded to its upper and lower surfaces will vary with the shape and the size of the patches. When used as actuators to enhance the buckling load, a voltage difference of $\max(10^7|u_c|,\ 125)\mathrm{V}$ was applied across the two faces of the actuators. Figure 2.8 evinces the enhancement in the buckling load versus the fraction of the surface area of the plate covered by the PZT actuators for the four shapes delineated above. It is evident from these results that rectangular PZT patches fully extended in the X_2-direction are

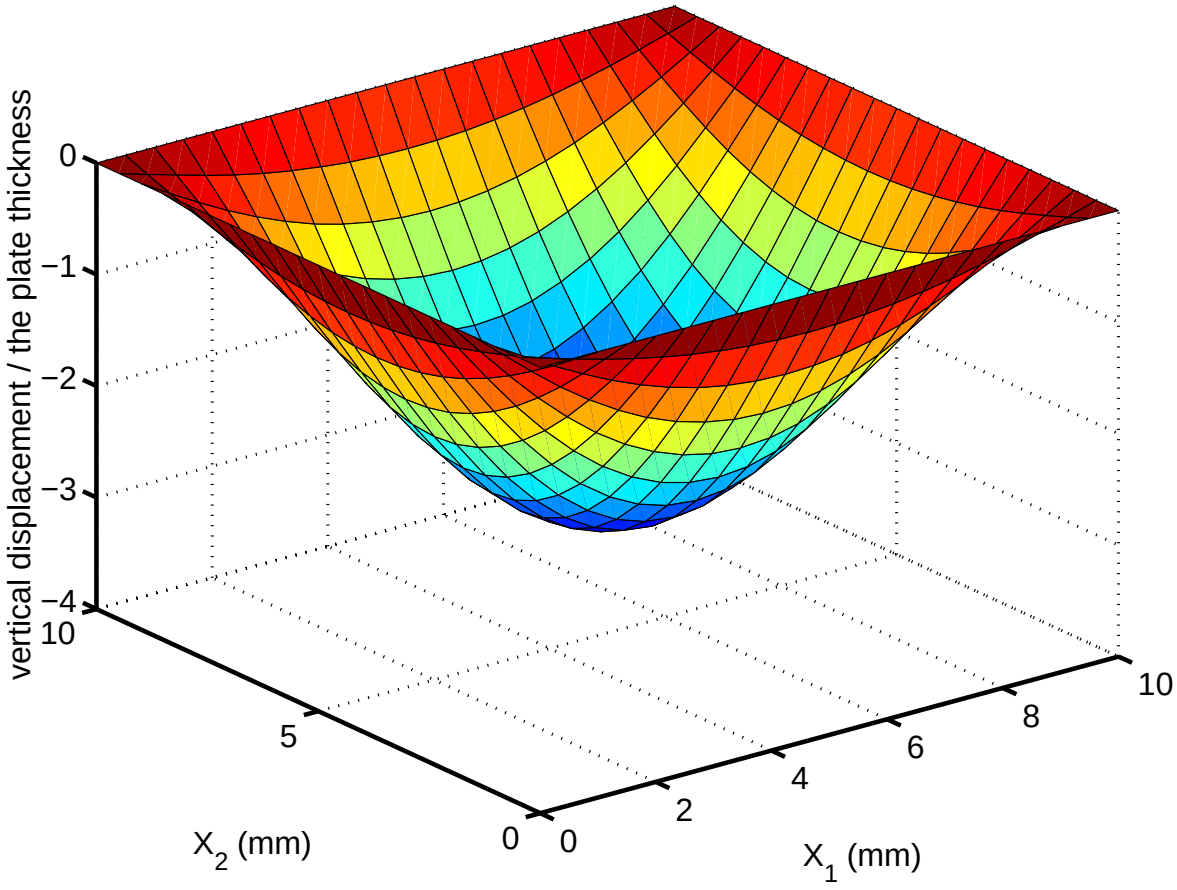

Figure 2.4: The buckled shape of a square graphite-epoxy plate loaded on two opposite edges by uniformly distributed axial tractions that increase linearly with time.

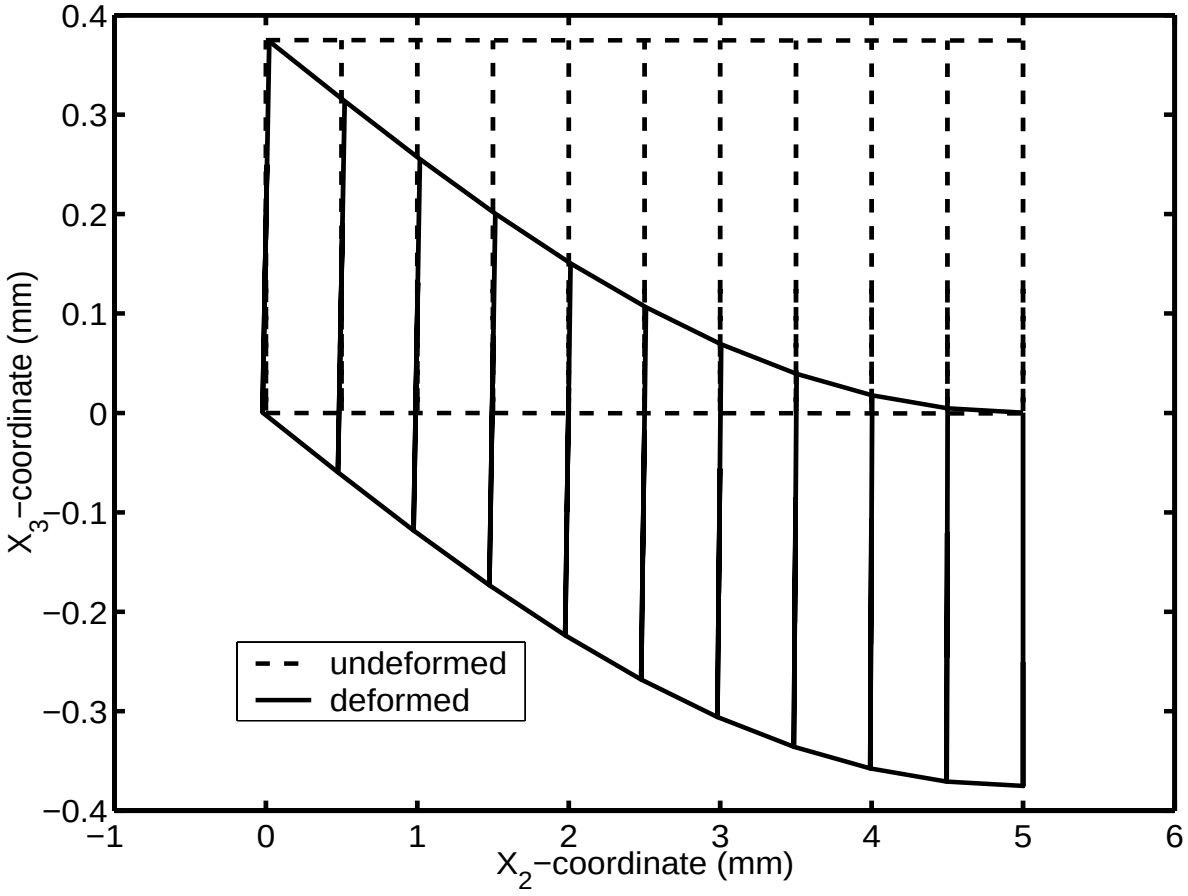

Figure 2.5: View from the X_1-axis of the square graphite-epoxy plate loaded on two opposite edges by uniformly distributed axial tractions that increase linearly with time.

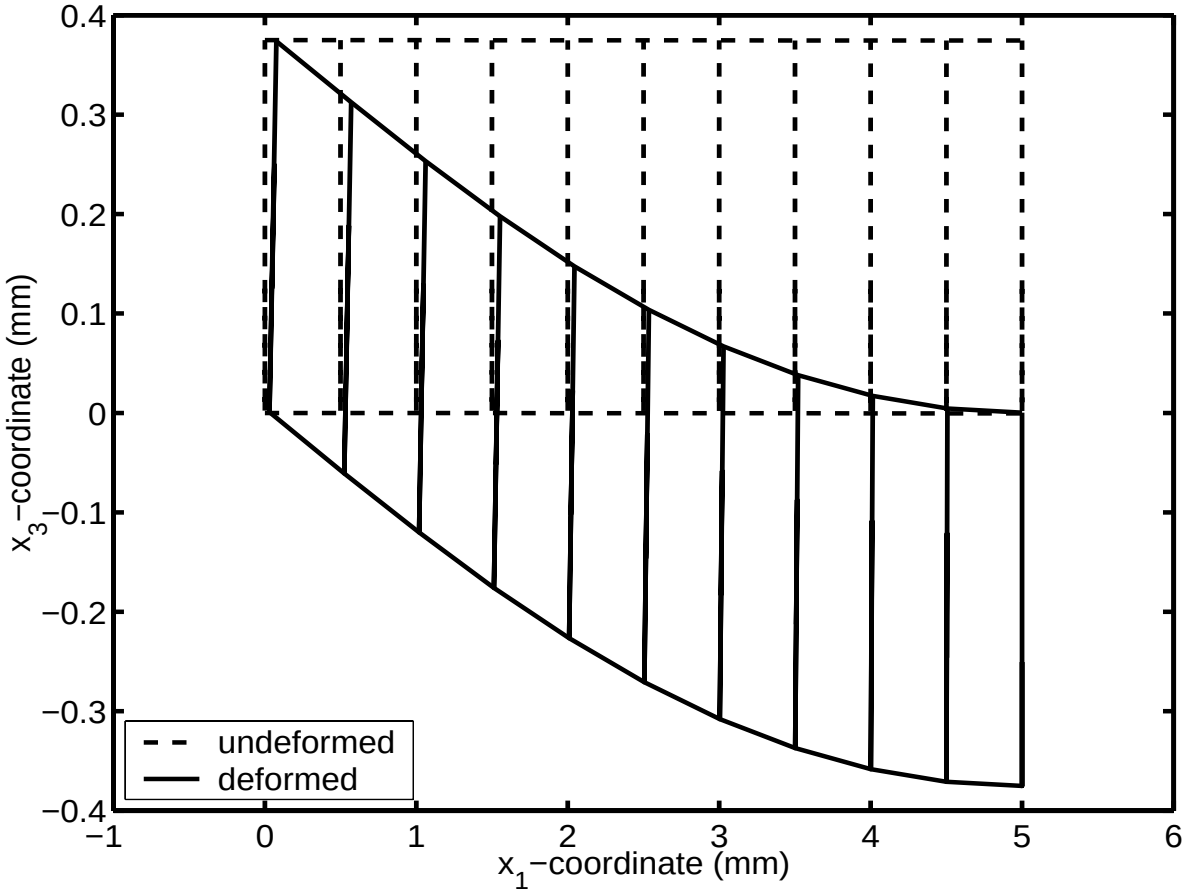

Figure 2.6: View from the X_2-axis of the square graphite-epoxy plate loaded on two opposite edges by uniformly distributed axial tractions that increase linearly with time.

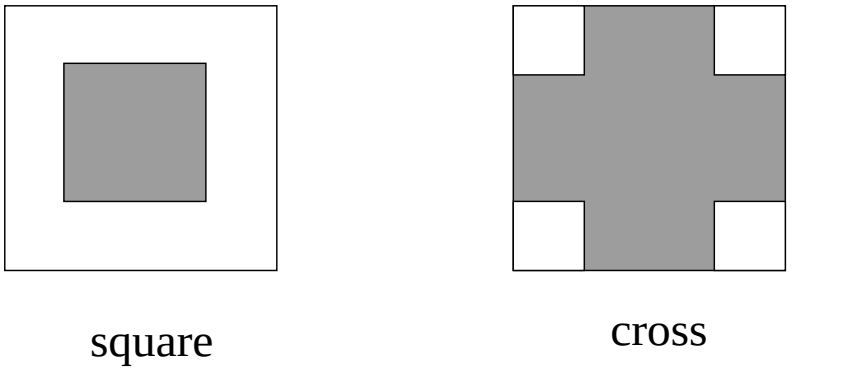

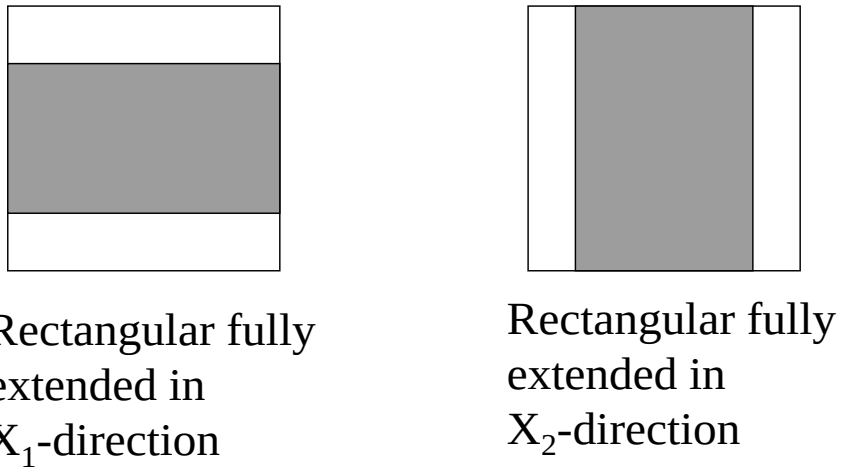

Figure 2.7: Four different shapes of PZT patches attached to the top and bottom surfaces of a square plate.

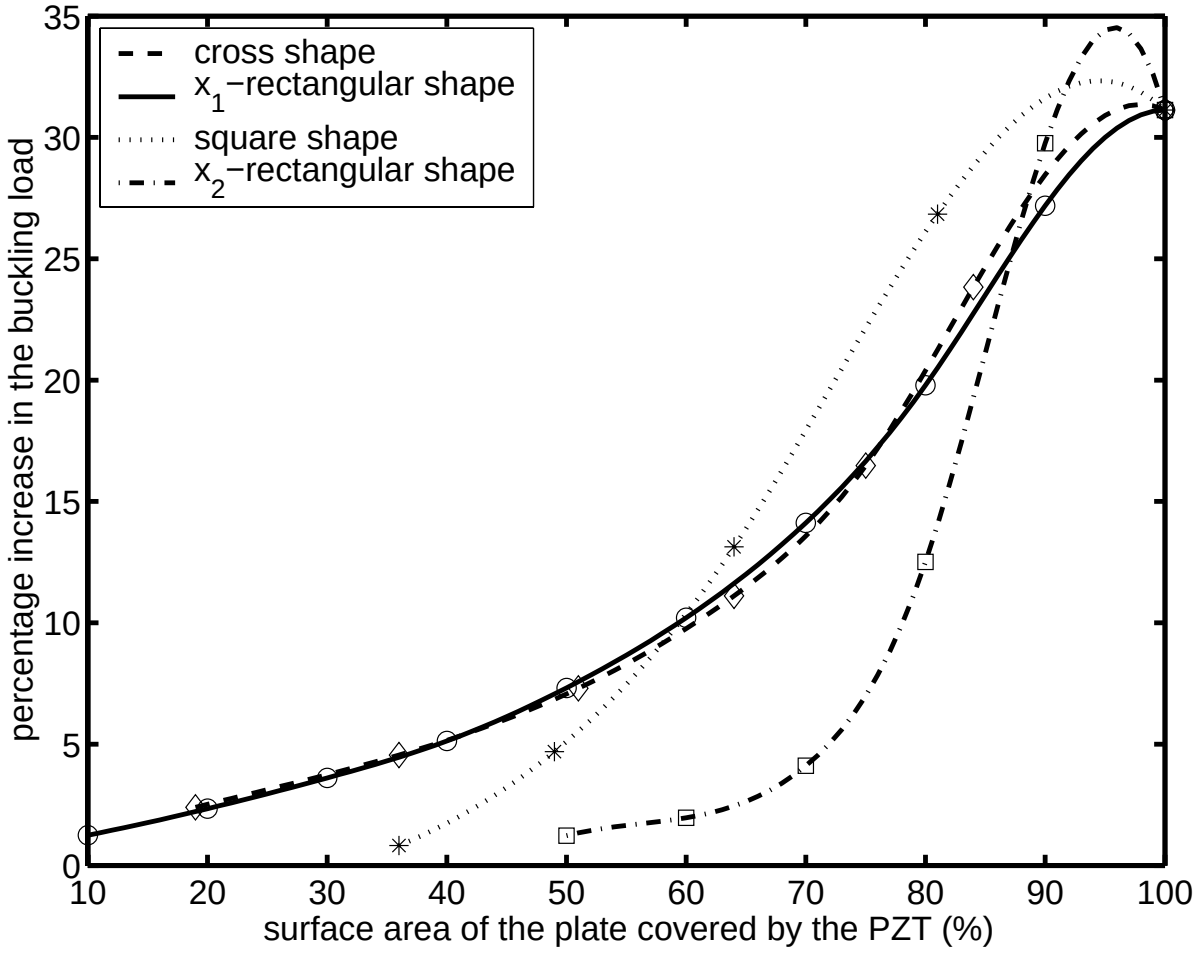

Figure 2.8: Enhancement in the buckling load of a square graphite-epoxy plate with PZT actuators bonded to its upper and lower surfaces versus fraction of the surface area covered by the PZTs.

least effective in enhancing the dynamic buckling load. Also, cross-shaped and rectangular PZT patches fully extended in the X_1-direction are equally effective in increasing the buckling load during dynamic deformations of the plate. When the surface area of the plate covered by the PZT patches is at least 60%, the square PZT patches enhance the buckling load most. Recalling that the edge loads to the plate are applied in the X_1-direction, the computed results suggest that PZT patches extending along the direction of the load are quite effective in enhancing the buckling load of the plate.

Effect of the Plate Thickness Relative to that of the PZT Layers

For this study rectangular PZT layers fully extended in the X_2-direction and covering 90% of the surface area of the plate were considered. Keeping the thickness of each PZT layer fixed at 0.125 mm, the plate thickness was assigned the values 0.25, 0.75, 1.5, 2.25 and 3 mm. In each case, the quarter of the plate was divided into uniform $10 \times 10 \times 3$ elements, and the voltage applied to the PZTs equaled $\max(10^7|u_c|,\ 125)$V. The corresponding enhancements in the buckling load were found to be 29.76, 15.21, 7.34, 0.71 and 0.31% respectively. Thus an increase in the plate thickness relative to that of the PZT layers diminishes the effect of the PZTs in enhancing the buckling load.

Effect of the Plate Dimensions and Boundary Conditions

For $10 \times 10 \times 0.125$ mm, $50 \times 50 \times 0.625$ mm, $100 \times 100 \times 1.25$ mm, and $150 \times 150 \times 1.875$ mm substrate, the dynamic buckling load per unit edge length was found to be proportional to the length of a side of the plate, and the percentage gain in the dynamic buckling load caused by the PZT actuators remained unchanged. Also, the maximum principal strain and the maximum shear strain induced in each one of the four plates were the same.

Figure 2.9 depicts the buckled shape of the plate when two opposite edges AE and BC are simply supported and the other two edges are traction free. It is clear that the deformed shape looks like a

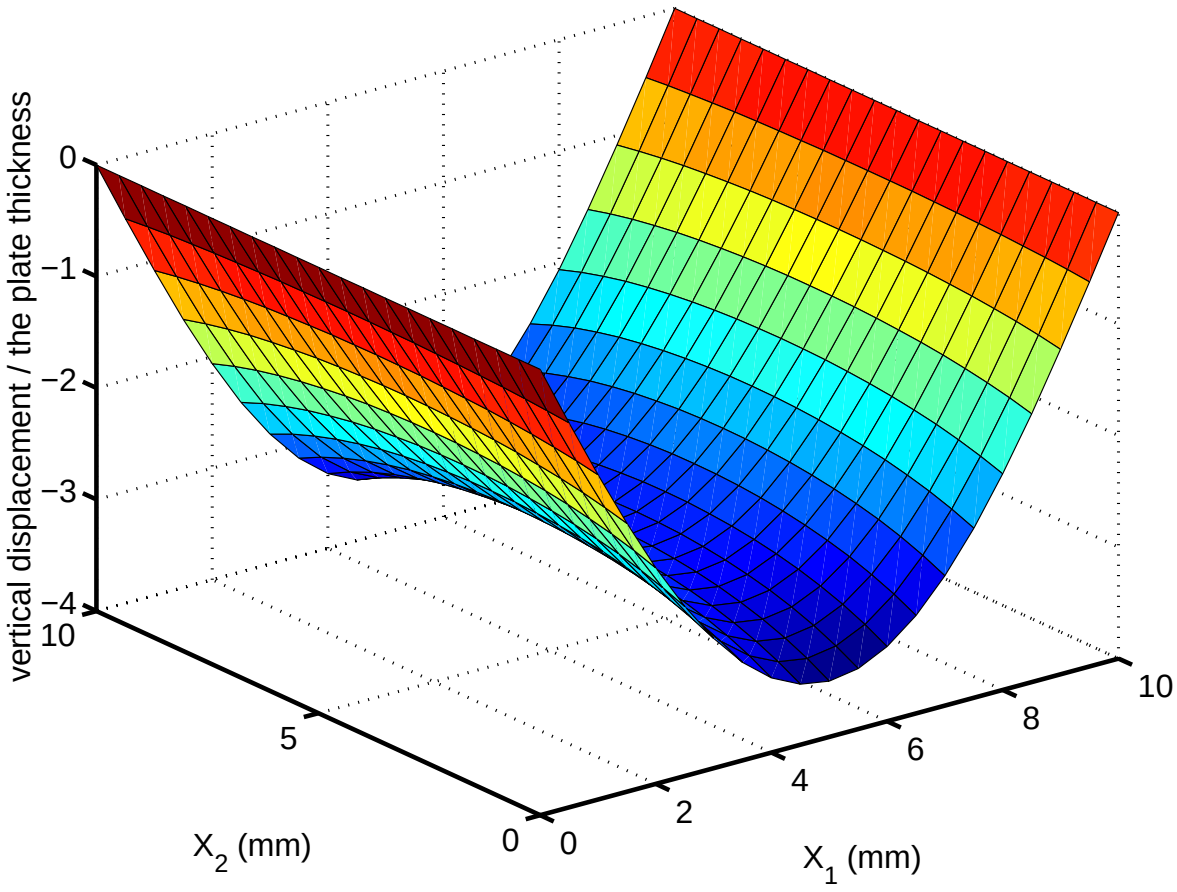

Figure 2.9: Buckled shape of the plate with two opposite edges simply supported and the other two edges traction free.

saddle rather than the double sinusoidal curve obtained when all four edges are simply supported.

2.3 Conclusions

We have used a 3-dimensional geometrically nonlinear theory to investigate the enhancement in the dynamic buckling load of a graphite-epoxy square plate sandwiched between two piezoceramic layers. The simply supported plate is loaded on two opposite edges by equal and opposite in-plane compressive time-dependent tractions with the other two edges kept traction free. The plate material is modeled as neo-Hookean and the piezoceramic by a second-order constitutive relation, i.e., the second Piola-Kirchhoff stress tensor and the electric polarization are expressed as second degree polynomials in the Green-St. Venant strain tensor and the electric field. The plate material is modeled as orthotropic and the PZT as transversely isotropic with the axis of transverse isotropy along the thickness direction. The transient problem is analyzed numerically by using the finite element code developed by Batra and Liang [3]. The plate is taken to have buckled when its centroidal deflection equaled three times the plate thickness.

The dynamic buckling load for the plate is found to strongly depend upon the rate of rise of the applied tractions and hence the inertia effects. With the maximum electric potential difference applied to the PZT layers limited to 1 kV/mm, the buckling load is enhanced by 18.3% when the PZT elements are activated. For a maximum electric field of 30 kV/mm, the buckling load increased by 58.5%. When only a part of the top and bottom surfaces of the plate can be covered by PZT layers, then square PZT elements give a larger enhancement in the buckling load than rectangular shaped or cross-shaped PZT elements provided that the covered surface area exceeds 60%. Otherwise the cross-shaped and rectangular PZT elements fully covering the square plate in the loading direction result in higher buckling loads than the square shaped PZT actuators.

An increase in the plate thickness relative to that of the PZT layers decreases the effectiveness of the PZTs in enhancing the buckling load for the plate. Of course, design considerations may limit the thickness of the PZT layers that can be used.

Even though we have not verified it, we believe that other definitions of the dynamic buckling load will not alter the qualitative nature of results but may change the magnitude of the gain in the buckling load achieved by activating the PZTs.

Chapter 3

Comparison of Active Constrained Layer Damping by using Extension and Shear Mode Piezoceramic Actuators *

3.1 Formulation of the Problem

Schematic sketches of the problem studied are shown in Figs. 3.1 and 3.2. Fig. 3.1 depicts an ACLD (Active Constrained Layer Damping) treatment with a shear mode PZT actuator and Fig. 3.2 with two extension mode PZT actuators. The total thicknesses of the PZT and the aluminum layers in the two cases are the same. However, because of the differences in the vertical positions of the two layers and in their material properties, their structural stiffnesses will be different. Thus the same load applied at geometrically similar points will result in different deformations of points in the aluminum layers. Whereas the electric field is applied in the x_3-direction for both the shear mode and the extension mode PZT actuators, they are poled in the x_1-direction in the former case and the x_3-direction in the latter case.

*A slightly modified version of this chapter has been submitted, for possible publication, to **Journal of Intelligent Material System and Structures**.

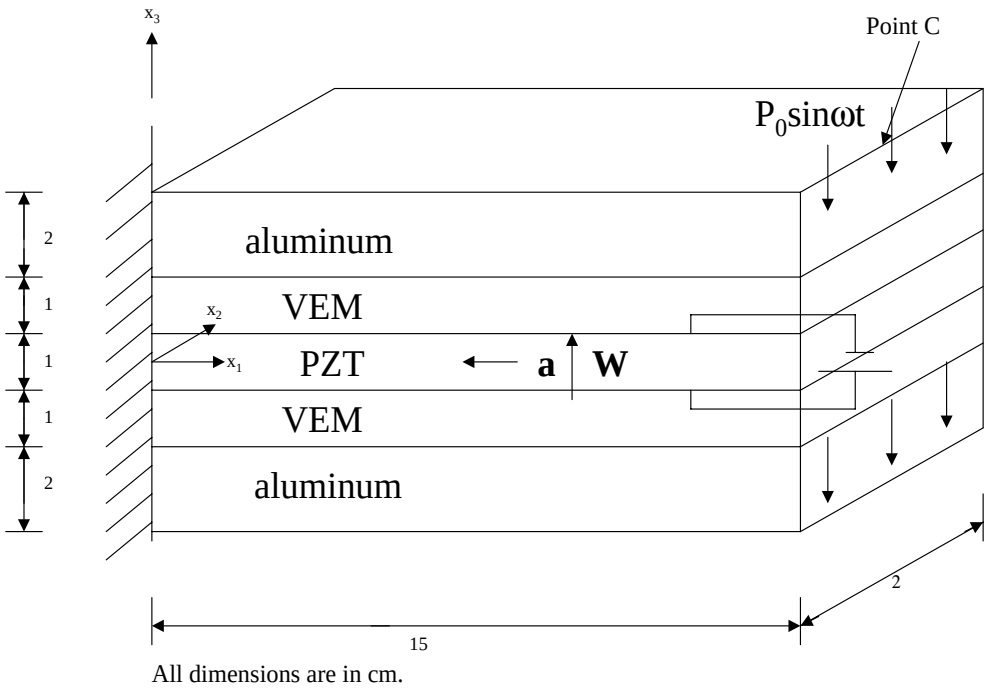

Figure 3.1: Schematic sketch of the problem studied; (a) ACLD treatment with a shear mode actuator. Unit vectors $\mathbf{a}$ and $\mathbf{W}$ point in the directions of polarization and the electric field respectively.

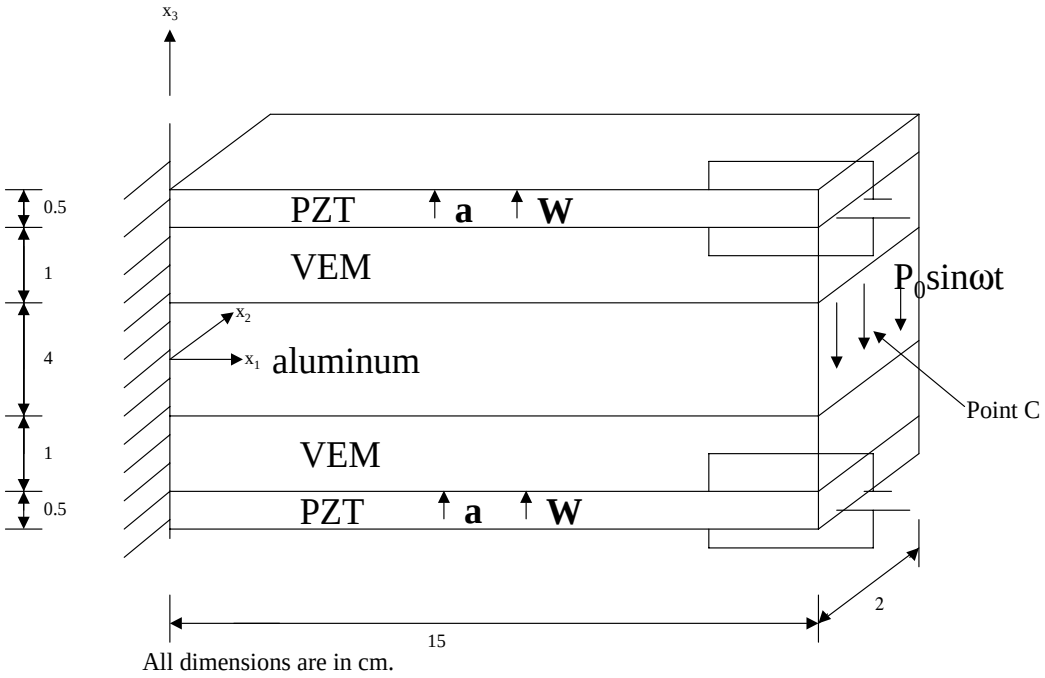

Figure 3.2: Schematic sketch of the problem studied; (b) ACLD treatment with extension mode actuators. Unit vectors $\mathbf{a}$ and $\mathbf{W}$ point in the directions of polarization and the electric field respectively.

In the Lagrangean description of motion and in the absence of body forces and distributed charges, equations governing dynamic deformations of a structure are

$$\rho J = \rho_0, \tag{3.1}$$

$$\rho_0 \ddot{x}_i = T_{i\alpha,\alpha},\ i = 1,2,3,\ \alpha = 1,2,3, \tag{3.2}$$

$$T_{i\alpha} x_{j,\alpha} = T_{j\alpha} x_{i,\alpha}, \tag{3.3}$$

$$D_{\alpha,\alpha} = 0, \tag{3.4}$$

where we have used rectangular Cartesian coordinates x_i and X_α to describe the position of the same material particle in the present and the reference configurations respectively. A superimposed dot indicates the material time derivative, $J = \det[x_{i,\alpha}]$, $x_{i,\alpha} \equiv \partial x_i / \partial X_\alpha$, $\mathbf{T}$ is the first Piola-Kirchhoff (or the nominal or the engineering) stress tensor, a repeated index implies summation over the range of the index, ρ and ρ_0 equal mass densities in the present and the reference configurations respectively, and $\mathbf{D}$ is the electric displacement. Latin and Greek indices signify components of a tensor with respect to coordinates in the present and the reference configurations respectively. Equations (3.1), (3.2), (3.3) and (3.4) express, respectively, the balance of mass, the balance of linear momentum, the balance of moment of momentum, and the Maxwell equation with inertia effects associated with the electric field neglected. Note that the balance of moment of momentum is identically satisfied by requiring that the Cauchy stress tensor, $\boldsymbol{\sigma}$, related to $\mathbf{T}$ by

$$\sigma_{ij} = J^{-1} T_{i\alpha} x_{j,\alpha}, \tag{3.5}$$

be symmetric. Furthermore, once the present positions x_i of material particles are known, the present mass density can be computed from eqn. (3.1). Thus we need to solve equations (3.2) and (3.4) for x_i and the electric potential. Equations (3.2) and (3.4) are to be supplemented by initial and boundary conditions and constitutive relations.

We assume that the host structure and the viscoelastic layer are made of homogeneous and isotropic materials and the PZT of a homogeneous and transversely isotropic material with the axis of

transverse isotropy coincident with the poling direction. In terms of the symmetric second Piola-Kirchhoff stress tensor, $S_{\alpha\beta}$, related to the first Piola-Kirchhoff stress tensor $\mathbf{T}$ by

$$T_{i\alpha} = x_{i,\beta} S_{\alpha\beta}, \tag{3.6}$$

constitutive relations for materials of the three layers are given below.

Host layer:

$$S_{\alpha\beta} = \frac{\nu Y}{(1+\nu)(1-2\nu)} E_{\gamma\gamma}\delta_{\alpha\beta} + \frac{Y}{(1+\nu)} E_{\alpha\beta}; \tag{3.7}$$

Viscoelastic material:

$$\begin{aligned} S_{\alpha\beta} = {} & \frac{\nu Y \delta_{\alpha\beta}}{(1+\nu)(1-2\nu)} \left[E_{\gamma\gamma}(t) - \frac{\chi}{\tau} \int_{-\infty}^{t} e^{-\frac{t-s}{\tau}} E_{\gamma\gamma}(s) ds \right] \\ & + \frac{Y}{(1+\nu)} \left[E_{\alpha\beta}(t) - \frac{\chi}{\tau} \int_{-\infty}^{t} e^{-\frac{t-s}{\tau}} E_{\alpha\beta}(s) ds \right]; \end{aligned} \tag{3.8}$$

PZT:

$$\begin{aligned} \mathbf{S} = {} & (2c_1 I_1 + c_3 I_2 + e_1 I_3 + 3\lambda_1 I_1^2 + 2\lambda_3 I_1 I_2 + \lambda_4 I_2^2 + \lambda_5 II_1 + \lambda_7 II_2 + 2\nu_1 I_1 I_3 \\ & + \nu_2 I_3^2 + \nu_7 II_3 + \nu_9 II_4 + \nu_{14} I_2 I_3)\mathbf{a} \otimes \mathbf{a} + (2c_2 I_2 + c_3 I_1 + e_2 I_3 + 3\lambda_2 I_2^2 + \lambda_3 I_1^2 \\ & + 2\lambda_4 I_1 I_2 + \lambda_6 II_1 + \lambda_8 II_2 + 2\nu_3 I_2 I_3 + \nu_4 I_3^2 + \nu_8 II_3 + \nu_{10} II_4 + \nu_{14} I_1 I_3)\mathbf{1} \\ & + (c_4 + \lambda_5 I_1 + \lambda_6 I_2 + \nu_5 I_3)(\mathbf{a} \otimes \mathbf{E} \cdot \mathbf{a} + \mathbf{a} \cdot \mathbf{E} \otimes \mathbf{a}) + 2(c_5 + \lambda_7 I_1 + \lambda_8 I_2 + \nu_6 I_3)\mathbf{E} \\ & + (e_3 + \nu_9 I_1 + \nu_{10} I_2 + \nu_{11} I_3)(\mathbf{a} \otimes \mathbf{W} + \mathbf{W} \otimes \mathbf{a}) + 3\lambda_9 \mathbf{E}^2 + \nu_{12} \mathbf{W} \otimes \mathbf{W} \\ & + \nu_{13}(\mathbf{a} \otimes \mathbf{E} \cdot \mathbf{W} + \mathbf{W} \cdot \mathbf{E} \otimes \mathbf{a} + \mathbf{W} \otimes \mathbf{E} \cdot \mathbf{a} + \mathbf{a} \cdot \mathbf{E} \otimes \mathbf{W}), \\ -\boldsymbol{\pi} = {} & (2\epsilon_1 I_3 + e_1 I_1 + e_2 I_2 + 3\mu_1 I_3^2 + \mu_2 II_3 + \nu_1 I_1^2 + 2\nu_2 I_3 I_1 + \nu_3 I_2^2 + 2\nu_4 I_3 I_2 \\ & + \nu_5 II_1 + \nu_6 II_2 + \nu_{11} II_4 + \nu_{14} I_1 I_2)\mathbf{a} + 2(\epsilon_2 + \mu_2 I_3 + \nu_7 I_1 + \nu_8 I_2)\mathbf{W} \\ & + 2(e_3 + \nu_9 I_1 + \nu_{10} I_2 + \nu_{11} I_3)\mathbf{E} \cdot \mathbf{a} + 2\nu_{12} \mathbf{E} \cdot \mathbf{W} + 2\nu_{13} \mathbf{E}^2 \cdot \mathbf{a}; \end{aligned} \tag{3.9}$$

where

$$E_{\alpha\beta} = (u_{\alpha,\beta} + u_{\beta,\alpha} + u_{\gamma,\alpha}u_{\gamma,\beta})/2,$$
$$u_\alpha = x_i\delta_{i\alpha} - X_\alpha, \tag{3.10}$$

$$I_1 = \mathbf{a}\cdot\mathbf{E}\mathbf{a}, \qquad I_2 = \operatorname{tr}\mathbf{E}, \qquad I_3 = \mathbf{a}\cdot\mathbf{W},$$
$$II_1 = \mathbf{a}\cdot\mathbf{E}^2\mathbf{a}, \quad II_2 = \operatorname{tr}\mathbf{E}^2, \quad II_3 = \mathbf{W}\cdot\mathbf{W}, \tag{3.11}$$
$$II_4 = \mathbf{a}\cdot\mathbf{E}\mathbf{W} + \mathbf{W}\cdot\mathbf{E}\mathbf{a}.$$

Here $\mathbf{u}$ equals the mechanical displacement of a material point, $\mathbf{E}$ is the strain tensor appropriate for finite deformations of a body, $\delta_{\alpha\beta}$ is the Kronecker delta, $\mathbf{a}$ is a unit vector along the poling direction of the PZT, $\boldsymbol{b}\otimes\boldsymbol{c}$ denotes the tensor product between vectors $\boldsymbol{b}$ and $\boldsymbol{c}$ defined as $(\boldsymbol{b}\otimes\boldsymbol{c})\boldsymbol{d} = (\boldsymbol{c}\cdot\boldsymbol{d})\boldsymbol{b}$ for every vector $\boldsymbol{d}$, $\boldsymbol{b}\cdot\boldsymbol{c}$ denotes the inner product between vectors $\boldsymbol{b}$ and $\boldsymbol{c}$, $\boldsymbol{\pi}$ is the polarization vector that is related to the electric displacement $\mathbf{D}$, the electric field $\mathbf{W}$ and the electric potential ϕ through

$$\pi_\alpha = D_\alpha - \varepsilon_0 J X_{\alpha,i}X_{\beta,i}W_\beta,\ W_\beta = -\phi_{,\beta}, \tag{3.12}$$

where ε_0 is the dielectric permittivity of the free space.

In eqn. (3.7) Y is Young's modulus and ν Poisson's ratio. Equation (3.7) implies that the material of the host layer is being modeled as neo-Hookean. Equation (3.8) signifies that both the shear and the bulk response of the viscoelastic material have the same relaxation time τ and the Poisson ratio is independent of time. If relaxation times and/or values of χ for the bulk and the shear moduli are different, then Poisson's ratio of the viscoelastic material will depend upon time t. Also, generalization to the case of more than one relaxation time for the shear and the bulk moduli is fairly straightforward to implement in the analysis of the problem. Christensen [35] has discussed how equation (3.8) relates to nonlinear viscoelastic materials; here we note that it is analogous to

equation (3.7). Yu and Batra [56] used the analogue of equation (3.8) for incompressible materials to analyze damping induced by a viscoelastic layer enclosed between two cylinders and undergoing finite torsional deformations. For the strain history

$$\mathbf{E}(t) = \mathbf{E}^0, \tag{3.13}$$

equation (3.8) yields

$$S_{\alpha\beta} = \left(\frac{\nu Y}{(1+\nu)(1-2\nu)} E^0_{\gamma\gamma}\delta_{\alpha\beta} + \frac{Y}{(1+\nu)} E^0_{\alpha\beta} \right) (1 - \chi + \chi e^{-t/\tau}). \tag{3.14}$$

Thus the stress eventually relaxes to $(1-\chi)$ times that in a neo-Hookean material with Young's modulus Y and Poisson's ratio ν.

For infinitesimal sinusoidal deformations with the strain history

$$E_{\alpha\beta}(t) = \varepsilon^0_{\alpha\beta} \sin \omega t, \ |\varepsilon^0_{\alpha\beta}| \ll 1, \tag{3.15}$$

equation (3.8) gives

$$S_{\alpha\beta}(t) = \frac{\left((1+\tau^2\omega^2-\chi)^2 + \chi^2\tau^2\omega^2\right)^{1/2}}{1+\omega^2\tau^2} \left[\frac{\nu Y \varepsilon^0_{\gamma\gamma}}{(1+\nu)(1-2\nu)}\delta_{\alpha\beta} + \frac{Y}{1+\nu}\varepsilon^0_{\alpha\beta} \right] \sin(\omega t + \delta), \tag{3.16}$$

where

$$\tan\delta = (\chi\omega\tau)/(1+\tau^2\omega^2-\chi). \tag{3.17}$$

Thus the phase shift, δ, between the applied infinitesimal sinusoidal strain history and the induced stress history depends upon the frequency ω, the relaxation time τ and the factor χ. Also, the amplitude of each component of stress is smaller than $(1+\chi^2)^{1/2}$ times that in a Hookean material of Young's modulus Y and Poisson's ratio ν. Each component of stress exhibits the same phase

shift with respect to its value in the corresponding Hookean material for which $\chi = 0$. The storage bulk and shear moduli of the viscoelastic material equal $(1 - \chi/(1 + \tau^2\omega^2))$ times those for the corresponding elastic material, and the multiplying factor for the loss moduli is $\chi\omega\tau/(1 + \omega^2\tau^2)$. Thus the maximum value of the loss moduli and hence of energy dissipated per unit volume of the viscoelastic material occurs for $\tau = 1/\omega$. It is not easy to identify the storage and the loss moduli in the presence of geometric nonlinearities.

With the definition

$$\eta_{\alpha\beta}(t) = \frac{1}{\tau}\int_{-\infty}^{t} e^{-\frac{t-s}{\tau}} E_{\alpha\beta}(s)ds, \tag{3.18}$$

equation (3.8) becomes

$$\begin{aligned} S_{\alpha\beta} = & \left(\frac{\nu Y(1-\chi)}{(1+\nu)(1-2\nu)}\eta_{\gamma\gamma}\delta_{\alpha\beta} + \frac{Y(1-\chi)}{(1+\nu)}\eta_{\alpha\beta}\right) \\ & + \frac{\nu Y\tau}{(1+\nu)(1-2\nu)}\dot{\eta}_{\gamma\gamma}\delta_{\alpha\beta} + \frac{Y\tau}{(1+\nu)}\dot{\eta}_{\alpha\beta}. \end{aligned} \tag{3.19}$$

With $\eta_{\alpha\beta}$ interpreted as a pseudo strain and $\dot{\eta}_{\alpha\beta}$ as a pseudo strain-rate, constitutive relation (3.8) represents a Kelvin material with an isotropic neo-Hookean material of Young's modulus $Y(1-\chi)$ and Poisson's ratio ν connected in parallel with a purely viscous isotropic material of bulk viscosity $\nu Y\tau/(1+\nu)(1-2\nu)$ and shear viscosity $Y\tau/(1+\nu)$. We note that for finite deformations, $\dot{E}_{\alpha\beta}$ does not equal the strain rate.

Equation (3.18) implies that $\eta_{\alpha\beta}$ satisfies the ordinary differential equation

$$\tau\dot{\eta}_{\alpha\beta} + \eta_{\alpha\beta} = E_{\alpha\beta}. \tag{3.20}$$

Second-order constitutive relations (3.9) for the piezoelectric material were derived by Yang and Batra [55] and contain terms quadratic in the electric field $\mathbf{W}$ and the strain tensor $\mathbf{E}$. In these equations $c_1, c_2, \ldots, e_1, e_2, \ldots, \lambda_1, \lambda_2 \ldots$ and $\nu_1, \nu_2 \ldots$ are material parameters. There is not sufficient test data available to evaluate all of these material parameters. Batra and Liang [27] have

shown that for an unconstrained PZT nonzero values of $c_1, c_2, c_3, c_4, c_5, e_1, e_2, e_3, \varepsilon_1, \varepsilon_2, \nu_4$ and ν_{12} yield a material response that is close to the one observed experimentally by Crawley and Anderson [36]. Tiersten [47] has considered third order terms in $\mathbf{W}$ and obtained a better agreement between the computed and the observed axial strain vs. the applied electric field. Furthermore, the permittivity ε_0 of the free space is usually quite small so that equation $(3.12)_1$ is simplified to $\boldsymbol{\pi} = \mathbf{D}$. Accordingly, equations (3.9) simplify to

$$\begin{aligned} S_{\alpha\beta} &= (2c_1 I_1 + c_3 I_2 + e_1 I_3) a_\alpha a_\beta + (2c_2 I_2 + c_3 I_1 + e_2 I_3 + \nu_4 I_3^2)\delta_{\alpha\beta} \\ &\quad + c_4(a_\alpha E_{\beta\gamma} a_\gamma + a_\beta E_{\alpha\gamma} a_\gamma) + 2c_5 E_{\alpha\beta} + e_3(a_\alpha W_\beta + a_\beta W_\alpha) + \nu_{12} W_\alpha W_\beta, \\ -D_\alpha &= (2\varepsilon_1 I_3 + e_1 I_1 + e_2 I_2 + 2\nu_4 I_2 I_3) a_\alpha + 2\varepsilon_2 W_\alpha + 2e_3 E_{\alpha\beta} a_\beta + 2\nu_{12} E_{\alpha\beta} W_\beta. \end{aligned} \tag{3.21}$$

For an extension mode actuator poled in the x_3-direction and the electric field also applied in the x_3-direction,

$$a_\alpha = \delta_{3\alpha},\ W_\alpha = W\delta_{3\alpha}, \tag{3.22}$$

and equations (3.21) reduce to

$$\left\{\begin{array}{c} S_{11} \\ S_{22} \\ S_{33} \\ S_{23} \\ S_{31} \\ S_{12} \\ -- \\ D_1 \\ D_2 \\ D_3 \end{array}\right\} = \left[\begin{array}{cccccc|c} 2(c_2+c_5) & 2c_2 & 2c_2+c_3 & 0 & 0 & 0 & e_2 \\ 2c_2 & 2(c_2+c_5) & 2c_2+c_3 & 0 & 0 & 0 & e_2 \\ c_3+2c_2 & c_3+2c_2 & A_e & 0 & 0 & 0 & B_e \\ 0 & 0 & 0 & c_{4/2}+c_5 & 0 & 0 & 0 \\ 0 & 0 & 0 & 0 & c_{4/2}+c_5 & 0 & 0 \\ 0 & 0 & 0 & 0 & 0 & c_5 & 0 \\ \hline 0 & 0 & 0 & 0 & -e_3 & 0 & -2\nu_{12}E_{13} \\ 0 & 0 & 0 & -e_3 & 0 & 0 & -2\nu_{12}E_{23} \\ -e_2 & -e_2 & -B_e & 0 & 0 & 0 & -C_e \end{array}\right]$$

$$\times \left\{\begin{array}{c} E_{11} \\ E_{22} \\ E_{33} \\ 2E_{23} \\ 2E_{31} \\ 2E_{12} \\ - - - \\ W \end{array}\right\} + W^2 \left\{\begin{array}{c} \nu_4 \\ \nu_4 \\ \nu_4+\nu_{12} \\ 0 \\ 0 \\ 0 \\ - - - \\ 0 \end{array}\right\} \tag{3.23}$$

where

$$A_e = 2(c_1+c_2+c_3+c_4+c_5),\ B_e = e_1+e_2+2e_3,\ C_e = 2(\nu_4 E_{\gamma\gamma}+\nu_{12}E_{33})+2(\varepsilon_1+\varepsilon_2).$$

When the PZT actuator acts in shear mode with

$$a_\alpha = \delta_{1\alpha},\ W_\alpha = W\delta_{3\alpha}, \tag{3.24}$$

equations (3.21) become

$$\left\{\begin{array}{c} S_{11} \\ S_{22} \\ S_{33} \\ S_{23} \\ S_{31} \\ S_{12} \\ \hline -D_1 \\ -D_2 \\ -D_3 \end{array}\right\} = \left[\begin{array}{cccccc|c} A_s & 2c_2+c_3 & 2c_2+c_3 & 0 & 0 & 0 & 0 \\ 2c_2+c_3 & 2(c_2+c_5) & 2c_2 & 0 & 0 & 0 & 0 \\ 2c_2+c_3 & 2c_2 & 2(c_2+c_5) & 0 & 0 & 0 & 0 \\ 0 & 0 & 0 & c_5 & 0 & 0 & 0 \\ 0 & 0 & 0 & 0 & c_{4/2}+c_5 & 0 & e_3 \\ 0 & 0 & 0 & 0 & 0 & c_{4/2}+c_5 & 0 \\ \hline (e_1+e_2+2e_3) & e_2 & e_2 & 0 & 0 & 0 & B_s \\ 0 & 0 & 0 & 0 & 0 & e_3 & C_s \\ 0 & 0 & 0 & 0 & e_3 & 0 & D_s \end{array}\right]$$

$$\times \left\{\begin{array}{c} E_{11} \\ E_{22} \\ E_{33} \\ 2E_{23} \\ 2E_{31} \\ 2E_{12} \\ \hline W \end{array}\right\} + W^2 \left\{\begin{array}{c} 0 \\ 0 \\ \nu_{12} \\ 0 \\ 0 \\ 0 \\ \hline 0 \end{array}\right\} \tag{3.25}$$

where $A_s = 2(c_1+c_2+c_3+c_4+c_5)$, $B_s = 2\nu_{12}E_{13}$, $C_s = 2\nu_{12}E_{23}$, $D_s = 2(\varepsilon_2 + \nu_{12}E_{33})$.

Equations (3.23) and (3.25), written for specific choices of the electric field and the polarization directions, reveal that piezoelectric moduli $e_1,\ e_2,\ e_3,\ \nu_4$ and ν_{12} affect stresses induced in the extension mode actuator by the electric field $\mathbf{W}$ but only e_3 and ν_{12} cause stresses in the shear mode actuator. Also for our choice of directions of the polarization vector $\mathbf{a}$ and the electric field $\mathbf{W}$, terms quadratic in the electric field do not appear in expressions for shear stresses. If the polarization vector $\mathbf{a}$ were not aligned along one of the coordinate axes, then an electric field in the

thickness direction will induce both normal and shear stresses in the PZT and the actuation effect for the same electric field may be enhanced. Vidoli and Batra ([53], [54]) have explored such possibilities and found optimum orientations of the direction of the polarization vector of a PZT beam and a rod. Vel and Batra [52] studied cylindrical bending deformations of an extension-shear bimorph with the axis of polarization inclined at an angle α with the vertical axis. For PZT-5A, they found that the maximum tip deflection is realized in a combined extension-shear bimorph at $\alpha \approx 20^\circ$ for span-to-thickness ratio of 10 and at $\alpha \approx 28^\circ$ when the ratio is 5. We note that even when electric potential difference is applied uniformly to the top and the bottom surfaces of the PZT layer, an electric field may also be induced in x_1 and x_2 directions by the direct piezoelectric effect. Such possibilities are incorporated in the 3-dimensional analysis of the problem presented herein.

Batra [18] has modeled finite deformations of isotropic elastic materials by four frame-indifferent constitutive relations that express a stress tensor as a linear function of an appropriate strain tensor. He found that for large simple shearing or simple extensional deformations, equation (3.7) predicts a stiffening behavior in the sense that the nominal stress required to deform the body increases with an increase in the magnitude of the corresponding strain. A similar result was proved by Batra and Yu [26] for incompressible viscoelastic materials modeled by equation (3.8) with the term multiplying $E_{\gamma\gamma}(t)$ replaced by a hydrostatic pressure that can not be determined from the history of the deformation. For the present problem, strains induced in structural elements are not large enough for the stiffening effects to play a noticeable role.

In the analysis of the problem we assume that the upper and the lower surfaces of PZT layers are electroded with electrodes of negligible thickness, and all bounding surfaces of the viscoelastic layer and the host structure are electrically insulated. Even though the viscoelastic layer and the host structure may conduct electricity, such effects are not considered herein. We note that Cheng and Batra [34] have delineated effects of electrodes on static deformations of a hybrid laminated composite. The electric potential is prescribed on the upper and the lower surfaces of the PZT layers, and surfaces $x_1 = 0, L$ are electrically insulated. Continuity conditions at the interfaces

between two dissimilar materials are

$$[\![T_{i\alpha}N_\alpha]\!] = 0,\ [\![u_i]\!] = 0, \tag{3.26}$$

where $\mathbf{N}$ is an outward unit normal to the surface in the reference configuration, and $[\![f]\!]$ equals the difference in the values of f on the two sides of an interface. Thus the two adjoining layers are presumed to be perfectly bonded to each other with surface tractions and displacements continuous across their common interfaces. The edge $x_1 = X_1 = 0$ of the hybrid laminated plate is rigidly clamped, and a time harmonic tangential traction is applied only to the host structure at the edge $X_1 = L$. That is

$$\begin{aligned} &u_i = 0 \text{ on the surface } x_1 = X_1 = 0, \\ &T_{i1} = 0 \text{ on the surface } X_1 = L \text{ of the PZT and the viscoelastic layer}, \\ &T_{i1} = -(p_0 \sin\omega t)\delta_{i3} \text{ on the surface } X_1 = L \text{ of the host structure}. \end{aligned} \tag{3.27}$$

For times $t \leq 0$, we assume that all material points of the structure are at rest and have null displacements. Thus the lower limit of integration in equation (3.8) is zero.

Because of the time harmonic load applied, the response of the structure will be periodic after initial transients have died out. We note that no such assumption is made in the analysis of the problem and deformation fields as a function of time are computed numerically by the finite element method. During one cycle of deformation, energy input into the structure is given by

$$E^{\text{in}} = \int_0^{2\pi/\omega} dt \left[\int_{A_h} (-p_0 \sin\omega t)\dot{u}_3 dA - \int_{A_p} \phi \dot{D}_3 dA \right]. \tag{3.28}$$

Here A_h is the surface of the host structure where tangential tractions $(3.27)_3$ are prescribed, and A_p surfaces $X_3 = \text{const.}$ of the PZT layers where the electric potential is applied. Work done by

internal stresses in the viscoelastic layer during a cycle of deformation can be computed from

$$W = \int_0^{2\pi/\omega} dt \int_{V_{ve}} T_{i\alpha}\dot{x}_{i,\alpha} dV = \int_0^{2\pi/\omega} dt \int_{V_{ve}} S_{\alpha\beta}\dot{E}_{\alpha\beta} dV, \tag{3.29}$$

where V_{ve} is the region occupied by the viscoelastic layer in the reference configuration. Since stresses in the viscoelastic layer have two parts - one in phase and the other out of phase with the velocity gradients - a part of the work done W is stored in the body and the rest is dissipated. For a linear problem involving infinitesimal deformations, these two parts of stresses can be identified, e.g. see eqn. (3.16), and the energy dissipated per cycle per unit volume of the viscoelastic material is given by

$$W^{\text{dis}} = \frac{\pi\chi\tau}{(1+\tau^2\omega^2)} \frac{Y}{1+\nu} \left[\frac{\nu}{1-2\nu} \varepsilon^{\circ}_{\gamma\gamma}\varepsilon^{\circ}_{\alpha\alpha} + \varepsilon^{\circ}_{\alpha\beta}\varepsilon^{\circ}_{\alpha\beta} \right], \tag{3.30}$$

which equals $2\pi/\omega$ times the strain energy density of an isotropic elastic body with strains $\varepsilon^{\circ}_{\alpha\beta}$ and elastic moduli equal to the loss moduli of the viscoelastic body. However, when either material or geometric or both nonlinearities are considered, such an identification is not readily available. For infinitesimal deformations of a nearly incompressible viscoelastic body, $\nu \approx 0.5$, $\varepsilon^{o}_{\gamma\gamma} \approx 0$ and the first term in the bracket on the right-hand side of equation (3.30) is negligible as compared to the second term. Thus the energy dissipated in the visoelastic layer is predominantly due to its shearing deformations.

In a freely vibrating structural system composed of elastic and viscoelastic members, a measure of the energy dissipated during a cycle of deformation is the relative decrease in the amplitude of vibrations or the logarithmic decrement, δ^{ln}, defined as (Timoshenko, [48])

$$\delta^{ln} = ln(u^{\max}_{3(j)}/u^{\max}_{3(j+1)}) \tag{3.31}$$

where $u^{\max}_{3(j)}$ is the maximum displacement of a material point in the X_3-direction during the jth cycle of deformation. Here we have chosen the X_3-direction since the displacement in this direction is likely to be maximum. It is clear that in a continuous body the logarithmic decrement may vary

from point to point. A higher value of the logarithmic decrement implies that more of the energy stored in a freely vibrating body is dissipated during each cycle of deformation. This measure of energy dissipation is valid even when material and/or geometric nonlinearities are considered. For a nonlinear problem, the value of δ^{ln} may depend upon the cycle j of deformation. For problems studied herein, we have set $j = 2$. Note that δ compares amplitudes of two successive oscillations of a system and does not compare the amplitudes of oscillations obtained with and without an ACLD treatment.

The effectiveness of activating a PZT in an ACLD treatment can be measured by either one of the following two indices:

$$I_1 = 1 - \frac{|u_{3(1)}^{\max}(\text{PZTs activated})|}{|u_{3(1)}^{\max}(\text{PZTs not activated})|}, \tag{3.32}$$

$$I_2 = \frac{\delta^{\ell n}(\text{PZTs activated})}{\delta^{\ell n}(\text{PZTs not activated})} - 1. \tag{3.33}$$

Higher positive values of I_1 and I_2 indicate that actuating the PZTs enhances the energy dissipated in the viscoelastic layer.

3.2 Finite Element Formulation of the Problem

As noted earlier, our goal is to find x_i and ϕ from equations (3.2) and (3.4) subject to the initial and boundary conditions. Following Hughes [20] a weak formulation of these equations can be written as

$$\delta_{i\alpha}\delta_{i\beta}\int_\Omega \rho\ddot{u}_\alpha v_\beta d\Omega = \delta_{i\alpha}\left[\int_{\partial\Omega_t} f_i v_\alpha dS - \int_\Omega T_{i\beta} v_{\alpha,\beta} d\Omega\right], \tag{3.34}$$

$$\int_\Omega D_\alpha \psi_{,\alpha} d\Omega = \int_{\partial\Omega_c} q\psi dS, \tag{3.35}$$

where $\mathbf{v}$ and ψ are smooth test functions that vanish on parts of the boundary where essential boundary conditions and the electric potential are prescribed respectively. Furthermore Ω is the region occupied by the hybrid structure, $\partial\Omega_t$ the part of the boundary where surface tractions $f_i (f_i = T_{i\alpha}N_\alpha)$ are prescribed, and $\partial\Omega_c$ the part of the boundary where the surface charge density q ($q = D_\alpha N_\alpha$), is specified. For the present problem, $q = 0$ on $\partial\Omega_c$. When $\mathbf{v}$ is regarded as a virtual displacement, then the left-hand side of eqn. (3.34) equals the virtual work of inertia forces, and the two terms on the right-hand side represent the virtual work of surface tractions and internal stresses. For the host structure and the viscoelastic layer, internal stresses $T_{i\alpha}$ depend upon the mechanical deformations but for the PZT these also depend upon the electric field. Substitution for $\mathbf{S}$ from (3.7), (3.8) and $(3.9)_1$ into (3.6) and the result into (3.34), and for $\mathbf{D}$ or $\boldsymbol{\pi}$ from $(3.9)_2$ into (3.12) and the result into (3.35) yields coupled equations for the determination of mechanical displacements $\mathbf{u}$ and the electric potential ϕ. As stated earlier, initial displacements and velocities vanish, and the pertinent boundary conditions are given in (3.27) and in a few lines preceding (3.27).

The domain Ω is discretized into the union of 8-noded disjoint brick elements Ω_e and ensuring that each element is made of a monolithic material. This is easily achieved by placing nodes on an interface between two dissimilar materials. Whereas prescribed essential boundary conditions are to be satisfied after equations at the element level have been assembled, the interface continuity conditions (3.26) are satisfied during the assembly of these equations. Referring the reader to Hughes [20] for details, we note that equations (3.34) and (3.35) yield the following set of coupled nonlinear ordinary differential-algebraic equations.

$$\mathbf{M}\ddot{\mathbf{u}} = \mathbf{F}^{\text{ext}}(t) - \mathbf{F}^{\text{int}}(\mathbf{u}(t), \phi(t)), \tag{3.36}$$

$$\mathbf{P}^{\text{int}}(\mathbf{u}(t), \phi(t)) = \mathbf{0}, \tag{3.37}$$

where

$$\mathbf{F}^{\text{int}} = \sum_e \int_{\Omega_e} \mathbf{B}^T \mathbf{T} d\Omega, \tag{3.38}$$

$\mathbf{B}$ is the 9×16 matrix relating the deformation gradient $x_{i,\alpha}$ to the nodal displacements, the summation in equation (3.38) extends over all elements in the mesh, $\mathbf{M}$ is the mass matrix, $\mathbf{u}$ the vector of nodal displacements in the hybrid structure, $\mathbf{F}^{\text{ext}}$ is the vector of nodal forces equivalent to externally applied surface tractions, and $\mathbf{P}^{\text{int}}$ is the nodal charge vector equivalent to the internal polarization. Note that only piezoelectric elements contribute to $\mathbf{P}^{\text{int}}$. In order to avoid computing the integral of the history of the strain tensor at a material point of a viscoelastic layer, we use constitutive relation (3.19) for the viscoelastic layer and evaluate η at each integration point from equation (3.20) which is integrated by the backward difference method. Integrals over an element, like the one on the right-hand side of equation (3.38), are evaluated by using the $2\times2\times2$ quadrature rule.

Equation (3.36) is integrated by the central-difference method, equation (3.20) at each quadrature point by the backward-difference method, and the nonlinear algebraic equations (3.37) are solved by the Newton-Raphson technique. Since the backward-difference method is unconditionally stable, the time step is controlled by the central-difference method which is explicit and conditionally stable. Accordingly, we take

$$\Delta t = 1.8/\omega_{\max} \tag{3.39}$$

where $\omega_{\max}$ is the maximum frequency of free vibration of the discretized structure. For a nonlinear problem the structural stiffness varies with its deformations and hence $\omega_{\max}$ will be a function of time resulting in uneven time steps. We employ the following recursive relation to compute nodal values of mechanical displacements at successive times:

$$\mathbf{u}(t_{n+1}) = \Delta t_2 \left[\mathbf{M}^{-1}(\mathbf{F}^{\text{ext}}(t_{n+1}) - \mathbf{F}^{\text{int}}(t_{n-1})) \frac{\Delta t_1 + \Delta t_2}{2} + \left(\frac{1}{\Delta t_1} + \frac{1}{\Delta t_2} \right) \mathbf{u}(t_n) + \frac{\mathbf{u}(t_{n-1})}{\Delta t_1} \right], \tag{3.40}$$

where $\Delta t_1 = t_n - t_{n-1}$ and $\Delta t_2 = t_{n+1} - t_n$. For the hybrid laminated structure being studied, the number of nodal mechanical displacement degrees of freedom is considerably more than the nodal electric potentials. The aforestated explicit/implicit technique of analyzing the problem is

computationally more effective both in terms of the storage and the CPU time requirements than the purely implicit technique.

Note that the problem is being analyzed in the time domain rather than the frequency domain.

3.3 Computation and Discussion of Results

The finite element code developed by Batra and Liang [27] was modified to include the viscoelastic material behavior. Changes made in the code were verified by comparing computed results for the forced one-dimensional deformations of a viscoelastic bar with the analytical solution of the problem. When comparing the performance of extension mode and shear mode actuators in ACLD treatments, following values were assigned to various material parameters. We will find below the optimum value of the relaxation time τ and assign to it that value.

Host structure (Aluminum):

$$E = 70.3\,\mathrm{GPa},\ \nu = 0.34,\ \rho_0 = 2,700\,\mathrm{kg/m^3}; \tag{3.41}$$

Viscoelastic layer:

$$E = 298\ \mathrm{MPa},\ \nu = 0.49,\ \chi = 0.9,\ \rho_0 = 1,105\,\mathrm{kg/m^3}; \tag{3.42}$$

PZT material:

$$\begin{aligned}
&c_1 = 23.1\,\mathrm{GPa},\ c_2 = 33.944\,\mathrm{GPa},\ c_3 = 0.1996\ \mathrm{GPa},\ c_4 = -22.535\,\mathrm{GPa},\ c_5 = 33.49\,\mathrm{GPa},\\
&e_1 = 8.67544\,\mathrm{C/m^2},\ e_2 = 1.85657\,\mathrm{C/m^2},\ e_3 = -9.77768\,\mathrm{C/m^2},\\
&\varepsilon_0 = 8.8419\times 10^{-12}\,\mathrm{C/V-}m,\ \varepsilon_1 = 1.0\times 10^{-10}\,\mathrm{C/V-}m,\ \varepsilon_2 = -17.956\times 10^{-10}\,\mathrm{C/V-}m,\\
&\nu_4 = -0.903\times 10^{-4}\mathrm{N/V^2},\ \nu_{12} = 0.305\times 10^{-4}\mathrm{N/V^2},\\
&\rho_0 = 7,500\,\mathrm{kg/m^3}.
\end{aligned} \tag{3.43}$$

The ratio of Young's modulus for the aluminum and the instantaneous Young's modulus for the viscoelastic layer is nearly 200. Young's modulus in the longitudinal direction for the PZT also equals approximately 200 times the instantaneous Young's modulus for the viscoelastic layer. Thus for both the extension mode and the shear mode configurations, a soft viscoelastic layer is sandwiched between two rather stiff layers.

Unless stated otherwise results presented and discussed below are for $\nu_4 = \nu_{12} = 0$, i.e., without the consideration of W^2 terms in equation (3.21).

3.3.1 Determination of the fundamental frequency

We determine the first natural frequency of the structure with the goal of exciting it at that frequency and then annulling its vibrations. The procedure to find the first natural frequency was validated by finding the natural frequencies of a simply supported 3-layer laminated square elastic plate with each layer made of an orthotropic material; the elastic constants of the bottom and the top layers were set equal to β times those of the middle layer. The elastic constants of the middle layer are

$$\mathbf{C} = \begin{bmatrix} 1 & 0.23319 & 0.010776 & 0 & 0 & 0 \\ 0.23319 & 0.543103 & 0.098276 & 0 & 0 & 0 \\ 0.010776 & 0.098276 & 0.530172 & 0 & 0 & 0 \\ 0 & 0 & 0 & 0.26681 & 0 & 0 \\ 0 & 0 & 0 & 0 & 0.159914 & 0 \\ 0 & 0 & 0 & 0 & 0 & 0.262931 \end{bmatrix} \text{MPa}$$

and the mass density of each layer was taken to be $1,000\ \text{kg/m}^3$. Each side of the plate equaled 10 cm, and the thickness of the middle layer equaled 0.8 cm and that of each of the top and the bottom layers equaled 0.1 cm. The plate was excited by applying a uniformly distributed normal traction of $40\ \text{kN/m}^2$ in the central 4% of the surface area of the top surface of the plate. Due to the symmetry

about the two centroidal axes, only a quarter of the plate was modeled. The top and the bottom layers were divided into 8-node brick elements of size $1 \times 1 \times 0.1$ cm, and the size of the element in the middle layer equaled $1 \times 1 \times 0.4$ cm. By using $\Delta t = 20$ μs, time history of the vertical displacement of the centroid of the top surface of the layered plate was computed for 1 s which was analyzed by using the fast Fourier transform (FFT) to compute the natural frequencies. The variation of the first natural frequency with β is plotted in Fig.3.3 along with the analytical solution of Srinivas and Rao [43], and the natural frequency obtained from the Kirchhoff plate theory as reported by Srinivas and Rao. For each value of β, the computed fundamental frequency exceeds the analytical one by at most 4%. A finer mesh ($10 \times 10 \times 6$ elements) and normal tractions applied to a larger (16%) part of the surface area did not alter the computed natural frequency. Whereas for a homogeneous orthotropic plate with $\beta = 1$, the Kirchhoff plate theory gives acceptable value of the first natural frequency for the plate of aspect ratio 10, the difference between the analytical solution and that obtained from the Kirchhoff plate theory increases noticeably with an increase in the value of β. Kirchhoff's plate theory proposed for a homogeneous plate is not expected to give good results for composite laminated plates.

The classical laminated plate theory (CLPT) gives the following expression for the fundamental frequency of a simply supported rectangular laminated plate of sides a and b and thickness h.

$$\omega_{mn}^{\mathrm{CLPT}} = \left(\frac{\pi^2}{a^2}\frac{D_{11}}{2\rho h}\right)^{\frac{1}{2}} \left[m^4 + 2\frac{D_{12}+2D_{66}}{D_{11}}m^2\left(\frac{a}{b}n\right)^2 + \frac{D_{22}}{D_{11}}\left(\frac{a}{b}n\right)^4\right]^{\frac{1}{2}}.$$

Here D_{11}, D_{22}, D_{12} and D_{66} are the bending rigidities, and m and n are integers. For a square plate with $a/h = 10$, and $m = n = 1$, we get

$$\omega_{11}^{\mathrm{CLPT}} = \frac{\pi}{a\sqrt{2\rho h}}[D_{11} + 2D_{12} + 4D_{66} + D_{22}]^{\frac{1}{2}}.$$

Whereas the CLPT neglects effects of transverse shear deformations and rotary inertia, both the analytical solution of Srinivas and Rao [43] and the numerical solution obtained here account for these effects. For a laminated plate of aspect ratio 10, transverse shear effects may not be

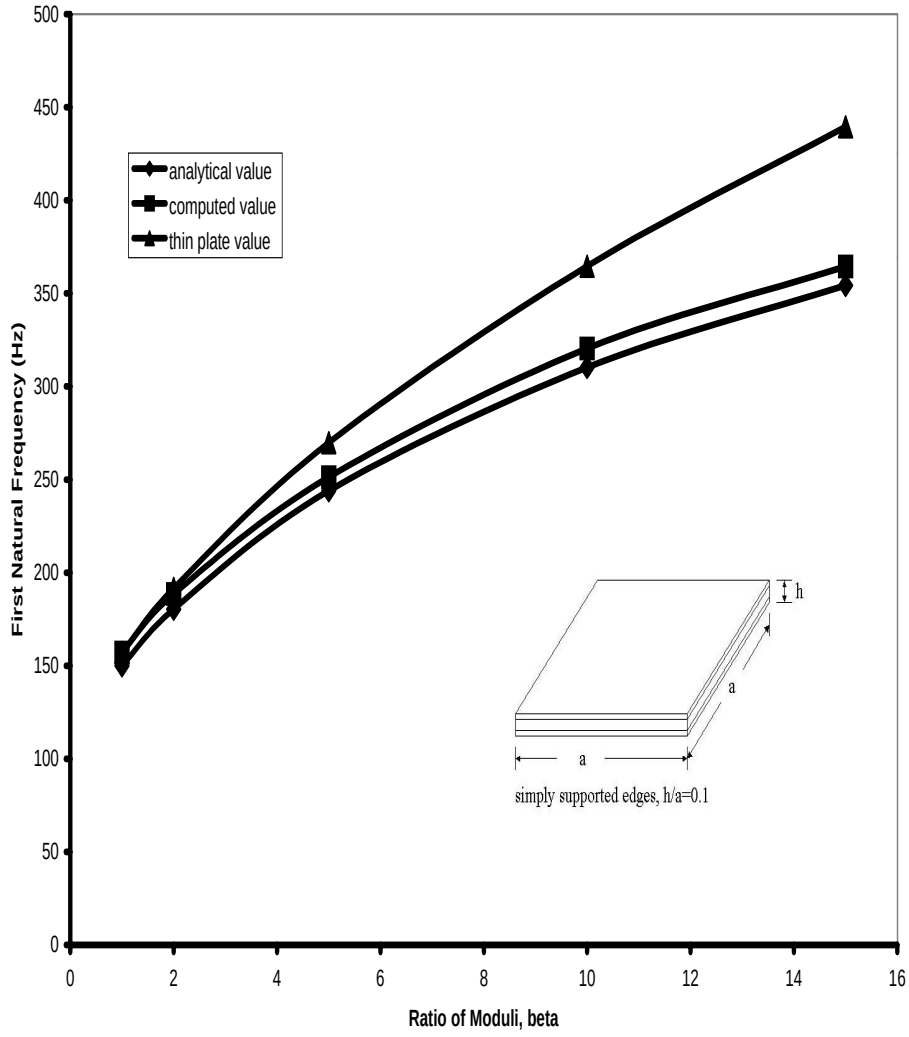

Figure 3.3: Comparison of the computed fundamental frequency of free vibration of a simply supported hybrid laminated plate with those obtained from the analytical solution of three-dimensional elasticity equations, and from the Kirchhoff plate theory.

negligible. The consideration of shear deformations and rotary inertia lowers the fundamental frequency of a plate.

In order to analyze the damping enhanced by activating the PZTs in an ACLD treatment, we first find the natural frequencies of the systems exhibited in Figs. 3.1 and 3.2 by using the aforementioned technique. In each case, a uniform tangential traction of 2 MPa is applied to the unclamped edge of the aluminum plate for a short while and then removed. Due to the symmetry of the problem about the plane $x_2 = 1$ cm, only one-half of the problem is studied. Using $\Delta t = 0.5\mu$s, time history of the transverse displacement of point C is computed; point C has coordinates (15, 1, 3.5) for the shear mode configuration of Fig. 3.1 and (15, 1, 0) for the extension mode configuration of Fig. 3.2. The fundamental frequency of the system was determined by taking the FFT of the displacement time history. The dependence of the fundamental frequency upon the thickness of the viscoelastic layer is listed in Table 1. In computing these, χ in equation (3.8) was set equal to 0.0; thus the energy dissipation in the viscoelastic layers was neglected. As is clear from the tabulated values, with an increase in the thickness of each of the two viscoelastic layers from 0.1 to 1.0 cm, the fundamental frequency of the system decreases from 6.472 kHz to 5.089 kHz for the shear mode configuration but it decreases from 9.174 kHz to 7.791 kHz for the extension mode configuration. Note that Young's modulus in the longitudinal direction for the shear mode PZT is more than that for the extension mode PZT. Because PZT layers are farthest from the midsurface for the extension mode configuration, the effective stiffness of the extension mode configuration is more than that of the shear mode configuration. The fundamental frequencies obtained from the Euler beam theory for the shear mode and the extension mode configurations equal 18.4 kHz and 15.1 kHz respectively for $h_{VE} = 1$ cm; however, for $h_{VE} = 0.1$ cm, each of these values equals 12.9 kHz. For 2.14 $\leq$ L/H $\leq$ 3, the Euler beam theory is not expected to give good values of the fundamental frequency.

Table 1. For different values of the thickness of the viscoelastic layer, first natural frequency of the systems shown in Figs. 3.1 and 3.2.

Thickness of the viscoelastic layer (cm)	First natural frequency (kHz)	
	Shear mode PZT	Extension mode PZT
0.1	6.472	9.174
0.2	5.906	8.734
0.3	5.655	8.482
0.4	5.529	8.294
0.5	5.404	8.168
0.6	5.341	8.074
0.7	5.278	7.980
0.8	5.215	7.917
0.9	5.152	7.854
1.0	5.089	7.791

An increase in the thickness of each of the viscoelastic layers implies that either the aluminum layers or the PZT layers are located farther from the midsurface of the composite plate, and the total thickness of the plate increases. The Kirchhoff plate theory suggests that the effective stiffness of the structure will increase and thus the first natural frequency should increase with an increase in the thickness of the viscoelastic layer. However, results reported in Table 1 are in the opposite direction. As noted earlier for a plate of aspect ratio 10, the difference in the first natural frequency computed from the Kirchhoff plate theory and the analytical one increases with an increase in the ratio of the moduli of the layers. Since the instantaneous Young's modulus for the viscoelastic layer is 1/200 times that of either the aluminum or the PZT, it is very likely that the vertical displacements of similarly situated points in the aluminum and the PZT layers are loosely coupled.

In order to delineate this, we have plotted in Fig.3.4, for the shear mode configuration, the time history of the normalized relative difference in the transverse displacements of points D (15, 1, 0) and C (15, 1, 2.5+h_{VE}) where h_{VE} is the thickness of the viscoelastic layer. It is clear that this difference increases with an increase in h_{VE}. However, the maximum value of this difference is less than 1.2%. Therefore, the different layers move together in the vertical direction.

Table 2. First natural frequency of the system of Fig. 3.1 for different thicknesses of each viscoelastic layer and for different values of the shear modulus.

Thickness of each viscoelastic layer (cm)	First natural frequency in kHz for shear modulus (GPa) equal to				
	0.1	0.3	1	3	10
0.1	6.472	7.854	9.174	9.927	10.304
0.4	5.529	6.597	8.294	9.865	11.058
0.7	5.278	6.220	8.043	9.990	11.750
1.0	5.089	6.032	7.854	10.053	12.315

We determined the first natural frequency of the shear mode configuration for different thicknesses of the viscoelastic layers by varying their shear modulus from 0.1 GPa to 10 GPa; these results are summarized in Table 2. It is evident from these values that when the shear modulus of the viscoelastic layer is nearly one-tenth (or more) of that of the surrounding layers, then the computed natural frequencies agree with the trends predicted by the CLPT.

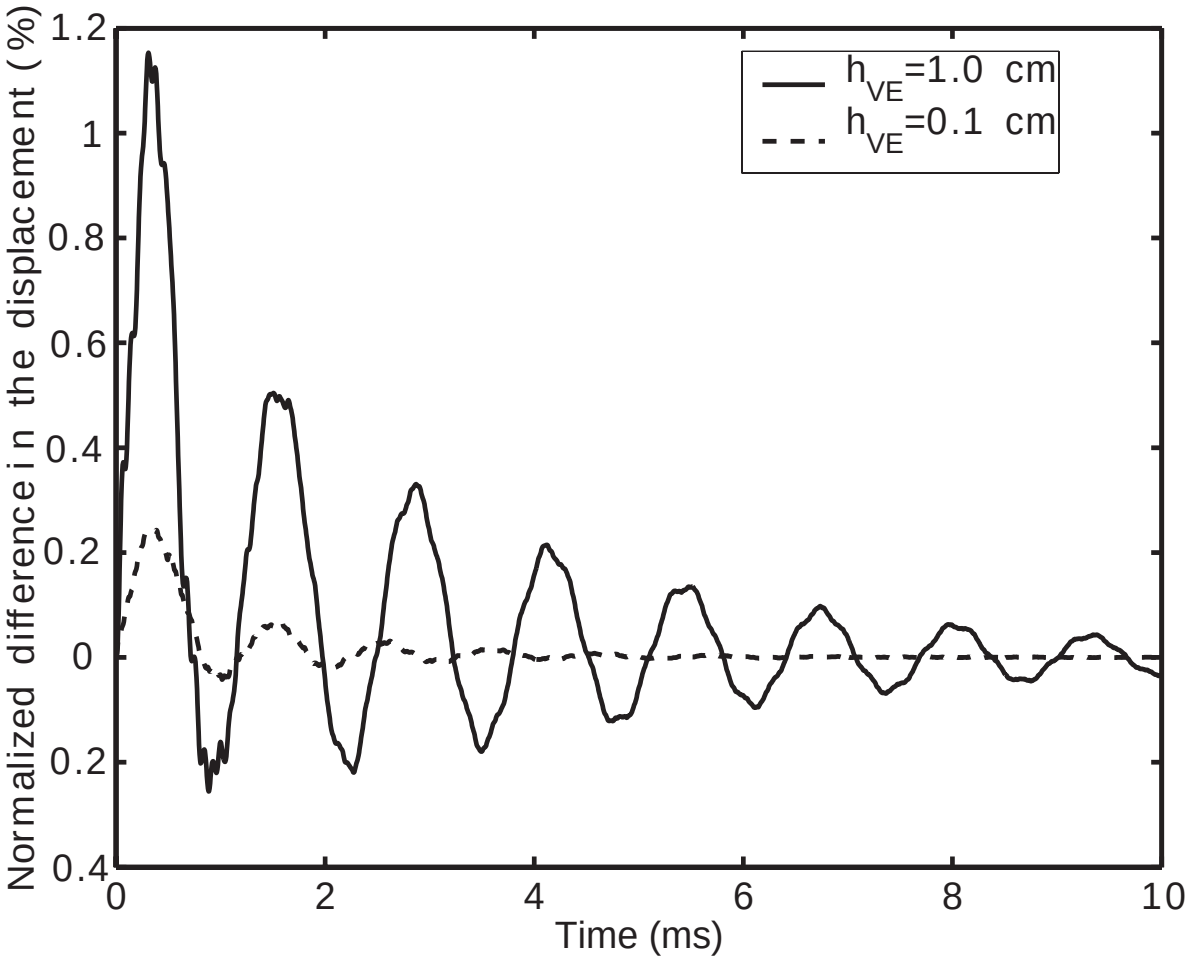

Figure 3.4: Time history of the normalized difference between the transverse displacements of the tips of the aluminum and the PZT layers for two values of the thickness of the intervening viscoelastic layer.

3.3.2 Analysis of Damping

We now set $\chi = 0.9$ and scrutinize damping induced by the ACLD treatment. In each case, $p_o = 0.2MPa$ and ω in equation (3.27) equals the first natural frequency of the system listed in Table 1. Because of the nonzero value of χ, the first natural frequency of the composite plate will be slightly different from that listed in Table 1. The load is applied for $0 \leq t \leq \pi/\omega$ and equals zero for $t \geq \pi/\omega$. For the extension mode actuators with PZTs poled in the x_3-direction, the voltage applied to the upper surface of the top PZT layer and to the lower surface of the bottom PZT layer equals the smaller of $4 \times 10^8 |u_3^C| V$ and 5 kV for $u_3^C > 0$ and the other surfaces of the PZT layers are grounded. Here u_3^C equals the transverse displacement of point C (cf. Fig. 3.1 and 3.2) in meters. For $u_3^C < 0$, the voltage given by $\min\{4 \times 10^8 |u_3^C|,\ 5\ \mathrm{kV}\}$ is applied to the lower surface of the top PZT layer and to the upper surface of the bottom PZT layer and the other surfaces of the PZT layers are grounded. Numerical experiments gave the optimum value of the gain factor to be 4×10^8 V/m. For the shear mode PZT actuator poled in the x_1-direction, the electric potential applied to its lower surface equals the minimum of $4 \times 10^8 |u_3^C|$ and 10kV with the upper surface grounded when $u_3^C > 0$. For $u_3^C < 0$, the lower surface of the PZT is grounded and the voltage equal to $\min\{4 \times 10^8 |u_3^C|, 10\mathrm{kV}\}$ is applied to its upper surface. We note that the electric strength of most commercially available PZTs is 2 kV/mm, and we are limiting it to 1 kV/mm. Since the thickness of the PZT layer is much smaller than its length, a uniform voltage difference applied to its surfaces $x_3 = \mathrm{const.}$ will produce a uniform electric field in the x_3-direction. However, deformations of the PZT layer will also induce an electric field. Both the direct and the converse piezoelectric effects are included in the analysis of the problem.

Determination of the optimum value of the relaxation time

For $h_{VE} = 1.0$ cm, $\omega_1 = 5.089$ kHz and the ACLD treatment with the shear mode PZT arrangement, computed values of the logarithmic decrement for different values of the relaxation time of the viscoelastic layer are listed in Table 3. Note that no voltage difference is applied to the major surfaces of the PZT layer.

Table 3. Variation of the logarithmic decrement with the relaxation time of the viscoelastic layer

Relaxation time τ	Logarithmic decrement δ^{ln}
$0.25/\omega_1$	0.1918
$0.5/\omega_1$	0.3134
$1/\omega_1$	0.3688
$2/\omega_1$	0.271
$4/\omega_1$	0.1574

Thus, as stated above in lines preceding equation (3.18), energy dissipated in the viscoelastic layer and hence the logarithmic decrement is maximum when $\tau = 1/\omega_1$ for the system excited at the fundamental frequency.

Determination of the optimum value of χ

With $\tau = 1/\omega_1$, we then varied χ between 0.9 and 0.5. Values of the logarithmic decrement so obtained are listed in Table 4. It is clear from these values that δ decreases monotonically with a decrease in the value of χ. Henceforth we took $\chi = 0.9$ and $\tau = 1/\omega_1$ for both the shear mode and

the extension mode ACLD treatments.

Table 4. Variation of the logarithmic decrement with the factor χ in the constitutive relation for the viscoelastic material.

χ	δ^{ln}
0.9	0.3688
0.8	0.3198
0.7	0.2736
0.6	0.2296
0.5	0.1875

Comparison of damping induced by the shear mode and the extension mode actuators

Figures 3.5 and 3.6 depict for the shear and the extension mode configurations and $h_{VE} = 1$ cm the time history of the transverse deflection of point C with and without the activation of the PZTs. It is clear that in each case the transverse deflection of point C decreases faster when an electric potential difference is applied across the faces of the PZT layers. Also, the time periods are shortened by the actuation of the PZTs and the decrease in the time period is more for the shear mode than that for the extension mode configurations. For the same intensity of the tangential traction applied at the unclamped edge for $0 < t < \pi/\omega_1$, the transverse displacement of point C for the shear mode configuration is more than twice of that for the extension mode configuration. Because of the difference in the values of ω_1 for the two configurations, the impulse imparted to the shear mode configuration is 1.53 times that given to the extension mode configuration. Also, values of the first natural frequency listed in Table 1 suggest that the effective stiffness of the extension mode configuration is higher than that of the shear mode one.

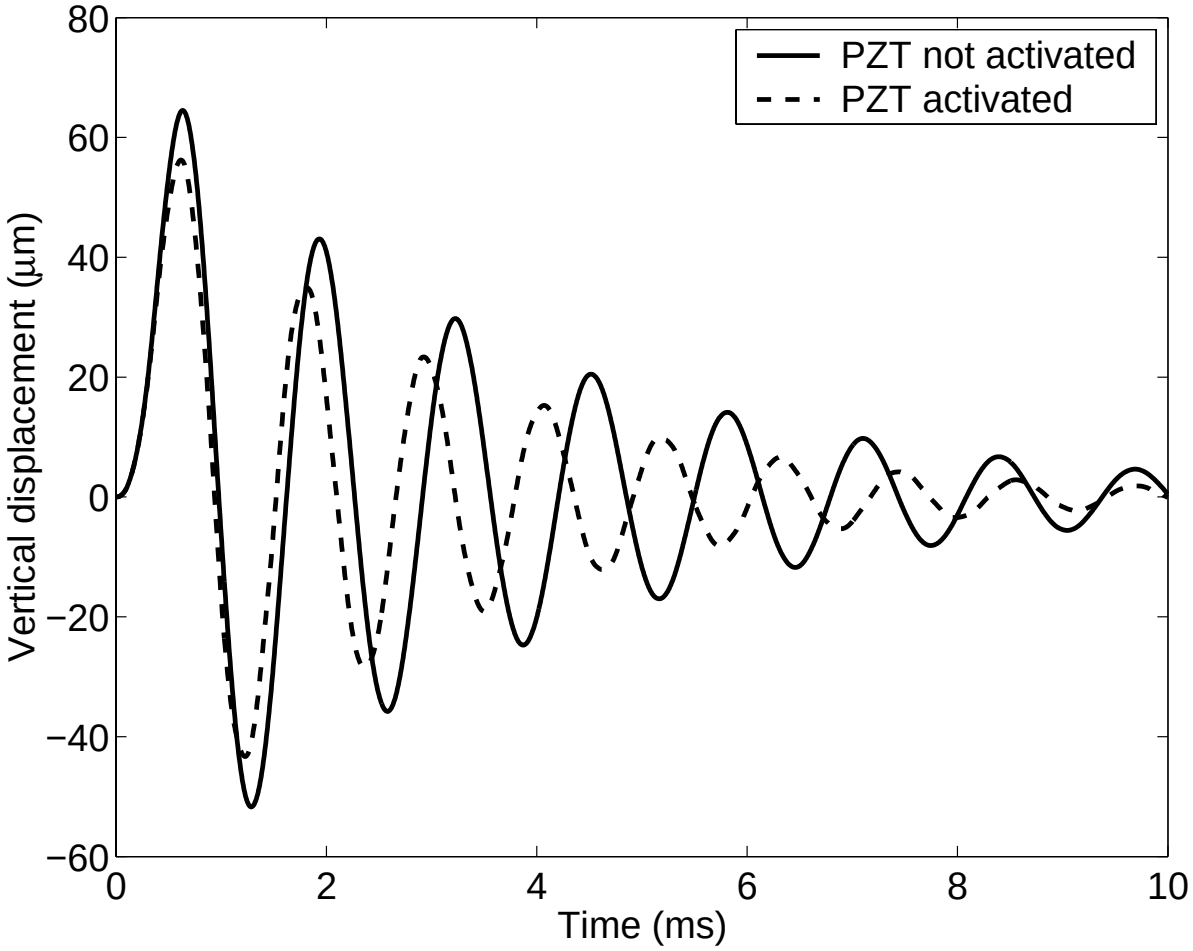

Figure 3.5: Time histories of the transverse displacement of point C with and without the application of an electric potential difference across the faces of the PZT layers for the shear mode configuration.

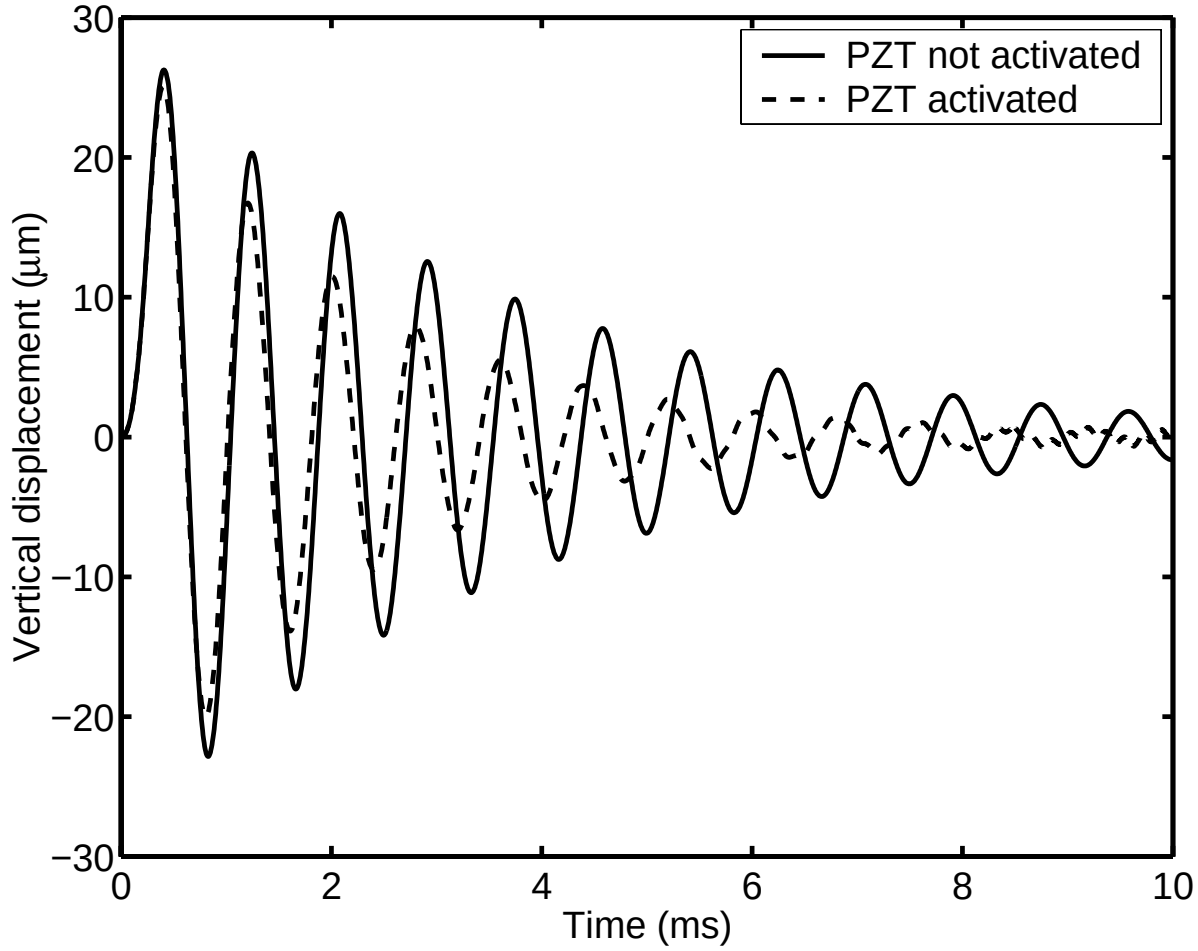

Figure 3.6: Time histories of the transverse displacement of point C with and without the application of an electric potential difference across the faces of the PZT layers for the extension mode configuration.

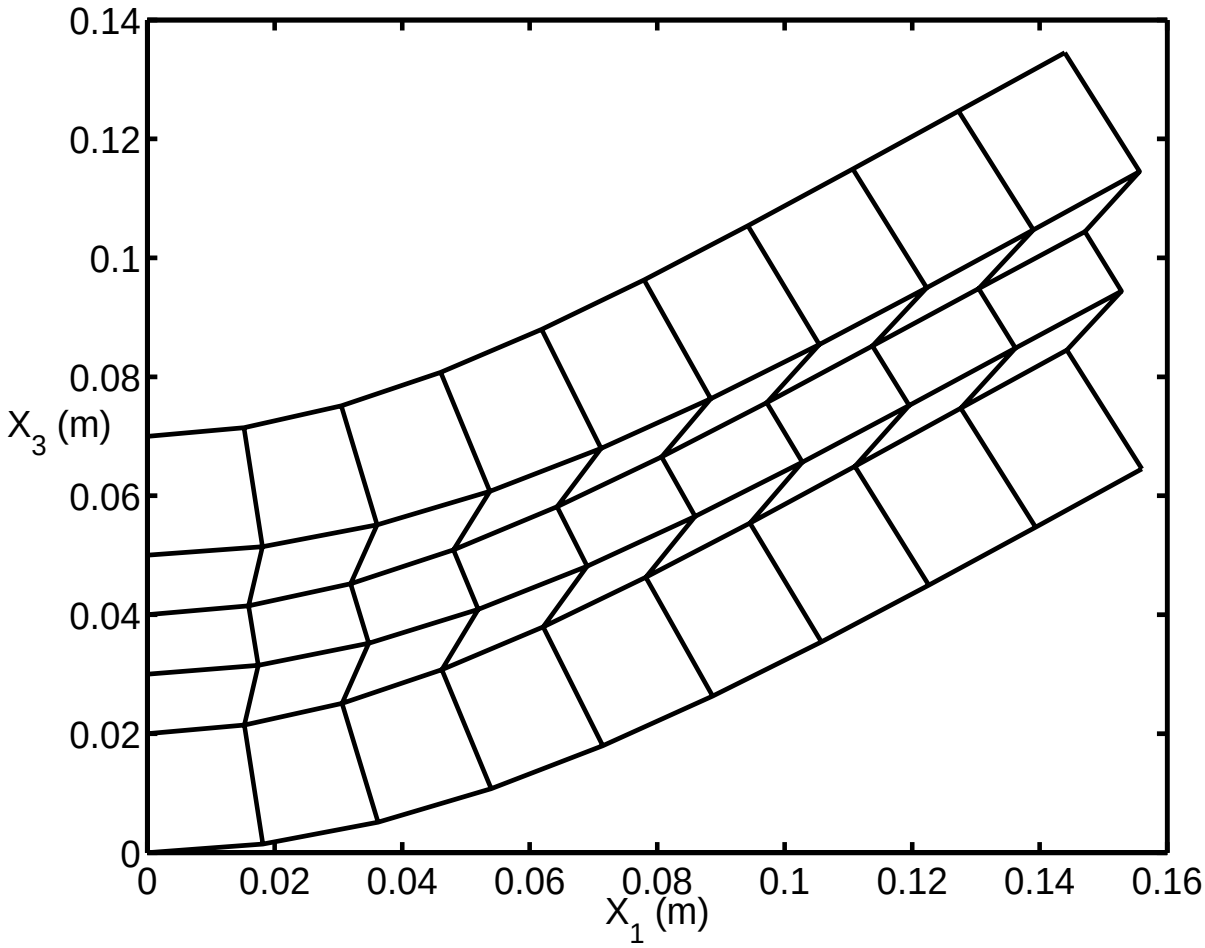

Figure 3.7: Deformed shape of the laminated hybrid plate for the shear mode PZT configuration at $t = 635$ μs. Displacements have been magnified by a factor of 1000.

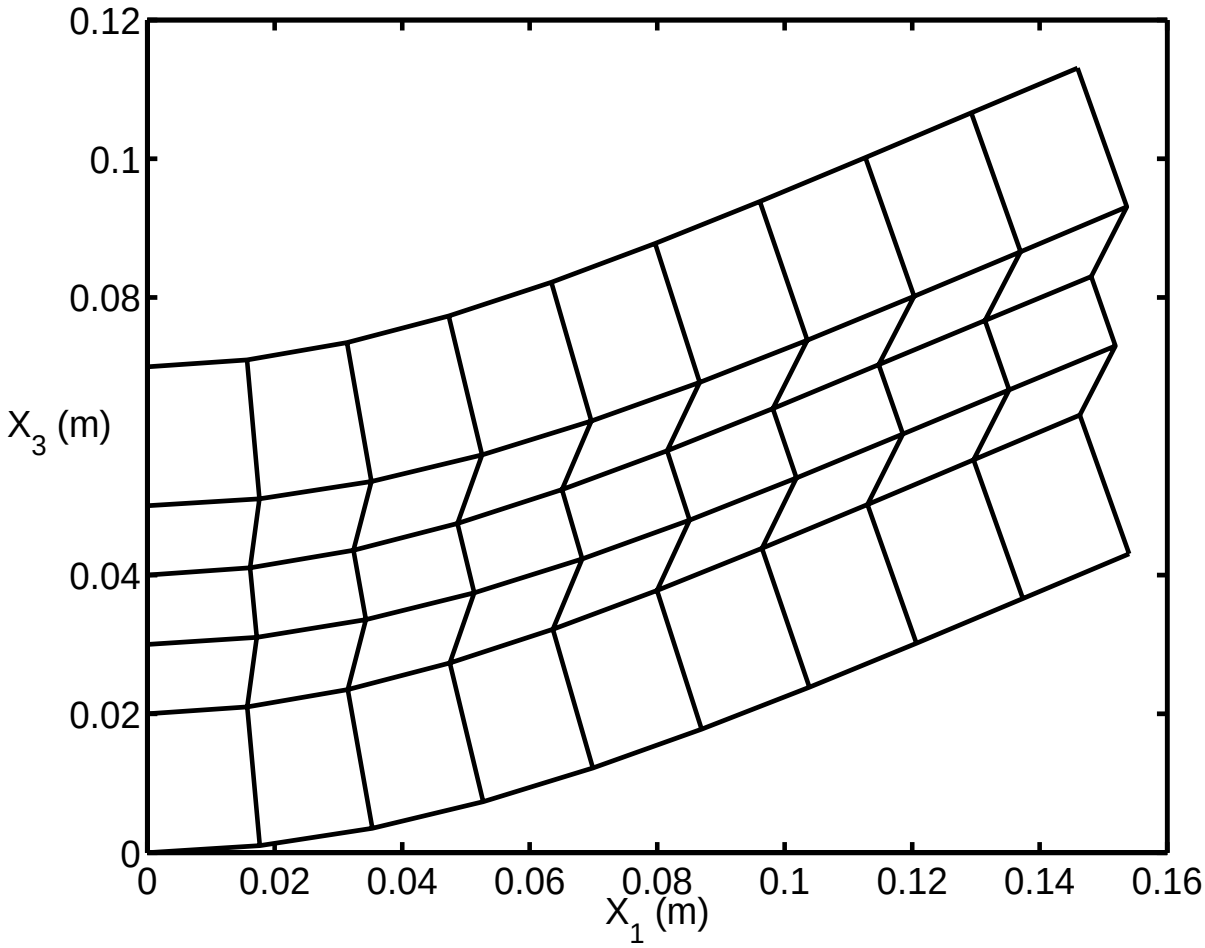

Figure 3.8: Deformed shape of the laminated hybrid plate for the shear mode PZT configuration at $t = 1935$ μs. Displacements have been magnified by a factor of 1000.

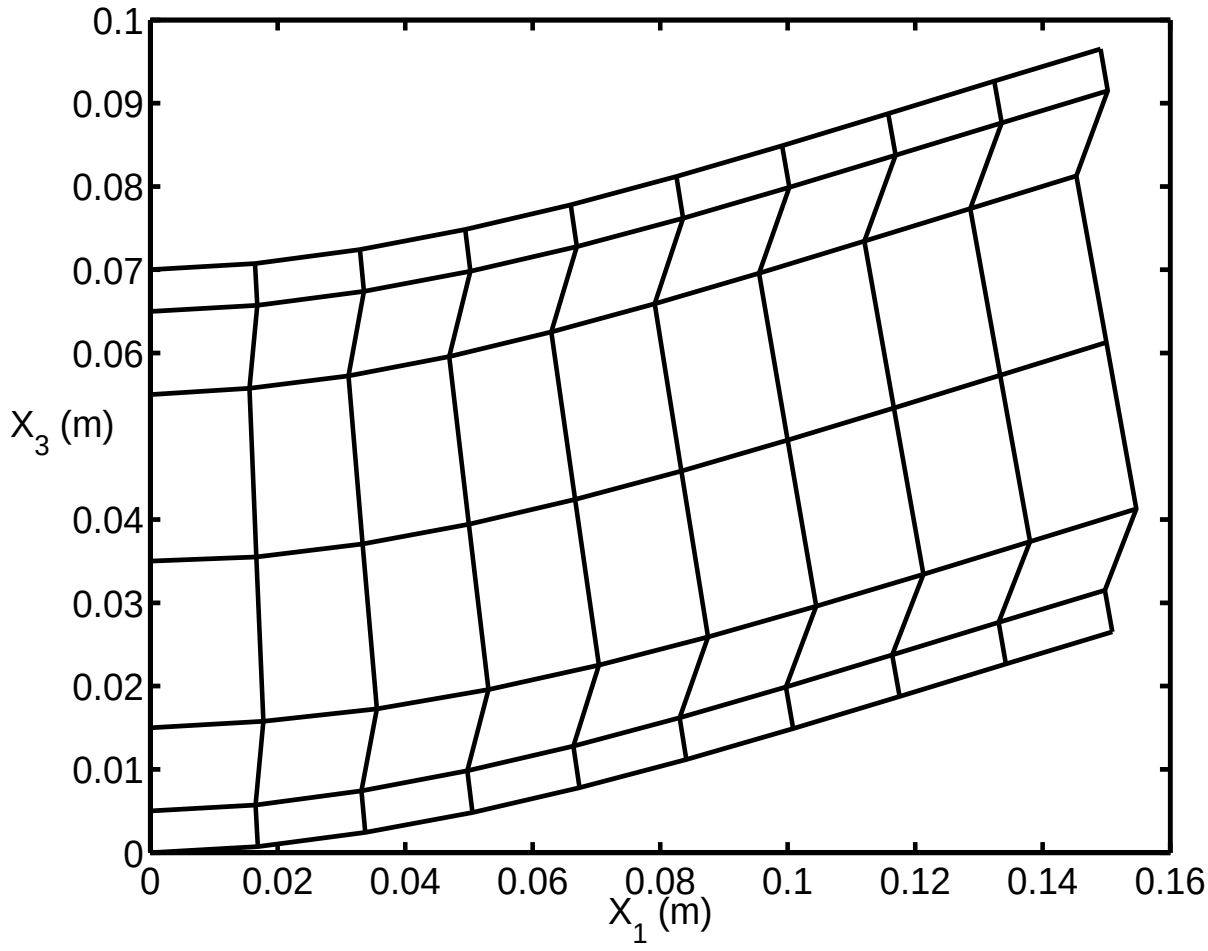

Figure 3.9: Deformed shape of the laminated hybrid plate for the extension mode PZT configuration at $t = 410$ μs; displacements have been multiplied by 1000.

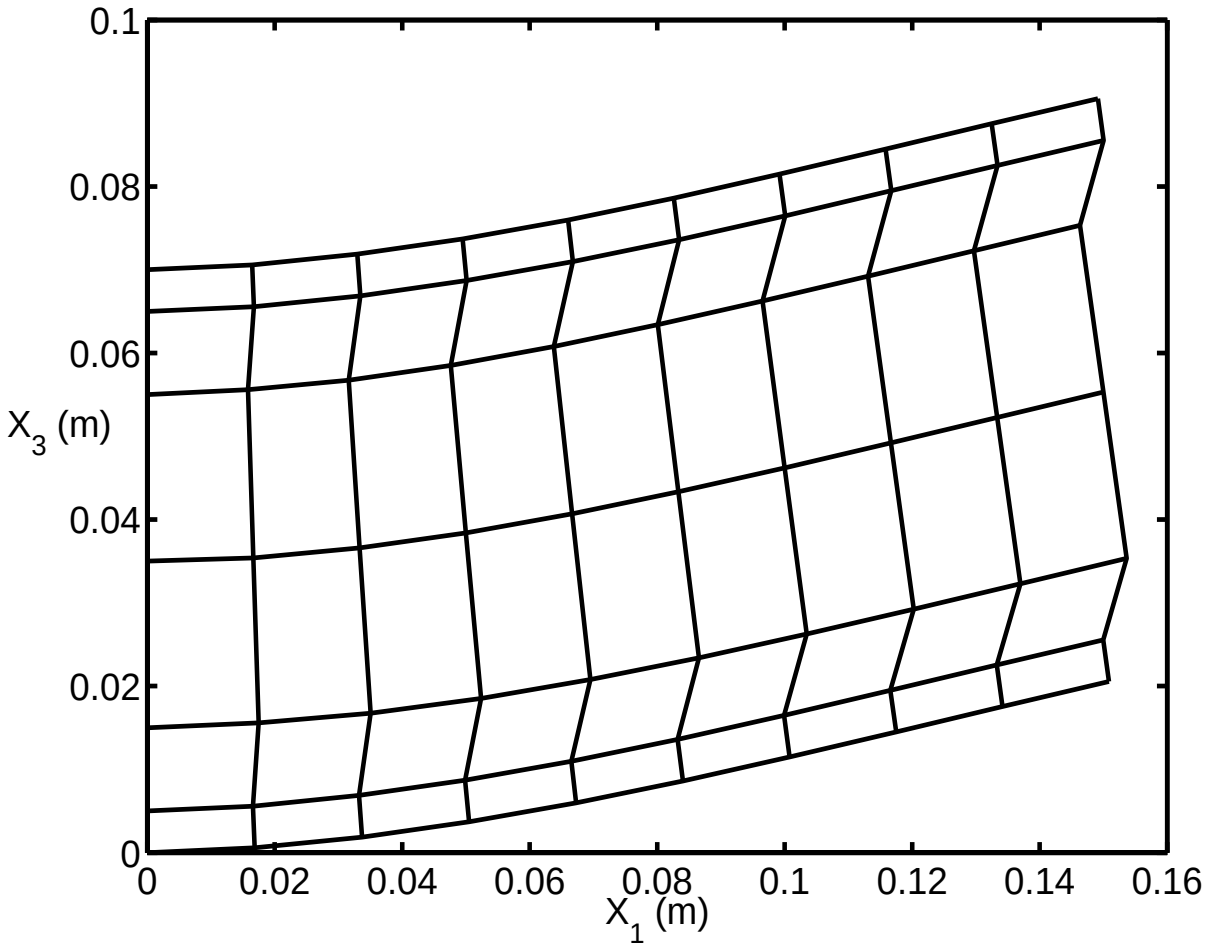

Figure 3.10: Deformed shape of the laminated hybrid plate for the extension mode PZT configuration at $t = 1245$ μs; displacements have been multiplied by 1000.

In Figures 3.7 and 3.8 we have plotted the deformed shapes at times $t = 635$ and 1935 μs respectively of the composite plate for the shear mode PZTs, and in Figs.3.9 and 3.10 at $t = 410$ μs and 1245μs for the extension mode PZTs. In each case displacements have been magnified by 1000 to clearly show the deformations of the viscoelastic layer. The times correspond to the instants of the first and the second maximum upwards vertical displacements of point C. In each of the corresponding Figs., shearing deformations of the viscoelastic layer are larger for the shear mode PZTs than those for the extension mode PZTs. Because of small strains induced, linear strain-displacement relations and linear constitutive relations should suffice even for the thick composite plate being studied herein.

For the shear mode PZTs, at time $t = 635\mu s$, among all the Gauss points in the PZTs, the maximum principal strain occurs at the point (3.71 cm, 0.71 cm, 8.81 cm) and the value is 6.1096×10^{-4}. Among all the Gauss points in the PZTs, the maximum principal stress occurs at the point (0.371 cm, 0.71 cm, 14.52 cm) and the value is 78.663 MPa. For the extension mode PZTs, at time $t = 410\mu s$, among all the Gauss points in the PZTs, the maximum principal strain occurs at the point (6.64 cm, 0.29 cm, 2.15 cm) and the value is 4.9927×10^{-4}. Among all the Gauss points in the PZTs, the maximum principal stress occurs at the point (6.86 cm, 0.71 cm, 14.52 cm) and the value is 92.136 MPa.

Effect of the thickness of viscoelastic layers

Figures 3.11, 3.12 and 3.13 evince the variation of the three measures $\delta^{\ell n}$, I_1 and I_2, of dissipation with the thickness of each one of the viscoelastic layers. For each value of the thickness, h_{VE}, of the viscoelastic layer, the logarithmic decrement for the shear mode actuator is considerably more than that for the extension mode actuator. For the extension mode ACLD treatment, $\delta^{\ell n}$ decreases

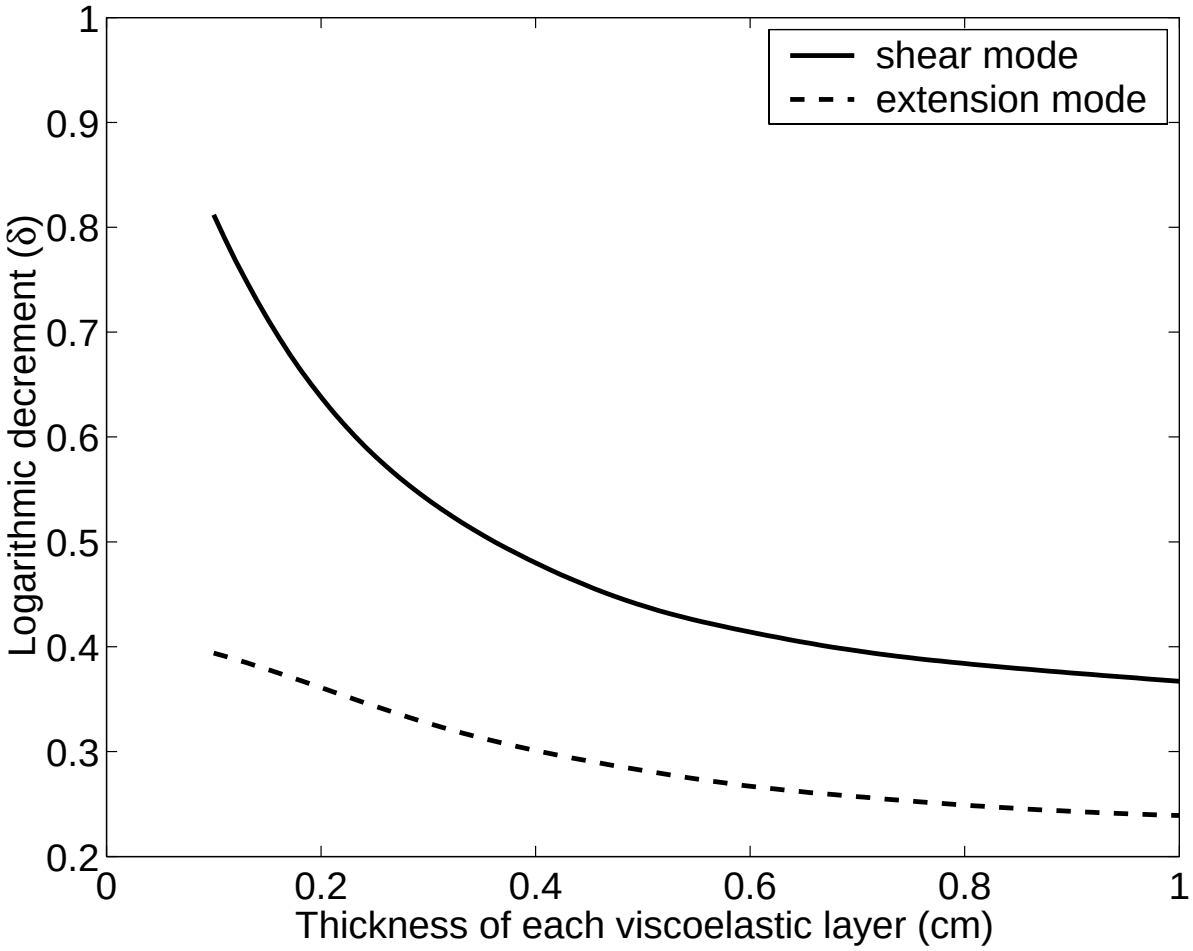

Figure 3.11: Dependence of the measure, $\delta^{\ell n}$, of energy dissipation upon the thickness of each one of the two viscoelastic layers.

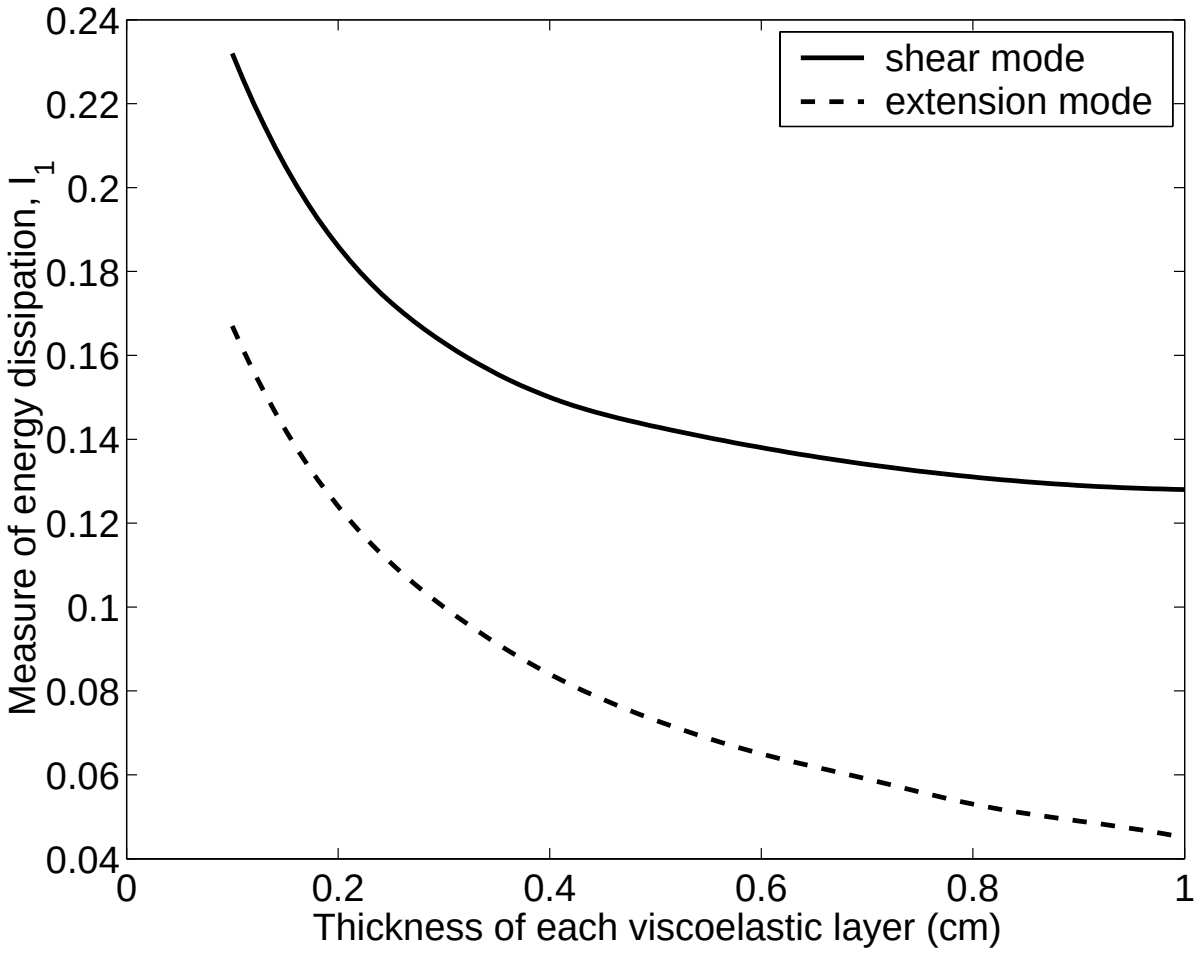

Figure 3.12: Dependence of the measure, I_1, of energy dissipation upon the thickness of each one of the two viscoelastic layers.

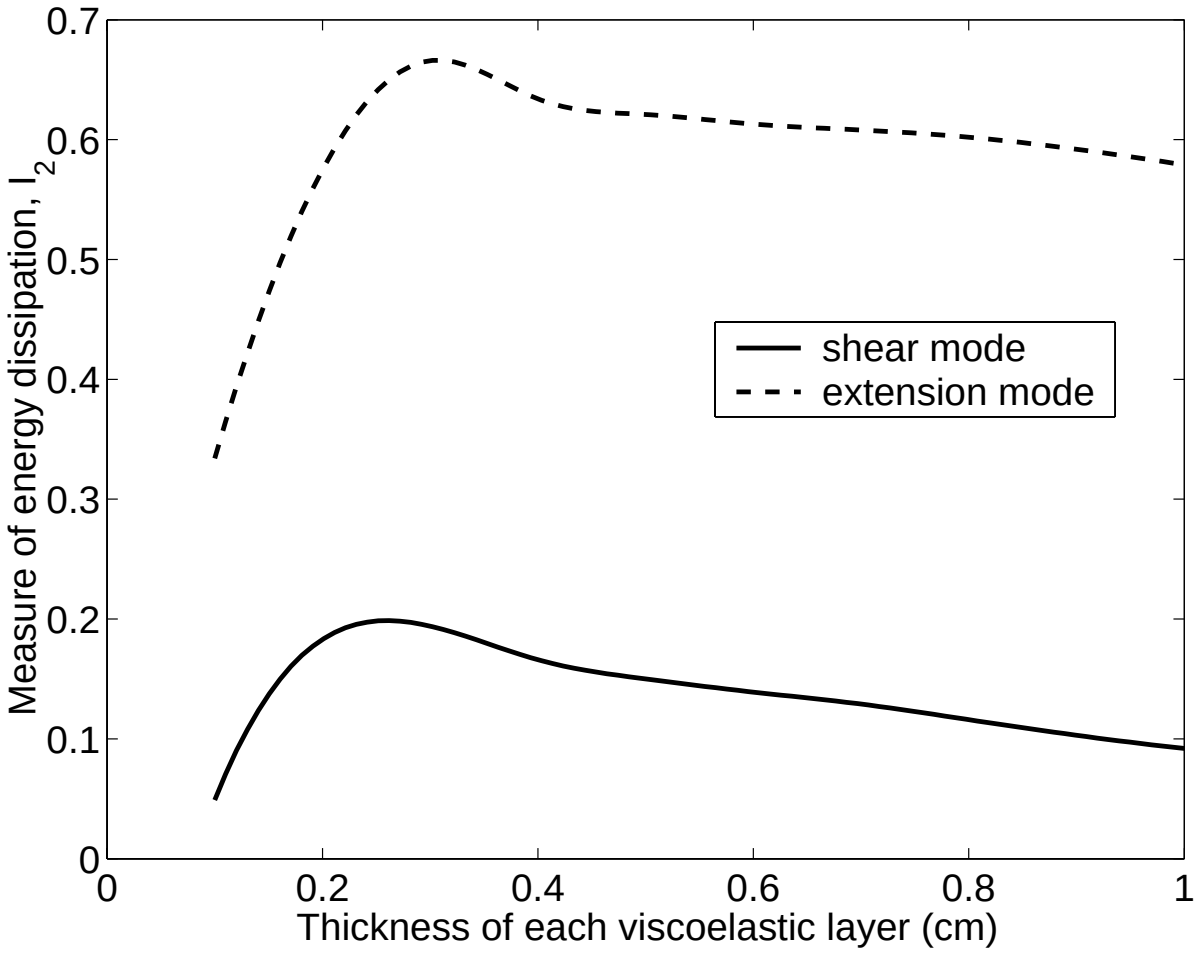

Figure 3.13: Dependence of the measure, I_2, of energy dissipation upon the thickness of each one of the two viscoelastic layers.

gradually from 0.394 for $h_{VE} = 0.1$ cm to 0.243 for $h_{VE} = 1.0$ cm, but for the shear mode ACLD treatment, $\delta^{\ell n}$ decreases rapidly from 0.812 to 0.638 when h_{VE} is increased from 0.1 cm to 0.2 cm but from 0.375 to 0.367 when h_{VE} is increased from 0.9 cm to 1.0 cm. This is because the maximum shear strain induced in the viscoelastic layer decreases rapidly when h_{VE} is increased from 0.1 to 0.2 cm but slowly for subsequent increase in the values of h_{VE}; it will be verified below. We recall that $\delta^{\ell n}$ does not indicate the improvement in damping caused by the activation of the PZTs but values of I_1 and I_2 signify this effect. Whereas I_1 has a simple interpretation, I_2 does not. Both for the shear and the extension mode actuators, I_1 decreases monotonically with an increase in the thickness of each viscoelastic layer. For each one of the ten values of h_{VE} considered, I_1 for the shear mode PZT actuator is higher than that for the extension mode PZT actuator. Thus shear mode PZTs are more effective in enhancing the shearing deformations of the viscoelastic layer which in turn increase the energy dissipation and the damping of vibrations of the system. However, I_2 attains a maximum value for $h_{VE} \approx 0.3$ cm for both the extension mode and the shear mode ACLD treatment.

We have plotted in Figs. 3.14 and 3.15 the longitudinal variation of the transverse shear strain in the viscoelastic layer for h_{VE} = 0.1, 0.4, 0.7 and 1.0 cm. In each case, the transverse shear strain monotonically increases from its lowest value in the element abutting the clamped edge to the maximum value near the midspan and stays uniform from there till the free edge of the plate. Also, the maximum transverse shear strain induced in the viscoelastic layer is largest for the thinnest layer. For the shear mode actuator, the maximum value of the transverse shear strain for $h_{VE} = 0.1$ cm is 2.3 times that for h_{VE} = 0.4 cm; for $h_{VE} = 0.1$ cm, the maximum transverse shear strain equals 0.28%. Thus the energy dissipated per unit volume will be highest for h_{VE} = 0.1 cm. Since the volume of the viscoelastic material is directly proportional to h_{VE}, the total

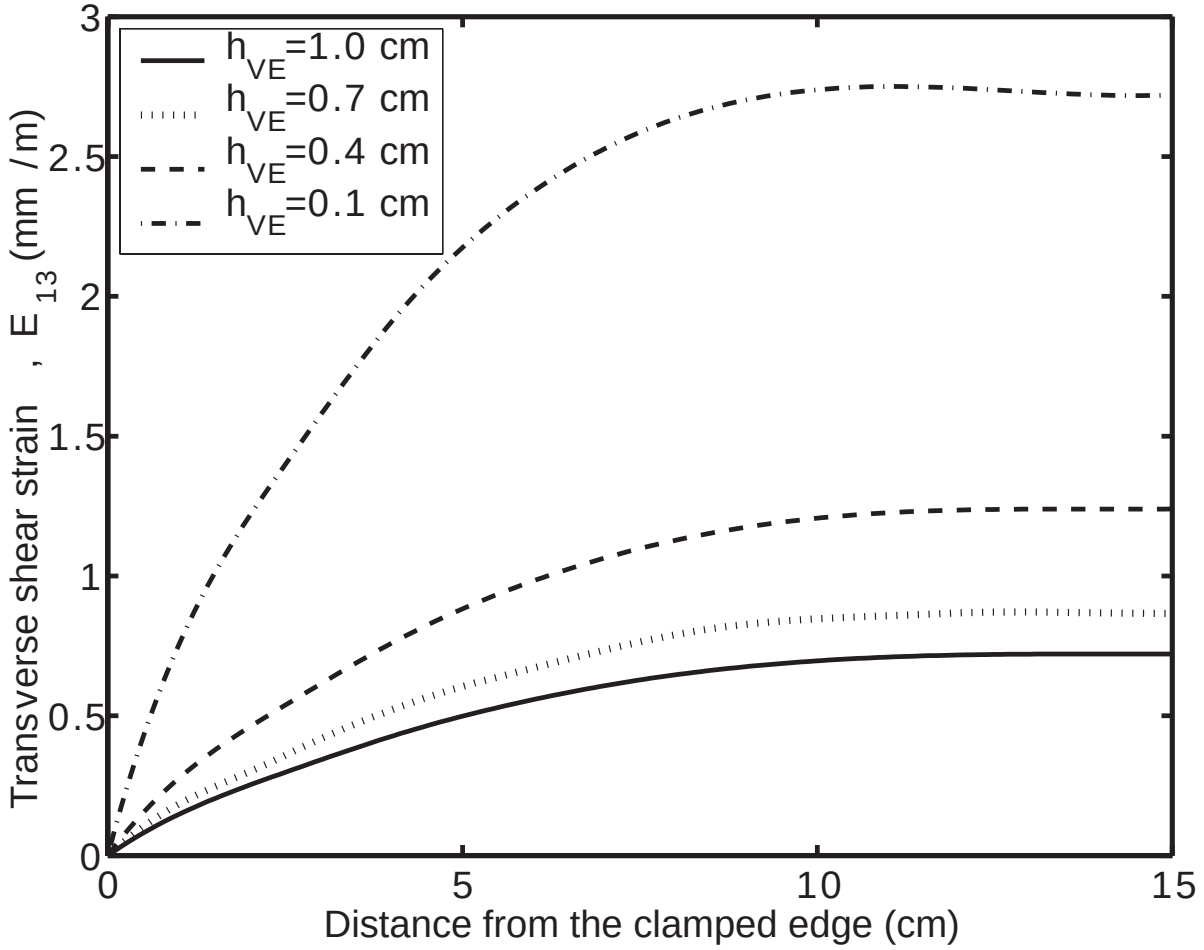

Figure 3.14: For four values of the thickness of the viscoelastic layers, variation of the transverse shear strain, E_{13}, on the midsurface of a viscoelastic layer; shear mode actuators.

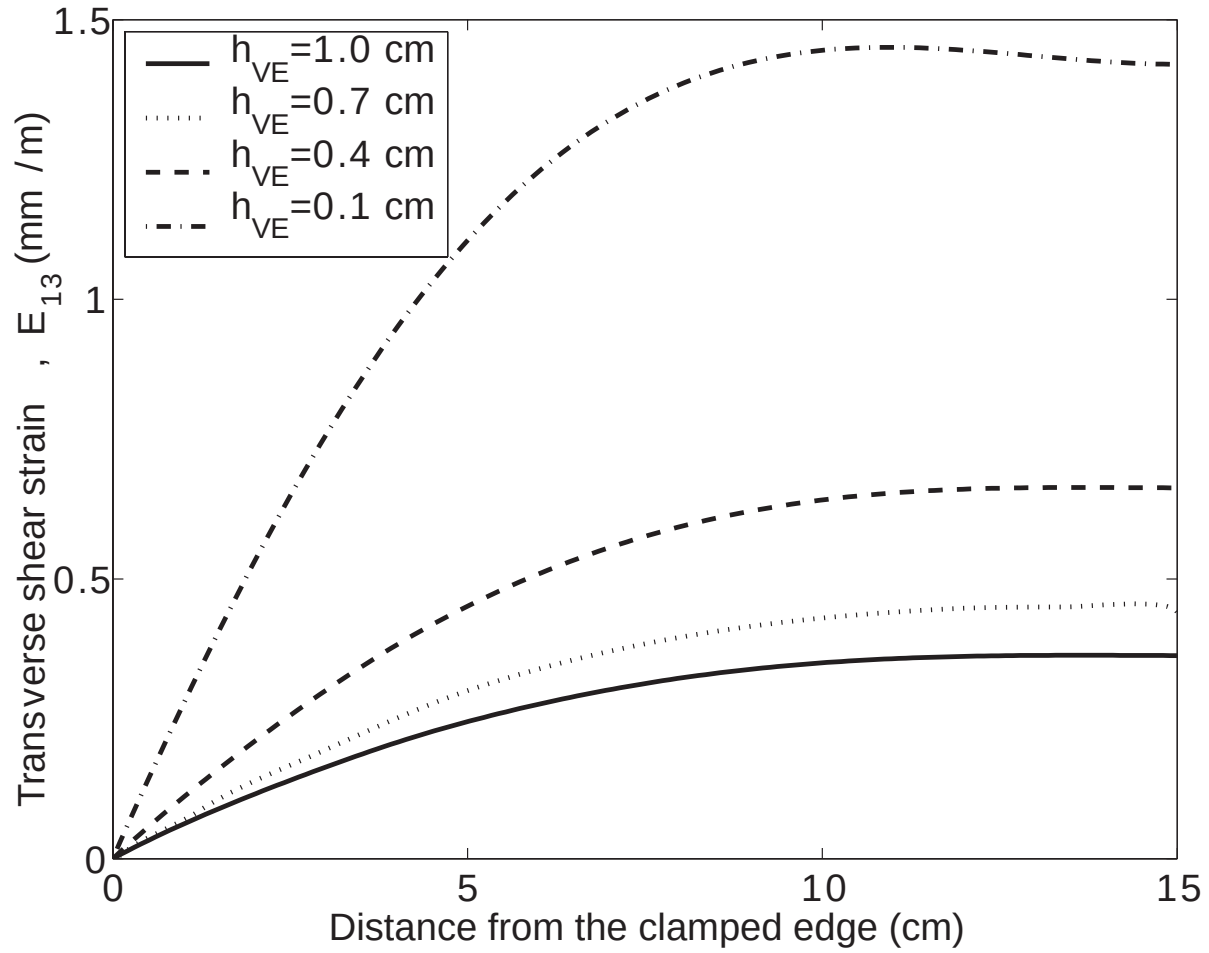

Figure 3.15: For four values of the thickness of the viscoelastic layers, variation of the transverse shear strain, E_{13}, on the midsurface of a viscoelastic layer; extension mode actuators.

energy dissipated per cycle of vibration need not be maximum for h_{VE} = 0.1 cm.

Effect of the thickness of PZT layers

We take h_{VE} = 0.3 cm and study the effect on damping of the thickness of the PZT layers. For the extension mode actuator configuration, the fundamental natural frequency for h_{PZT} = 0.1, 0.2, 0.3, 0.4 and 0.5 cm was found to be 9.479, 9.236, 8.985, 8.734 and 8.482 kHz respectively. Recalling that the thickness of the shear mode PZT actuator is twice that of each of the extension mode actuators, the corresponding natural frequency for the shear mode PZT set-up was found to be 6.220, 6.005, 5.843, 5.718 and 5.655 kHz. As stated earlier, in each case the system was excited by tangential tractions whose frequency equals the natural frequency of the system. The dependence of the three measures of energy dissipation or damping, $\delta^{\ell n}$, I_1 and I_2, upon the thickness of the PZT layer is exhibited in Figs. 3.16, 3.17 and 3.18 for the shear mode and the extension mode actuators. The electric energy input into the PZTs is different in each case. For the shear mode actuator, the logarithmic decrement has the maximum value for $h_{\rm PZT} \simeq 0.85$ cm, but for the extension mode configuration, the maximum value of $\delta^{\ell n}$ occurs for $h_{\rm PZT} > 1$ cm. However, for the same thickness of the PZT layers, the logarithmic decrement is higher for the shear mode configuration than that for the extension mode one. Whereas the index I_1 for the shear mode configuration increases monotonically and quite rapidly with an increase in the thickness of the PZT layer, for the extension mode configuration it attains a maximum value for $h_{\rm PZT} \simeq 0.8$ cm. The thickness of the PZT layer has a minimal influence on I_2 for the extension mode configuration but affects noticeably the value of I_2 for the shear mode configuration. For the shear mode configuration, the maximum value of I_2 occurs for $h_{\rm PZT} \simeq 0.8$ cm.

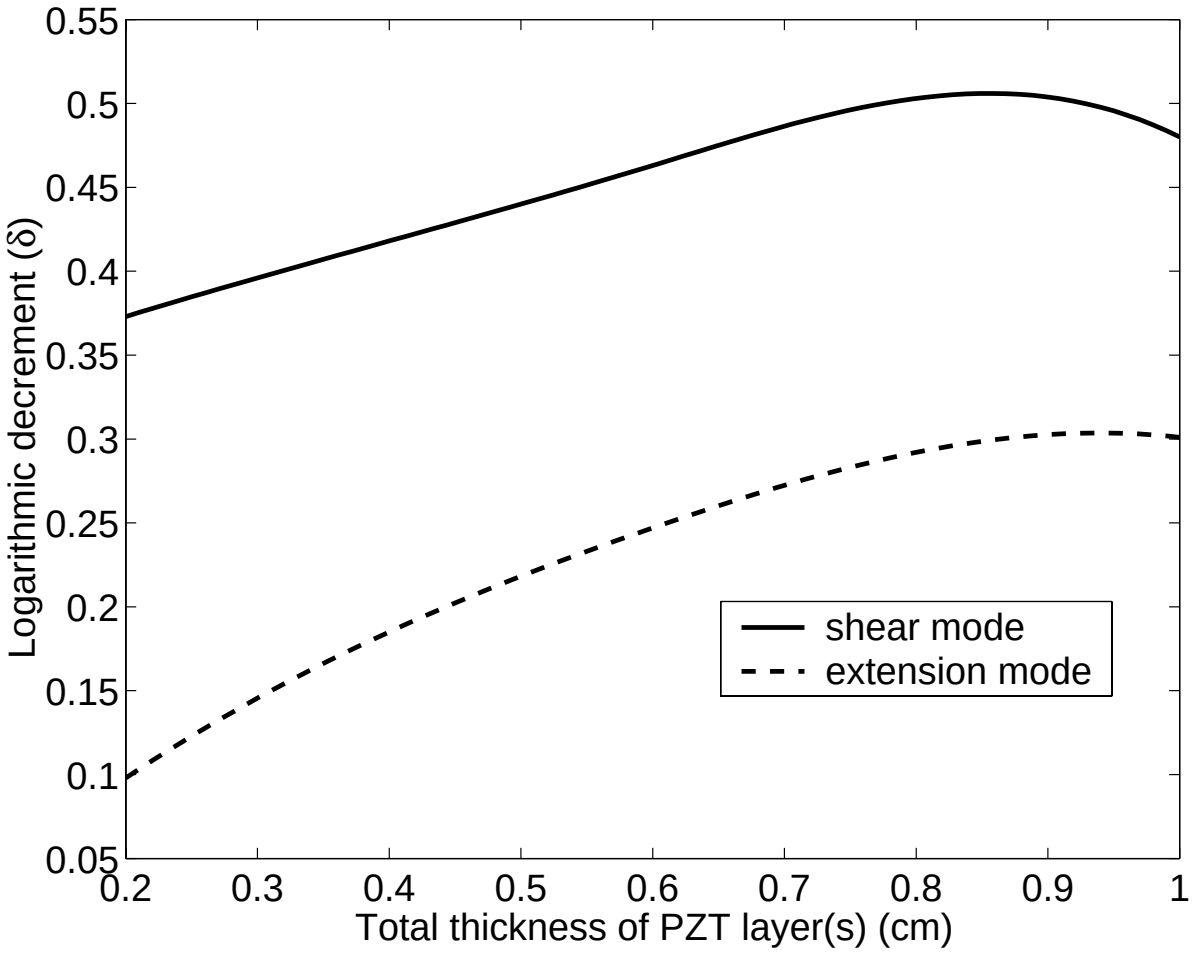

Figure 3.16: Dependence of the measure $\delta^{\ell n}$ of energy dissipation upon the thickness of the PZT layer.

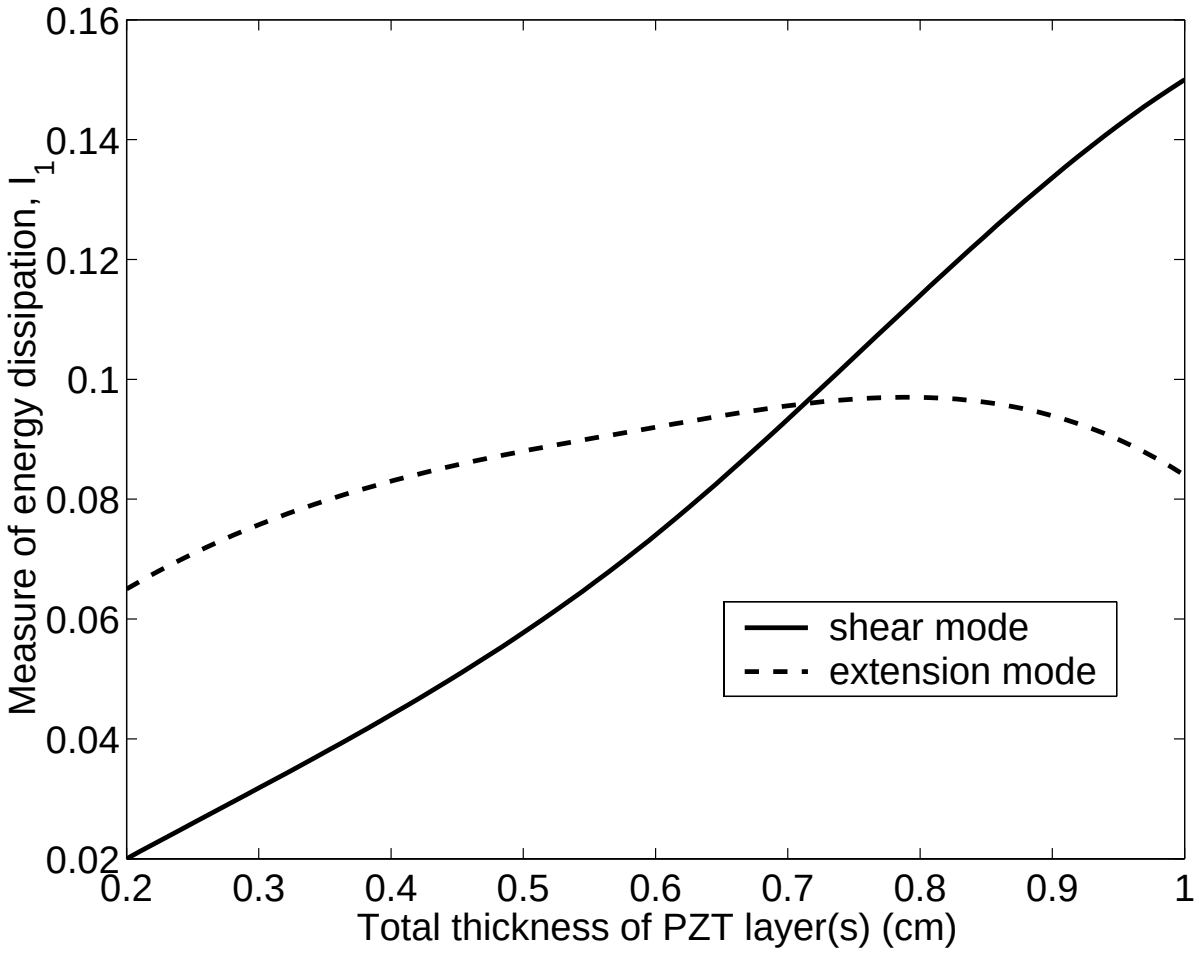

Figure 3.17: Dependence of the measure I_1 of energy dissipation upon the thickness of the PZT layer.

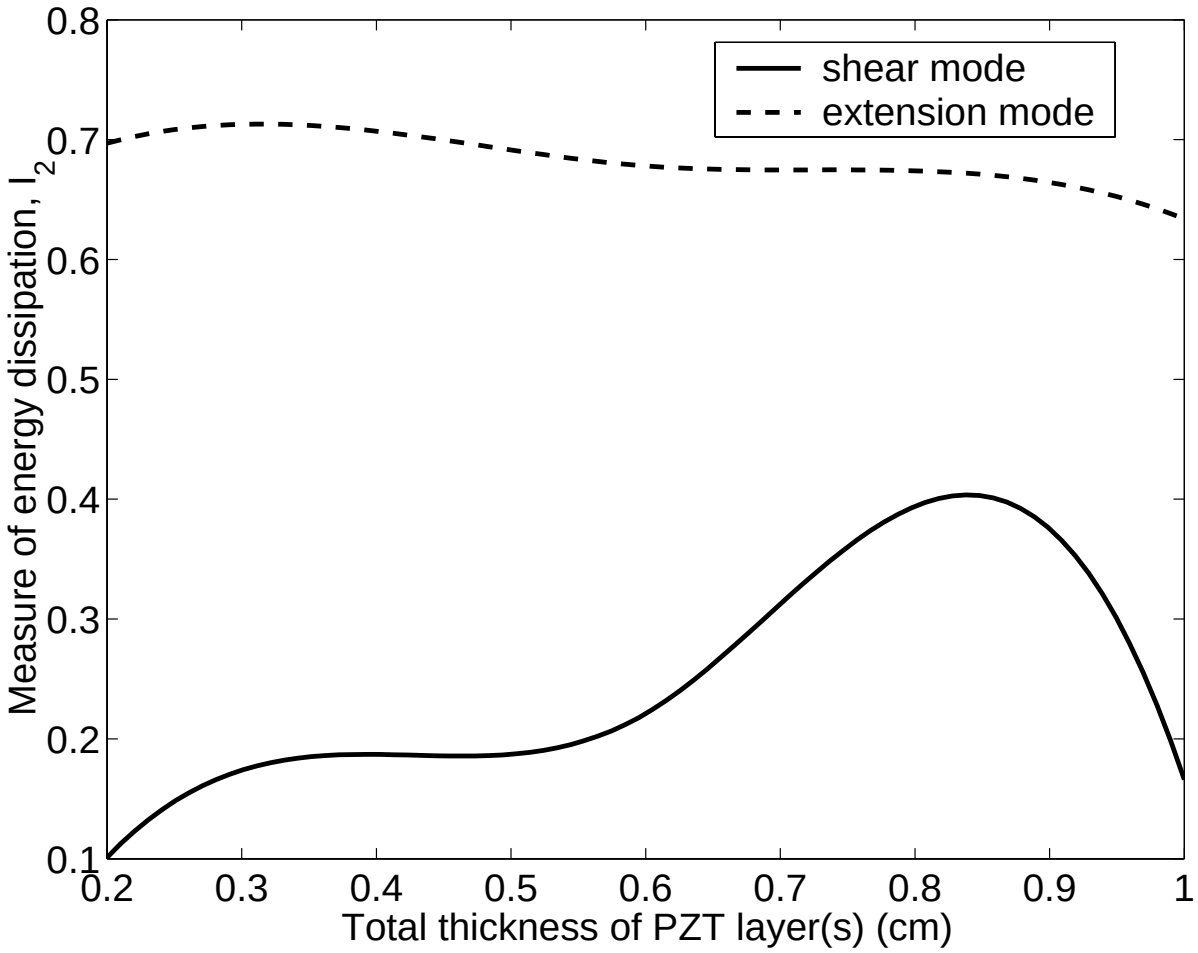

Figure 3.18: Dependence of the measure I_2 of energy dissipation upon the thickness of the PZT layer.

Effect of the aspect ratio of the plate

We now explore if an ACLD treatment works equally well for plates of different aspect ratios (s = length of plate/thickness of plate). We set h_{VE} = 0.3 cm and h_{PZT} = 0.4 cm for the extension mode PZTs and vary the aspect ratio by fixing the thickness of each layer and changing its length. For the shear mode configuration, the number of uniform finite elements used to model the aluminum, the PZT and the viscoelastic layer equaled 9, 1 and 1 in the x_1, x_2 and x_3 directions respectively for s = 3 and 10. For the extension mode configuration, the aluminum layer was divided into 2 elements in the x_3 direction. For s = 20 and 30, the number of elements in the longitudinal direction in each of the layers was increased to 18 and 27 respectively for both set-ups. For the shear and the extension mode configurations, the fundamental frequency for the four aspect ratios is listed in Table 5. For large aspect ratios, the fundamental frequency is inversely proportional to the aspect ratio as predicted by the Kirchhoff plate theory. For the four aspect ratios, the three measures of damping are also listed in Table 5. Values of I_1 which probably are a better indicator of the effect of activating the PZTs on the enhancement in damping suggest that extension mode actuators perform better than the shear mode ones for each of the four aspect ratios.

Table 5. Variation of the three measures of damping with the aspect ratio.

Aspect ratio s	Fundamental frequency (kHz)		Measures of damping					
			δ^{ln}		I_1		I_2	
	Shear mode	Extension mode	Shear mode	Extension mode	Shear mode	Extension mode	Shear mode	Extension mode
3	6.005	9.236	0.418	0.185	0.044	0.083	0.187	0.707
10	1.165	1.257	0.374	0.055	0.082	0.258	0.009	0.155
20	0.503	0.503	0.235	0.022	0.032	0.17	0.014	0.691
30	0.314	0.314	0.153	-	0.017	0.12	0.013	-

Effect of the poling direction of the shear mode PZT

In order to quantify the deterioration in the damping caused by the misorientation of the poling direction $\mathbf{a}$ for the shear mode PZT, we ascertained the effect of changing $\mathbf{a}$ in the x_1-x_3 plane. Let $\mathbf{a}$ make an angle θ^0 counterclockwise from the x_1-axis, i.e., $\mathbf{a} = (\cos\theta, 0, \sin\theta)$. Material properties of the PZT with respect to the global axes are obtained from equations (3.21). For seven values of θ, Table 6 lists the computed fundamental frequencies and the three measures of damping. Whereas the logarithmic damping is unaffected by the change in θ, values of I_1 and I_2 decrease as θ increases. Both I_1 and I_2 drop by about 10% when poling direction is inclined at 15° instead of 0° to the x_1-axis. Thus it is important that the shear mode PZT be poled correctly for optimum performance.

Table 6. For the shear mode PZT, dependence upon the poling direction of the fundamental frequency and the three measures of damping.

Poling angle θ°	Fundamental frequency (kHz)	Measures of damping		
		δ^{ln}	I_1	I_2
0	5.089	0.369	0.128	0.092
15	5.119	0.369	0.099	0.080
30	5.129	0.367	0.053	0.025
45	5.134	0.367	0.008	-0.014
60	5.128	0.368	-0.019	-0.035
75	5.117	0.369	-0.025	-0.051
90	5.111	0.370	-0.019	-0.033

We did not perform a similar study for the extension mode PZT.

Energy of electrical deformations

Figure 3.19 exhibits the time history of the energy, E_{el}, of electric deformations for the shear mode and the extension mode ACLD treatments with $h_{VE} = 1.0$ cm and $h_{\rm PZT} = 1.0$ cm. E_{el} is defined as

$$E_{el} = \int_{\Omega_{\rm PZT}} D_i W_i d\Omega$$

where $\Omega_{\rm PZT}$ is the region occupied by the PZT. Since a uniform electric potential is applied across the major surfaces, $x_3 = \text{const.}$, of the PZTs, only W_3 and D_3 have significant values; computed values of W_1 and W_2 were found to be several orders of magnitude lower than those of W_3. Recall that the time periods of the two configurations are different. Larger values of the energy of electric

deformations for the shear mode PZTs suggest that the potential difference imposed across the major faces of the PZT layers is higher for the shear mode configuration than that for the extension mode configuration. Also, flat portions of the curve for the shear mode PZTs suggest that the prescribed limiting value of the potential difference and hence of the electric field was required. Since the maximum bending stress induced in the shear mode PZT is considerably lower than that in the extension mode PZT, the former is expected to have larger service life.

Simultaneous damping of first two frequencies by using a functionally graded viscoelastic layer

Whereas in Section 3.3.2 we assessed the effect of varying the relaxation time τ on the logarithmic decrement for the fundamental mode of vibration of the structure, here we examine if the first two modes can be damped out simultaneously. The structure was excited as described in Section 3.3.1 and the amplitudes of vibrations of the first two modes were found by using the FFT technique both with and without (i.e. $\chi = 0$) modeling damping caused by the viscoelastic layer. For the undamped structure, the relative amplitude of the first mode of vibration equaled 8 times that of the second mode. These results, summarized in Table 7, suggest that $\tau = 1/\omega_1$ is most effective in damping out the first mode of vibration. However, $\tau = 1/\omega_2$, $1/\omega_3$ or $1/\omega_4$ damps out better the second mode of vibration. For any one of these three values of τ, the first mode of vibration is not damped out quickly.

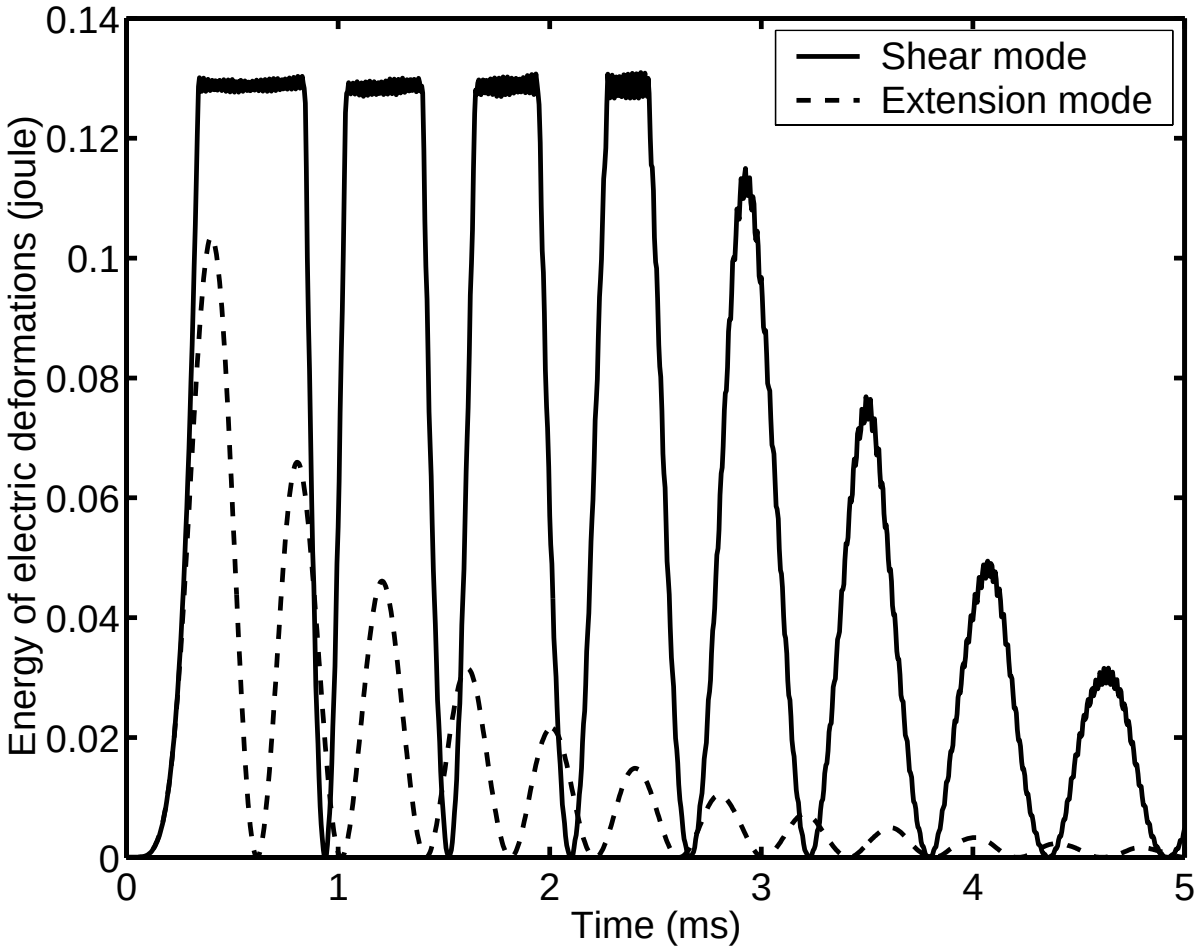

Figure 3.19: Time history of the energy of electric deformations for the shear mode and the extension mode ACLD treatments; $h_{VE} = 1.0\ \mathrm{cm},\ h_{\mathrm{PZT}} = 1.0\ \mathrm{cm}$.

Table 7. Effect of relaxation time on the simultaneous damping of the first two modes.

Relaxation time	Measure I_1 of damping	
τ (μs)	Mode 1	Mode 2
$\tau_1 = 1/\omega_1$	0.6406	0.4818
$\tau_2 = 1/\omega_2$	0.3815	0.8909
$\tau_3 = 1/\omega_3$	0.1644	0.9682
$\tau_4 = 1/\omega_4$	0.1315	0.9682

A possibility for damping out simultaneously the first two modes of vibration is to use a functionally graded viscoelastic layer with material properties varying continuously through the thickness. An approximate way to model a functionally graded layer is to consider it made of several layers of different homogeneous materials. Here, each one of the two viscoelastic layers was divided into four sublayers; when moving in the x_3 direction these are numbered as 1, 2, 3 and 4 for the bottom layer and 4, 3, 2 and 1 for the top layer. For six different assignments of the relaxation times to these sublayers, we list in Table 8 computed values of the measure I_1 of damping for the first two modes of vibration. The entries in the first column and the last row of Table 8 imply that the material of the sublayer 1 had relaxation time τ_1, that of sublayer 2 had relaxation time τ_2 etc. It is clear from these results that the rate of damping of the second mode of vibration is virtually unaffected by the relaxation time assigned to each of the sublayers. Since the amplitude of the first mode of vibration is 8 times that of the second mode, it may be desirable to use homogeneous viscoelastic layers with relaxation time $\tau = 1/\omega_1$. However, the arrangement of the second row of Table 8 doubles the values of I_1 for the second mode of vibration while lowering it only about 15% for the first mode. This may be more effective in damping out quickly the total energy of a structure.

Table 8. Simultaneous damping out of the first two modes of vibration with a functionally graded viscoelastic layer.

Sequence of relaxation times assigned to the 4 sublayers of each viscoelastic layer	Measure I_1 of damping	
	First mode	Second Mode
1-1-1-1	0.6406	0.4818
1-1-2-2	0.5425	0.9682
2-2-1-1	0.5459	0.9727
1-2-2-1	0.5408	0.9682
2-1-1-2	0.5488	0.9727
1-2-3-4	0.3384	0.9682
4-3-2-1	0.3481	0.9636

Effect of Material Nonlinearities in the Constitutive Relation for the PZT

We now investigate the effect of assigning values listed in (3.43) to material parameters ν_4 and ν_{12} in the constitutive relation (3.21) for the PZT. For each one of the ten values of the thickness of the viscoelastic layer listed in Table 1 and for the shear mode and the extension mode configurations, it was found that the value of the index I_1 was nearly the same as that for the case when $\nu_4 = \nu_{12} = 0$. For the shear mode configuration, the index I_1 was computed by considering transverse displacements of a point on the free edge of the PZT layer rather than that of a point on the aluminum layer. Figure 3.20 compares deformed shapes of the portion of the plate near the unclamped edge when ν_4 and ν_{12} are nonzero with those for $\nu_4 = \nu_{12} = 0$. Displacements have been magnified 100 times to clearly show the deformations. It is clear that for the extension mode configuration, the transverse shear strain in the viscoelastic layer is noticeable. The deformed shape for the shear

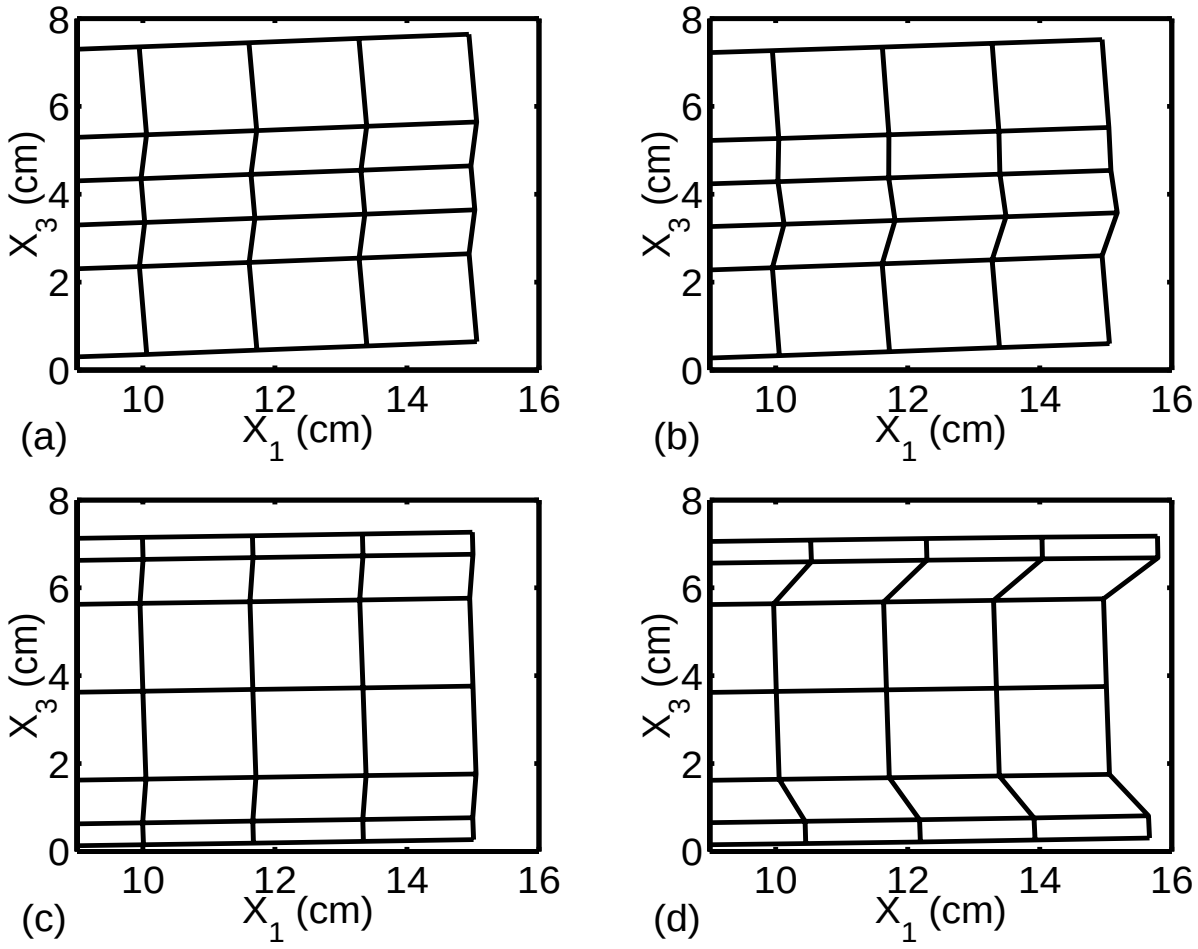

Figure 3.20: Deformed shapes of the laminated hybrid plate; (a) and (b) for the shear mode configuration with zero and nonzero values of ν_4 and ν_{12}, (c) and (d) for the extension mode configuration with zero and nonzero values of ν_4 and ν_{12}.

mode configuration can not be compared with the corresponding deformed shape for the extension mode configuration since the maximum deformations of the viscoelastic layer may not occur at the instants deformed shapes are plotted in Fig. 3.20.

3.3.3 Remarks

One can improve the agreement between experimental and computed results by incorporating more terms involving different relaxation times on the right-hand side of the constitutive relation (3.8) for the viscoelastic layer. The consideration of each additional relaxation time will add an equation like (3.20) and thus increase the computational effort required to analyze the problem. One can economize on the computational effort by integrating equation (3.20) only at the centroid of an element thereby tacitly assuming that $\eta_{\alpha\beta}$ is uniform over the element. This approximation is quite reasonable for a fine mesh. This generalization, though straight forward, has not been implemented in the code yet. Another extension of the work is to incorporate the effect of heat produced by electric and viscous dissipation on the temperature rise and the dependence of material moduli upon the temperature. These effects will be reported in a future study.

3.4 Conclusions

We have compared the performance of two active constrained layer damping treatments (ACLD) in a thick laminated plate comprised of layers made of a piezoceramic (PZT) material, aluminum and a viscoelastic material. Effects of geometric nonlinearities and the dependence of stresses and electric displacements upon squares of the electric field are incorporated into the analysis of the problem. In one configuration, the PZT layer is at the center, and it's transverse shear deformations

are predominant. In the other configuration, the PZT layers are at the outer surfaces and their extensional deformations are significantly more than their transverse shear deformations. Three-dimensional transient deformations of the composite system are analyzed in the time domain by the finite element method.

For each value of the thickness of the viscoelastic layer, the measure I_1 of energy dissipation for the shear mode PZT configuration is larger than that for the extension mode PZT configuration. It implies that the shear mode PZTs are more effective in damping out vibrations of the hybrid plate. The energy of electric deformations of the shear mode PZT configuration is more than that of the extension mode configuration.

The maximum transverse shear strain induced in the viscoelastic layer increases with a decrease in it's thickness. The optimum thickness of the viscoelastic layers for maximum total energy dissipation is the same for each set-up. The thickness of the PZT layer which results in the maximum value of the index I_1 of energy dissipation is the same for the two set-ups. Both arrangements result in the largest value of I_1 for a plate of aspect ratio 10. When each viscoelastic layer was divided into four sublayers and values of the relaxation moduli of the sublayers were changed between 0.1 and 0.4 times their instantaneous values, the value of the logarithmic decrement was essentially unaffected. With the objective of simultaneously damping out quickly the first two modes of vibration, each of these four sublayers was assigned a relaxation time equal to the reciprocal of the first four frequencies. These numerical experiments reveal that subdividing each viscoelastic layer into two sublayers and assigning relaxation times equal to the reciprocal of the first two frequencies to these sublayers will damp out rapidly the first two modes of vibration.

Chapter 4

Buckling of a Sandwich Plate Containing a Soft Core

4.1 Numerical Solution and Discussion of Results

We study three dimensional transient finite deformations of a box type plate. The top and the bottom layers and the layers on the left and the right sides of the structure are made of graphite-epoxy. These layers enclose a soft core. The material of each layer is modeled as orthotropic and neoHookean with the second Piola-Kirchhoff stress tensor related linearly to the Green-St. Venant strain tensor. Thus only geometric nonlinearities are accounted for. Each layer is assumed to be perfectly bonded to its adjoining layer; displacements and surface tractions at points on the common interface are assumed to be continuous across the interface.

The problem is solved by the finite element method as described in Chapters 2 and 3. The goal is to ascertain the difference in the vertical displacements of points on the top and the bottom layers of the plate as it buckles. The initial shape of the midsurface of the plate was taken to be half

sinusoidal both in the X_1- and the X_2-directions with amplitude equal to 1% of plate's thickness. The plate is assumed to have buckled when the transverse displacement (i.e. the displacement in the X_3-direction) of the centroid of the bottom-most surface (point A in Fig 4.1) equals the plate thickness. This buckling criterion differs from that adopted in Chapter 2 because the aspect ratios (i.e. length of the plate/thickness of the plate) of plates considered in this Chapter are small. In other words, plates studied are very thick and the plate is likely to be very severely deformed when the present buckling criterion is satisfied.

Due to the symmetry of the problem about the X_1 and X_2 planes passing through the plate's centriod, deformations of only a quarter of the structure lying in the first quadrant are analyzed. The top and the bottom graphite-epoxy layers are divided into $1.5625 \times 1.25 \times 0.3$ cm 8-noded brick elements, and the element size in the soft core equals $1.5625 \times 1.25 \times 0.35$ cm.

The values of material constants for the graphite-epoxy plate and soft core are listed below.

Graphite-epoxy:

$$\rho_C = 2,700\,\mathrm{kg/m}^3, \tag{4.1}$$

$$\mathbf{C_C} = \begin{bmatrix} 157.8 & 5.64 & 5.64 & 0 & 0 & 0 \\ 5.64 & 15.51 & 7.21 & 0 & 0 & 0 \\ 5.64 & 7.21 & 15.51 & 0 & 0 & 0 \\ 0 & 0 & 0 & 3.2 & 0 & 0 \\ 0 & 0 & 0 & 0 & 4.4 & 0 \\ 0 & 0 & 0 & 0 & 0 & 4.4 \end{bmatrix} \mathrm{GPa}$$

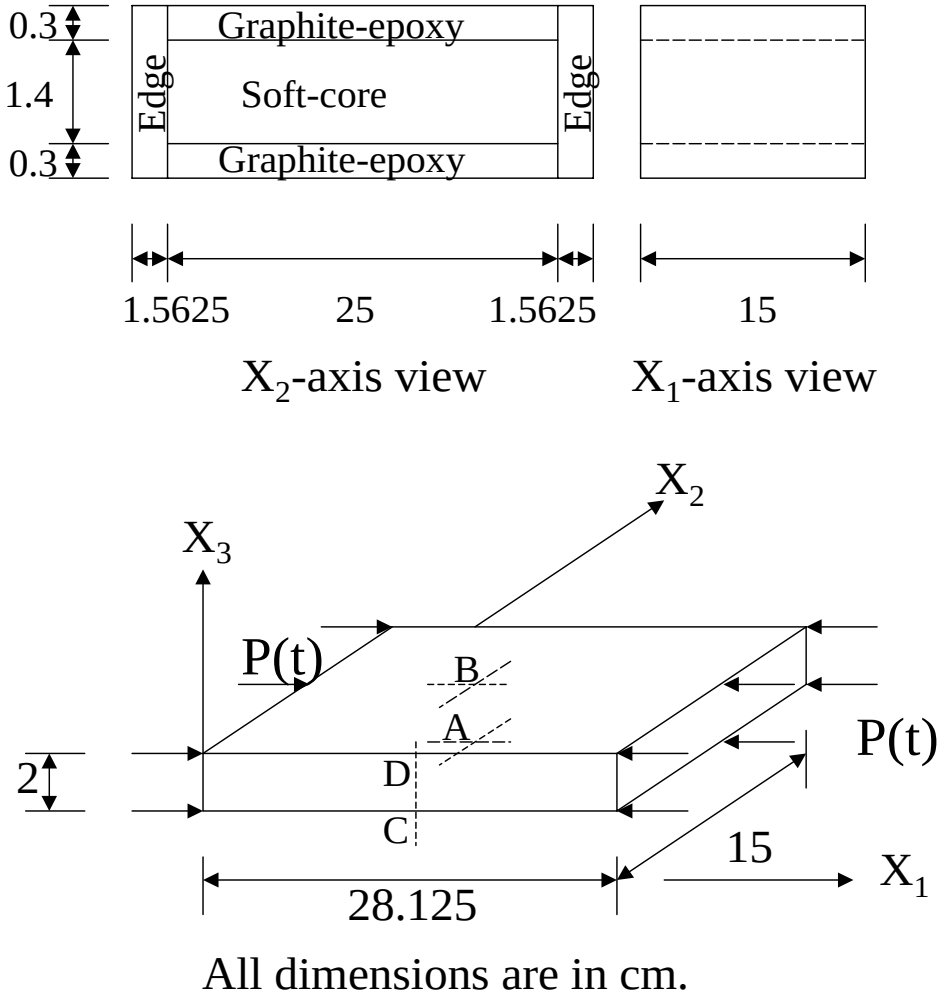

Figure 4.1: Schematic sketch of the problem studied.

Soft core:

$$\rho_S = \frac{\rho_C}{\beta}, \mathbf{C_S} = \frac{\mathbf{C_C}}{\beta} \tag{4.2}$$

Material of the edges:

$$\rho_E = \alpha\rho_C, \mathbf{C_E} = \alpha\mathbf{C_C} \tag{4.3}$$

4.1.1 Determination of edge stiffness to evenly transfer the axial load

Without the edge layers, the buckling load for the $25cm \times 15cm \times 2cm$ homogeneous graphite-epoxy plate (i.e. $\beta = 1$) was found to be 147.6 MN/m. With the edges added and $\beta = 1$, the computed buckling load for different values of α is listed below in Table 1. These values indicate that for $\alpha = 50$, the buckling load of the plate with the graphite-epoxy edge layers equals that of the homogeneous graphite-epoxy plate. Henceforth, we take $\alpha = 50$. The time histories of the transverse displacement of the centroid of the bottom-most surface of the plate with and without the edge layers are plotted in Fig. 4.2.

Table 1. Buckling load for different values of α.

α	1	2	3	4	5	10	20	30	40	50	100
Buckling load (MN/m)	119	128	131	133	134	137	140	142	143	144	149

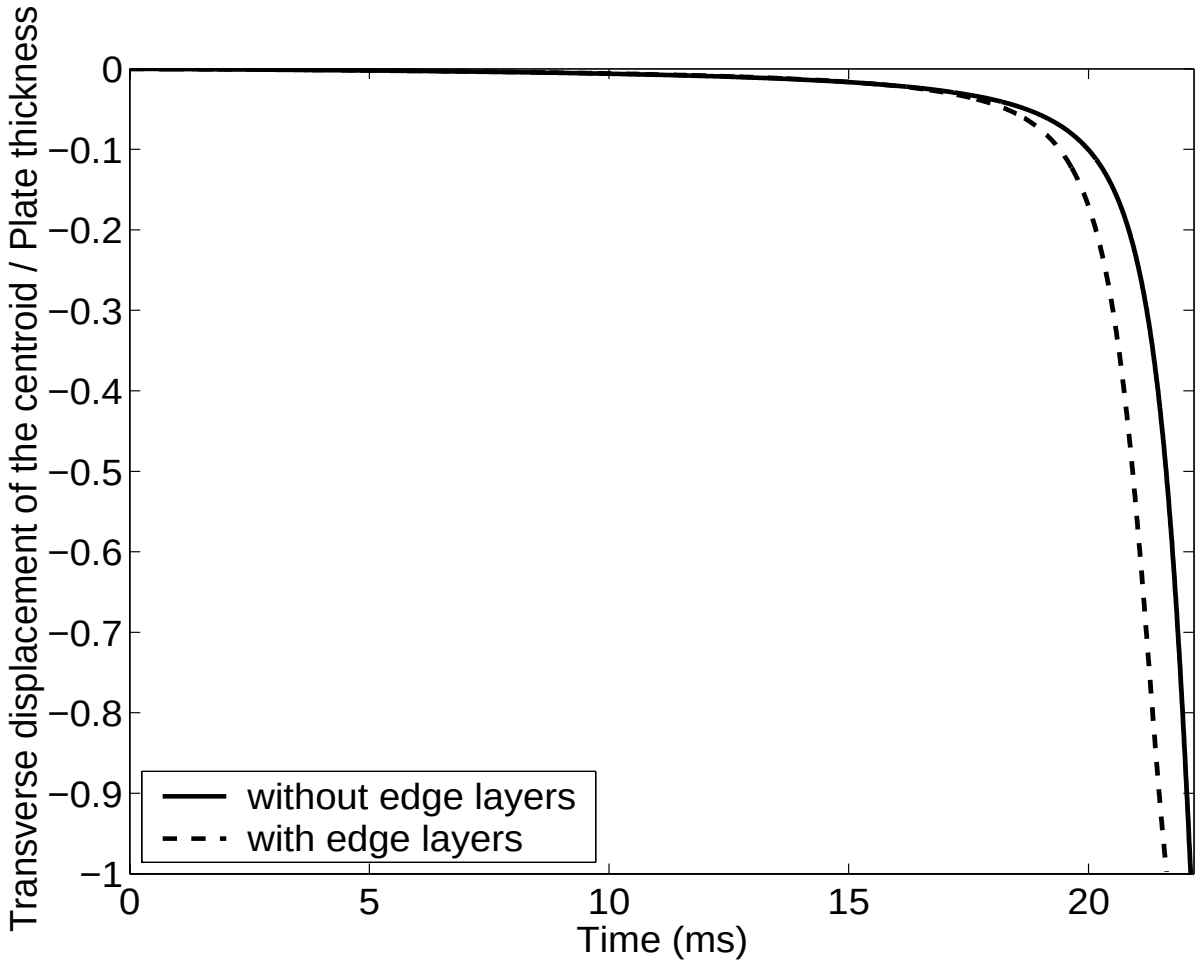

Figure 4.2: The time histories of the transverse displacement of the centroid of the bottom-most surface of the plate with and without edge layers.

4.1.2 Uncoupling of deformations of the three layers

In order to delineate the difference in the transverse displacement of the centroids of the top and the bottom surfaces, we define

$$I_S = \frac{u_3^B - u_3^D}{u_3^A - u_3^C} \tag{4.4}$$

where points A, B, C, D are depicted in Fig. 4.1. Points A and B are respectively the centroids of the bottom and the top surfaces, and points C and D are midpoints of the front edges of the bottom and the top surfaces. I_S will equal 1 if the vertical displacement of point D relative to that of point B equals the vertical displacement of point C relative to that of point A. It will imply that vertical displacements of points A and B are nearly synchronous. I_S will equal zero when $u_3^B = u_3^D$ but $u_3^A \neq u_3^C$. This will be so if the top layer deformed in mode (1,0) and the bottom layer in mode (1,1). Recall that $u_3^C = 0$ because point C is restrained from moving in the vertical direction. Since $u_3^A \neq 0$ for $p \neq 0$, I_S is well defined. When $u_3^A = -3$ mm, the dependence of the vertical displacement of points B and D upon β and the corresponding values of I_S are listed in Table 2.

Table 2. Values of u_3^B, u_3^D and I_S for different β values when $u_3^A = -3$ mm.

β	u_3^B(mm)	u_3^D(mm)	I_S
1	-2.969	-0.0504	0.973
2	-2.965	-0.0521	0.971
5	-2.980	-0.0771	0.968
10	-3.003	-0.1226	0.96
20	-3.004	-0.1587	0.948
50	-3.008	-0.1931	0.938
100	-3.009	-0.215	0.931
200	-3.014	-0.2497	0.921
500	-3.006	-0.3447	0.887
1,000	-2.983	-0.4689	0.838
2,000	-2.953	-0.6758	0.759
5,000	-2.902	-1.108	0.598
10,000	-2.904	-1.503	0.467
20,000	-2.911	-1.814	0.366
50,000	-2.905	-2.053	0.284
100,000	-2.906	-2.149	0.252
200,000	-2.907	-2.199	0.236
500,000	-2.907	-2.231	0.225

Note that u_3^B is nearly equal to u_3^A for $1 \leq \beta \leq 5\times10^5$ but values of u_3^D decrease from virtually zero to -2.231 mm implying that the top layer deforms in mode (1,0) for lager values of β and in mode (1,1) for small values of β whereas the bottom layer always deforms in mode (1,1). Deformed shapes of the top and the bottom layers for $\beta = 1$ and 5×10^5 are evinced in Figs. 4.3 and 4.5; for comparison purposes, we have also plotted in Fig. 4.4 these shapes for $\beta = 500$. Views from the

X_2-axis of the deformed shape for β=1, 500, and 500,000 are evinced in Figs. 4.6-8. We can see that a vertical line in the edge remains straight for different values of β. Since the elastic moduli of the intermediate layer are inversely proportional to β, for $\beta = 5 \times 10^5$ the intermediate layer is very soft and deformations of the top and the bottom layers become uncoupled. In this sense, I_S is a measure of the coupling of the deformations of the two layers. Values of I_S for different values of β are plotted in Fig. 4.9. We can see that I_S drops rapidly when β is increased from 5×10^2 to 5×10^5.

Time histories of u_3^A, u_3^B and u_3^D are plotted in Figs. 4.10-12 for β=1, 500, and 500,000. These show that u_3^A and u_3^B are always close to each other and equal -2.7 mm; however u_3^D decreases from -0.05 mm to -2.23 mm as β increases from 0 to 5×10^5.

Time histories of I_S are plotted in Fig. 4.13 for β=1, 500, and 500,000. An increase in β increases the rate of drop of I_S.

Time histories of the axial loads taken by the top, the bottom, and the intermediate layers for β=1, 500, and 500,000 are plotted in Figs. 4.14-16. As expected, the intermediate layer takes very little load for large values of β. The loads taken up by the top and the bottom layers are nearly equal even when the two deform in different modes.

4.1.3 Effects of the core thickness

For $\beta = 5 \times 10^5$, vertical displacements of points B and D for different thicknesses of the intermediate layer are listed in Table 3.

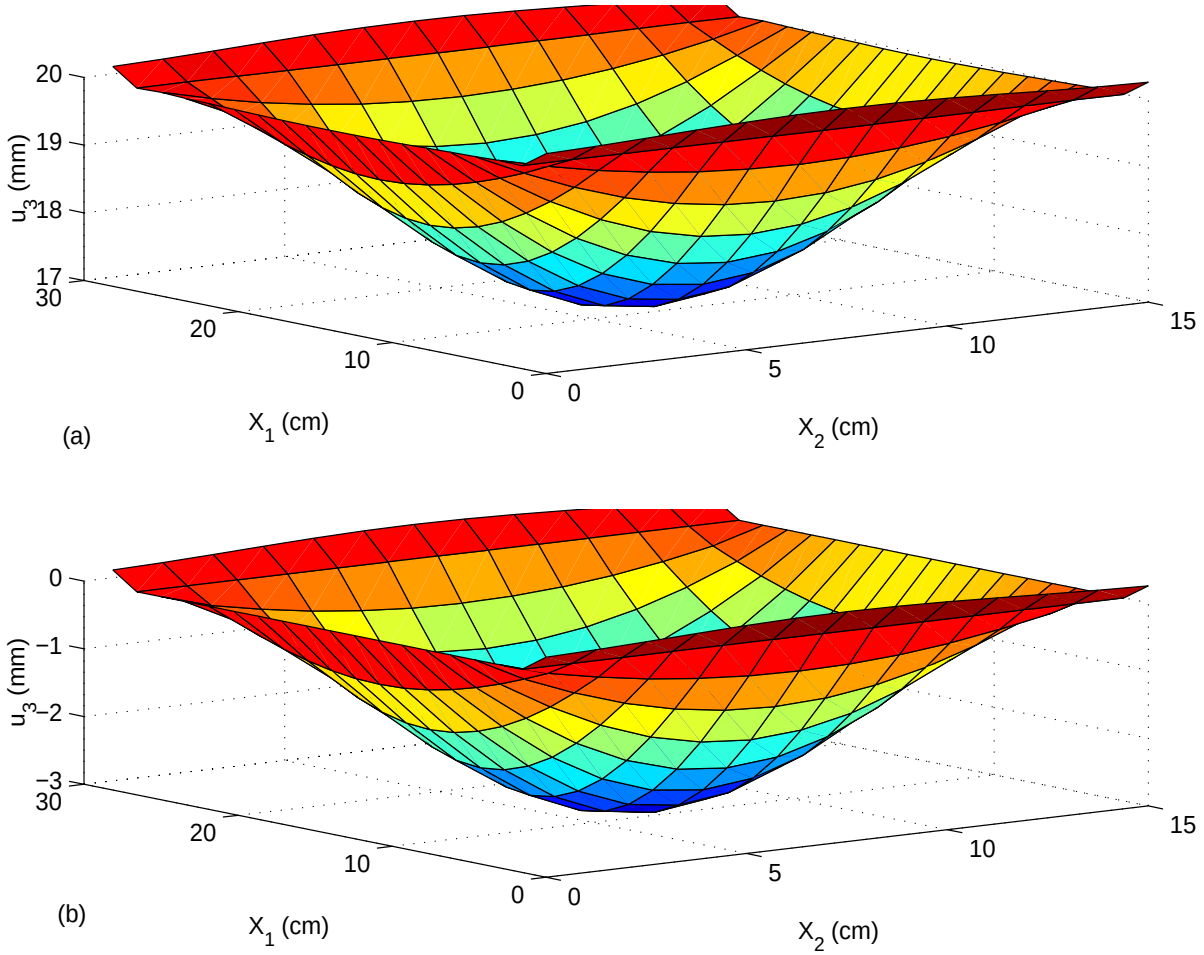

Figure 4.3: Deformed shapes of (a) the top layer, and (b) the bottom layer at the instant the transverse displacement of the centroid of the bottom surface equals -3 mm for $\alpha = 50, \beta = 1$.

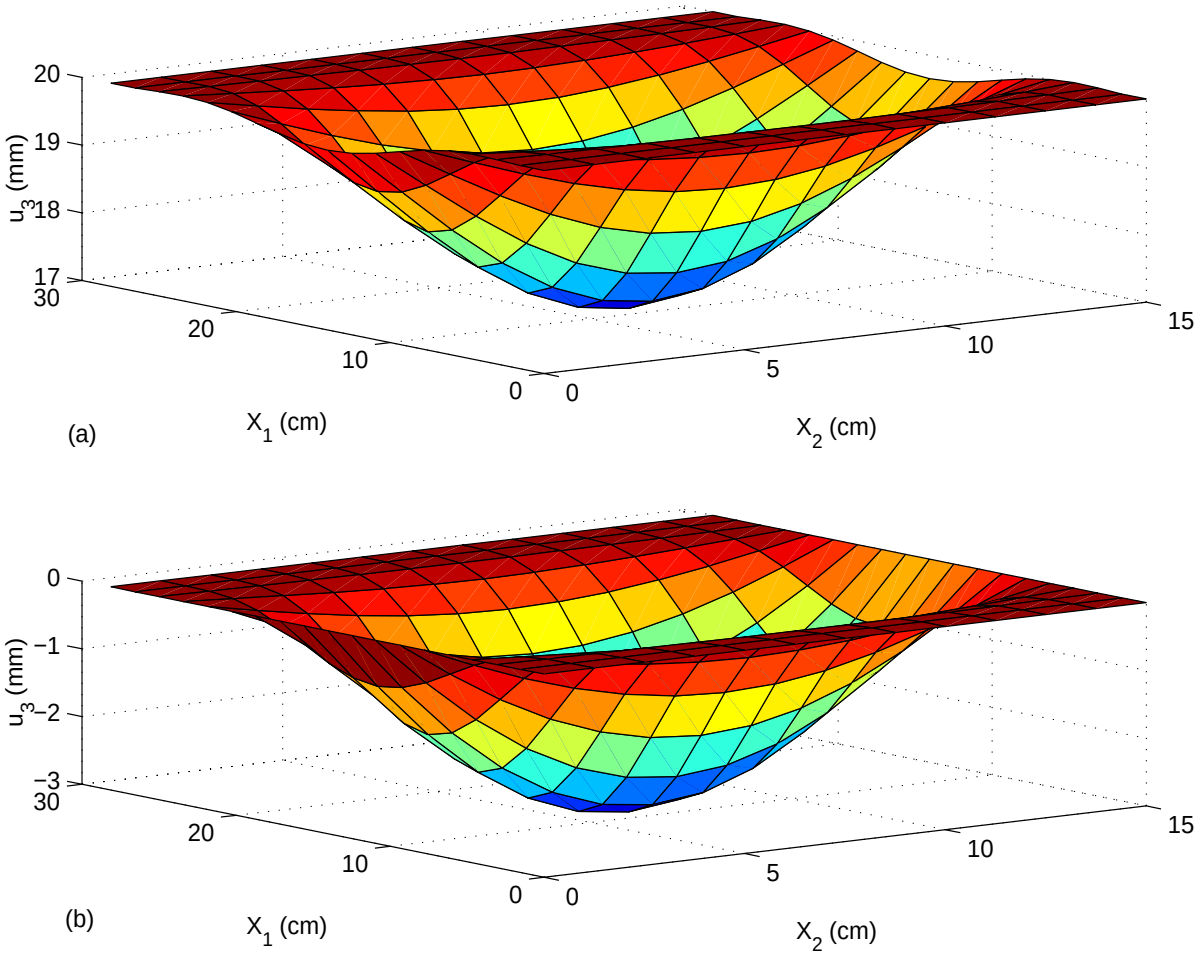

Figure 4.4: Deformed shapes of (a) the top layer, and (b) the bottom layer at the instant the transverse displacement of the centroid of the bottom surface equals -3 mm for $\alpha = 50, \beta = 500$.

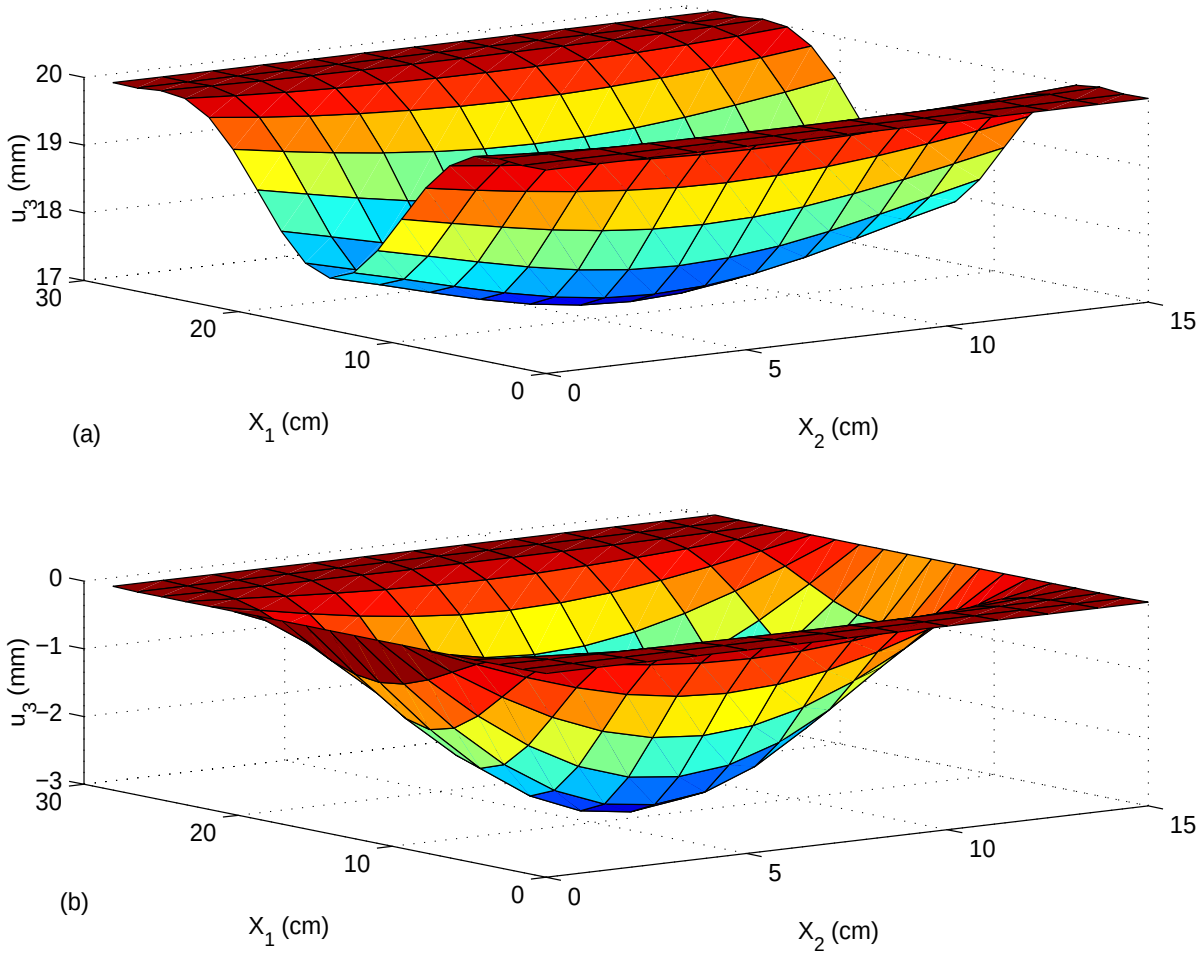

Figure 4.5: Deformed shapes of (a) the top layer, and (b) the bottom layer at the instant the transverse displacement of the centroid of the bottom surface equals -3 mm for $\alpha = 50, \beta = 500,000$.

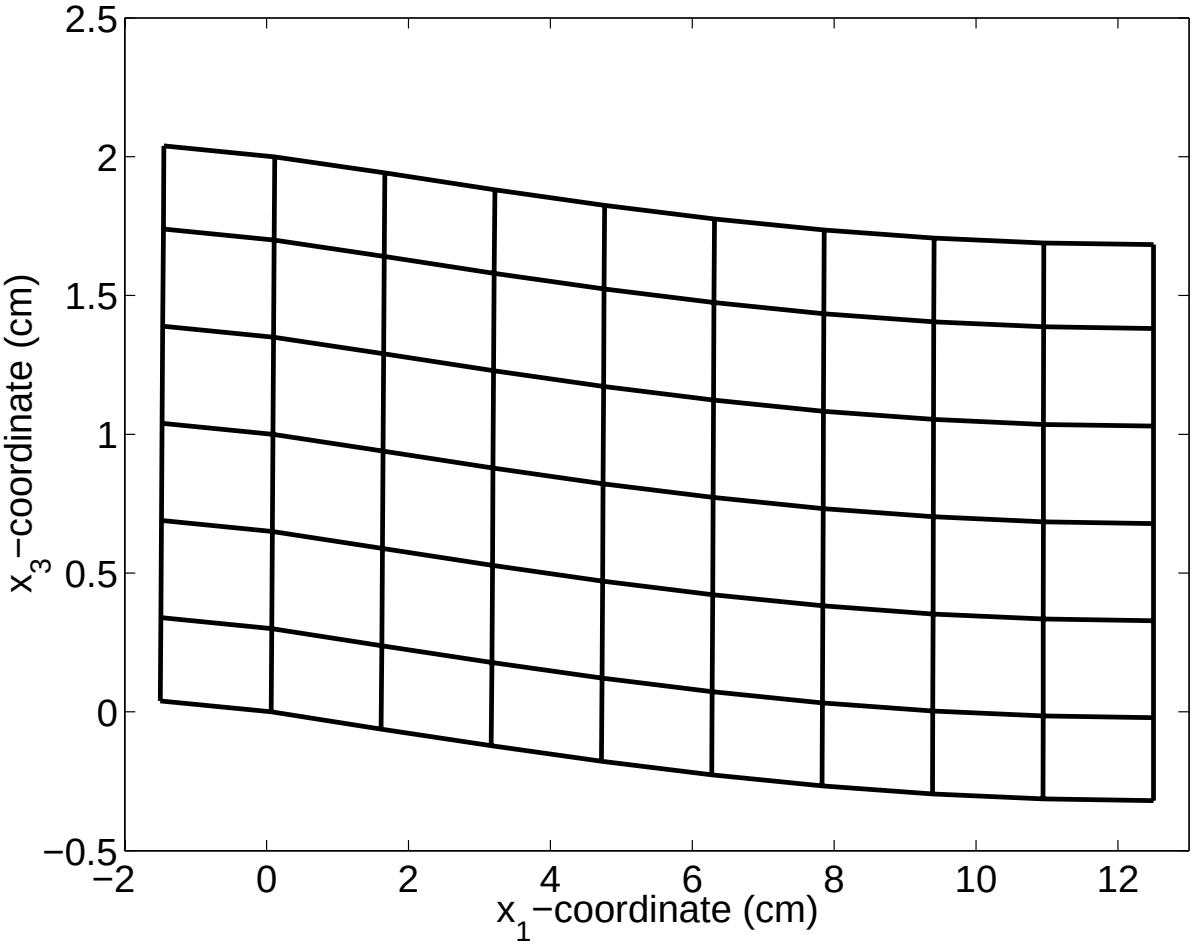

Figure 4.6: View from the X_2-axis of the deformed shape at the instant the transverse displacement of the centroid of the bottom surface equals -3 mm for $\alpha = 50, \beta = 1$.

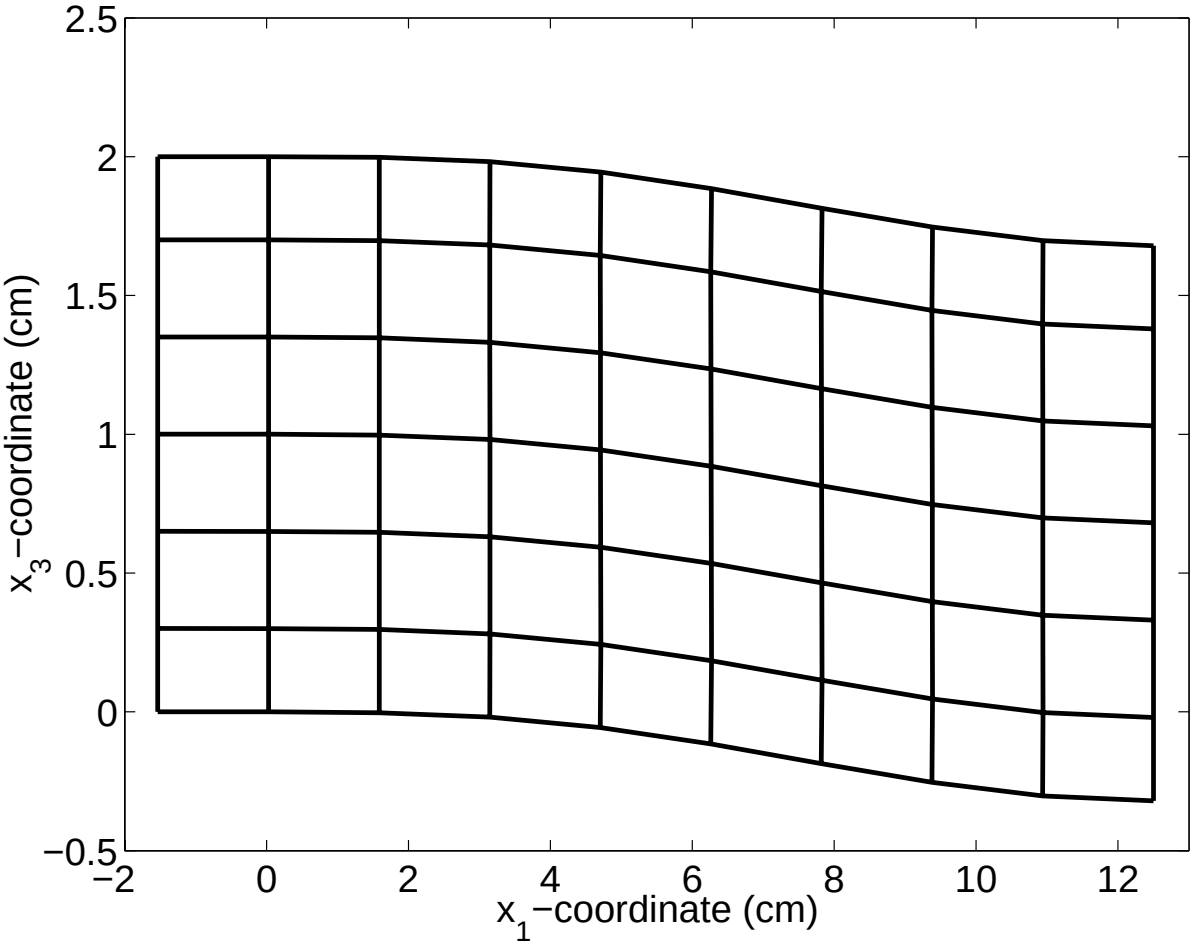

Figure 4.7: View from the X_2-axis of the deformed shape at the instant the transverse displacement of the centroid of the bottom surface equals -3 mm for $\alpha = 50, \beta = 500$.

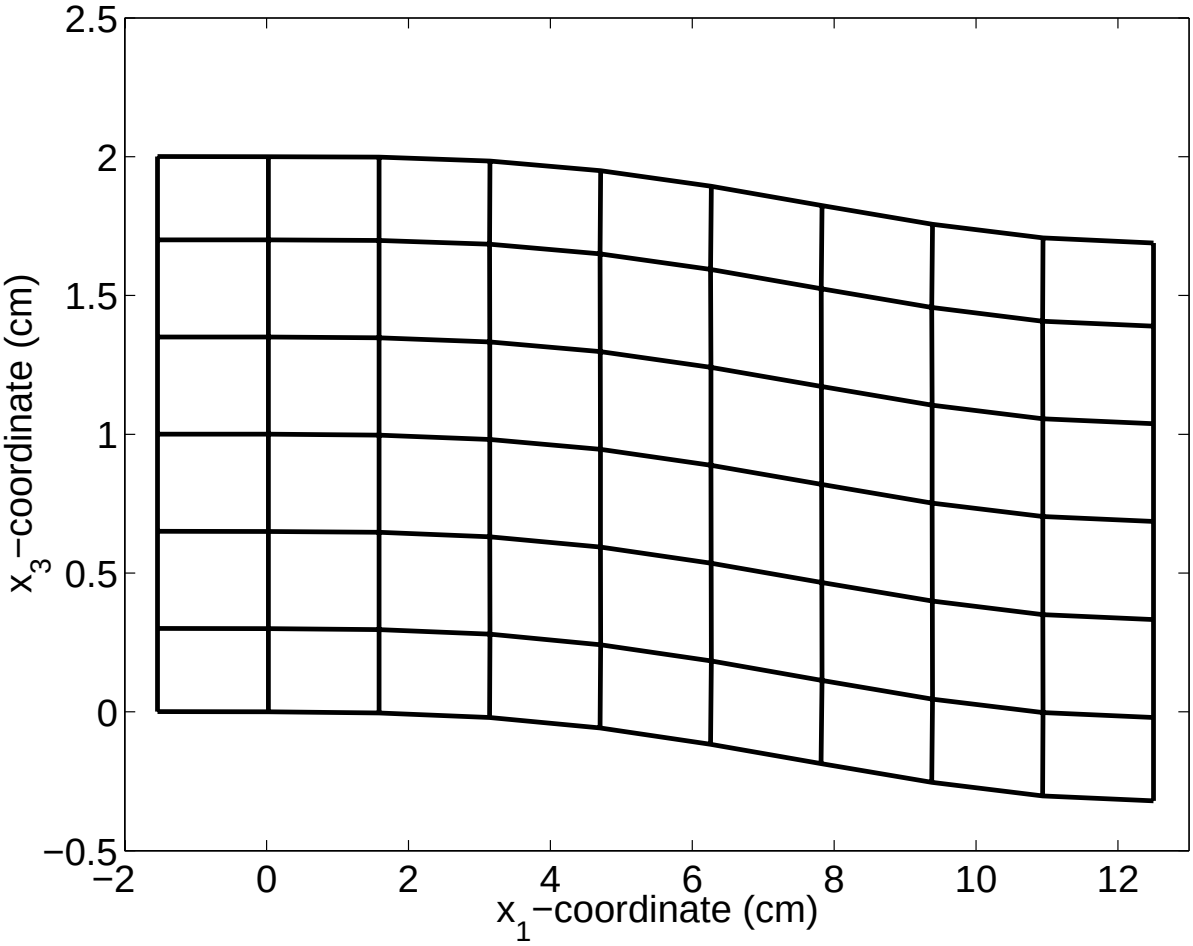

Figure 4.8: View from the X_2-axis of the deformed shape at the instant the transverse displacement of the centroid of the bottom surface equals -3 mm for $\alpha = 50, \beta = 500,000$.

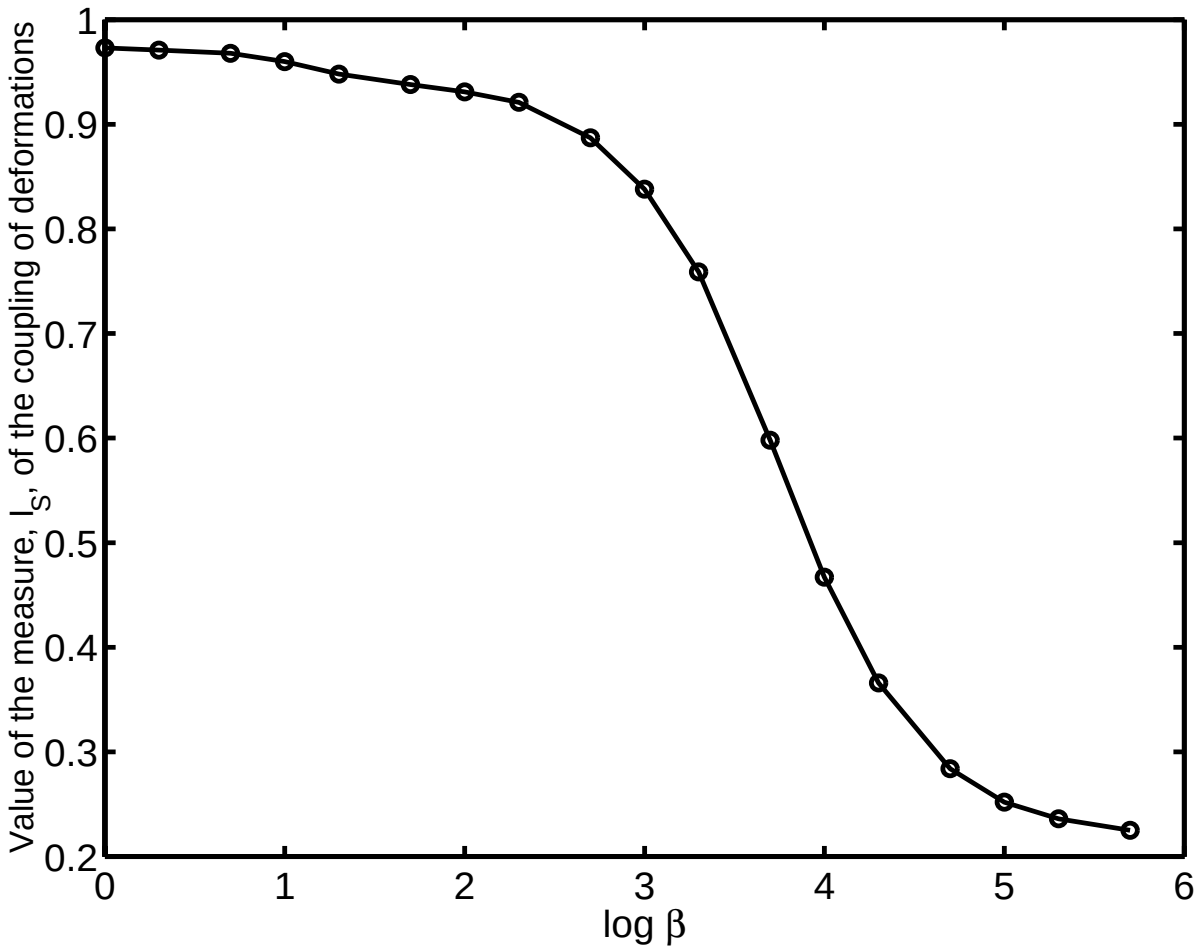

Figure 4.9: Variation of I_S with the ratio β of the elastic moduli of the top or the bottom graphite-epoxy layer and the soft core.

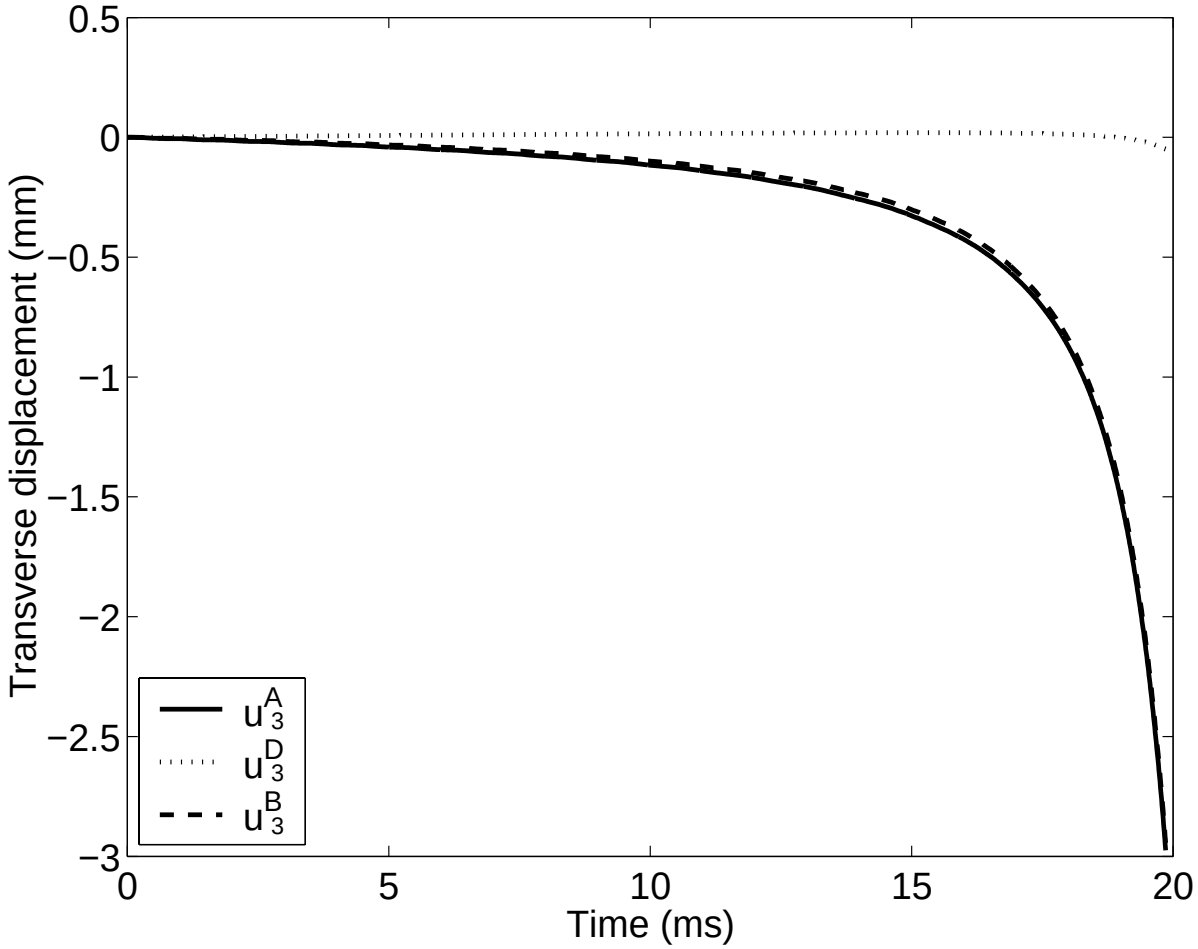

Figure 4.10: Time histories of u_3^A, u_3^B and u_3^D for $\beta = 1$.

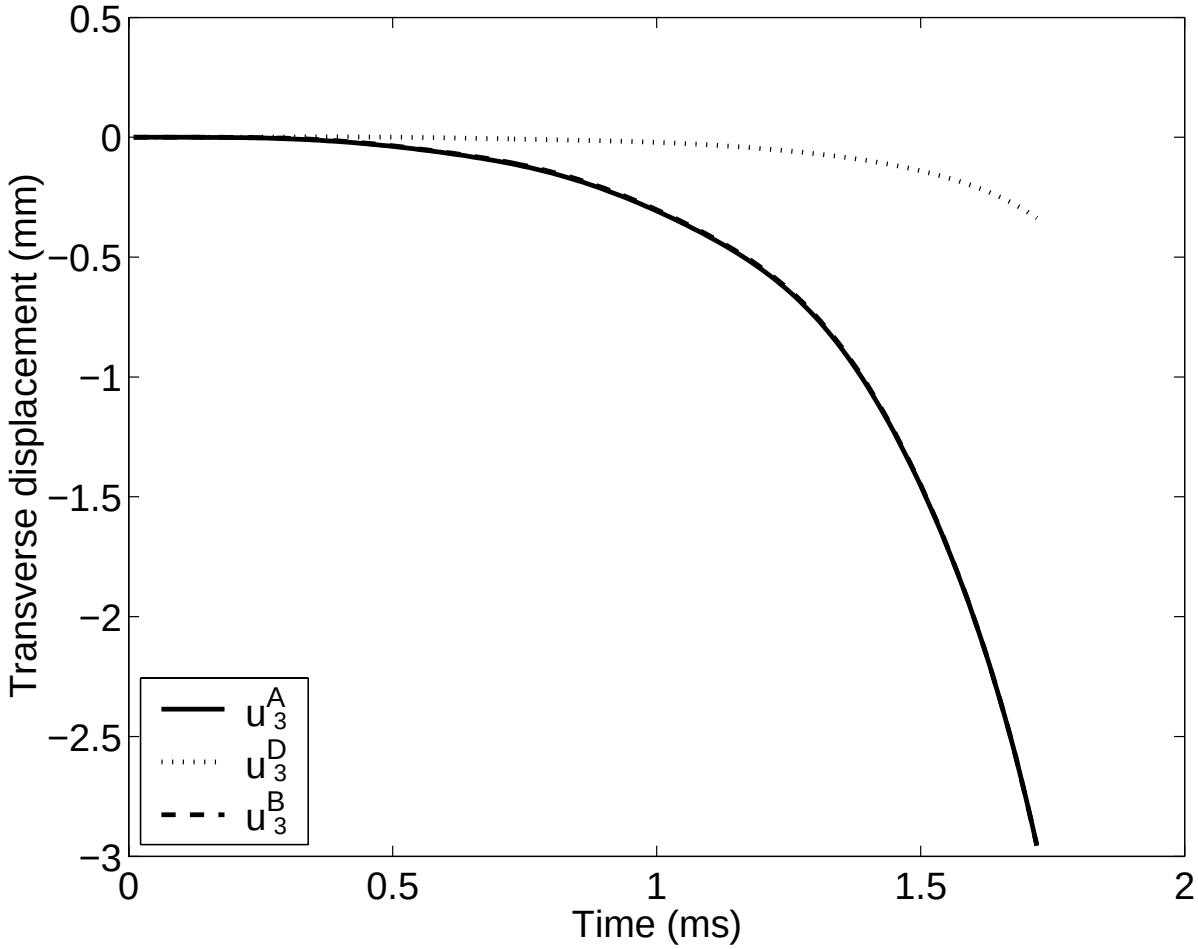

Figure 4.11: Time histories of u_3^A, u_3^B and u_3^D for $\beta = 500$.

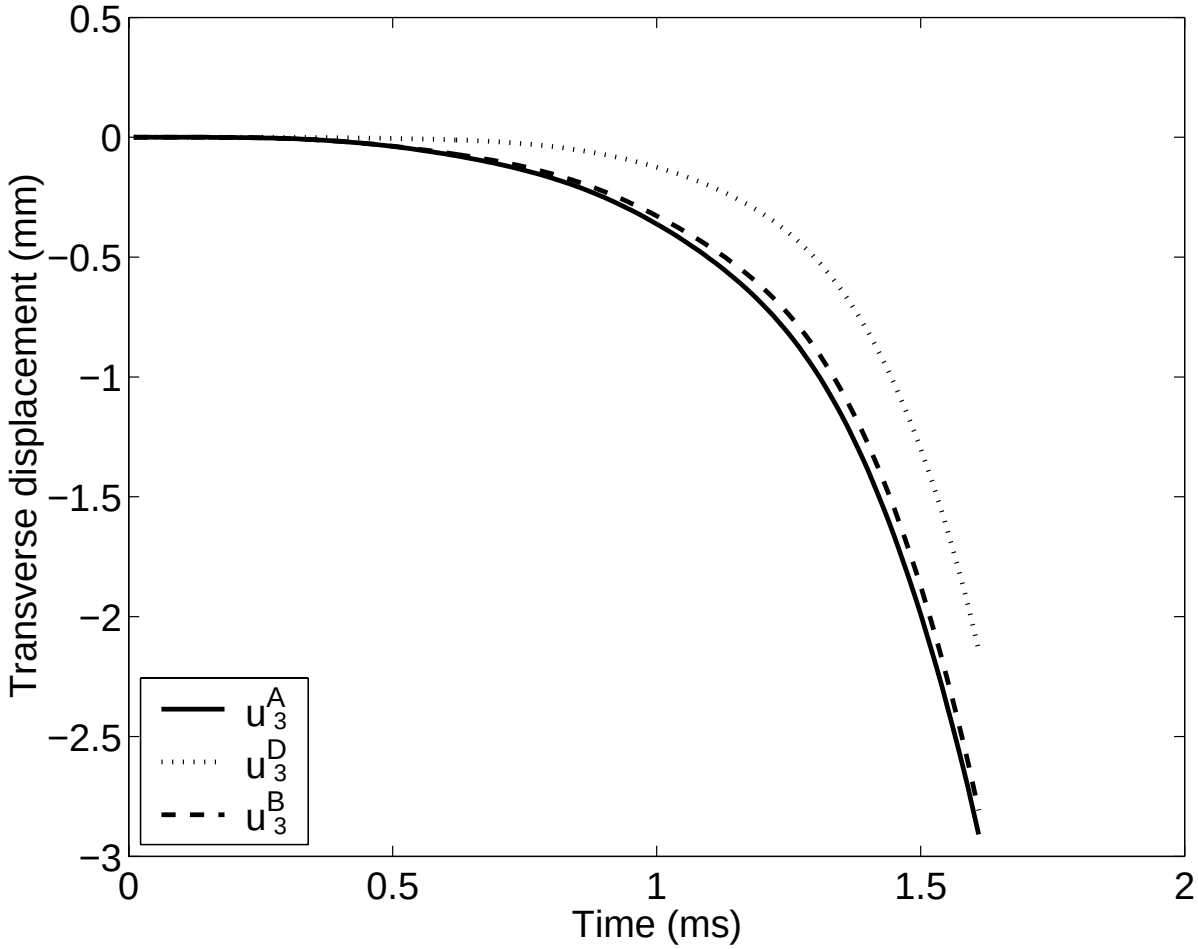

Figure 4.12: Time histories of u_3^A, u_3^B and u_3^D for $\beta = 500,000$.

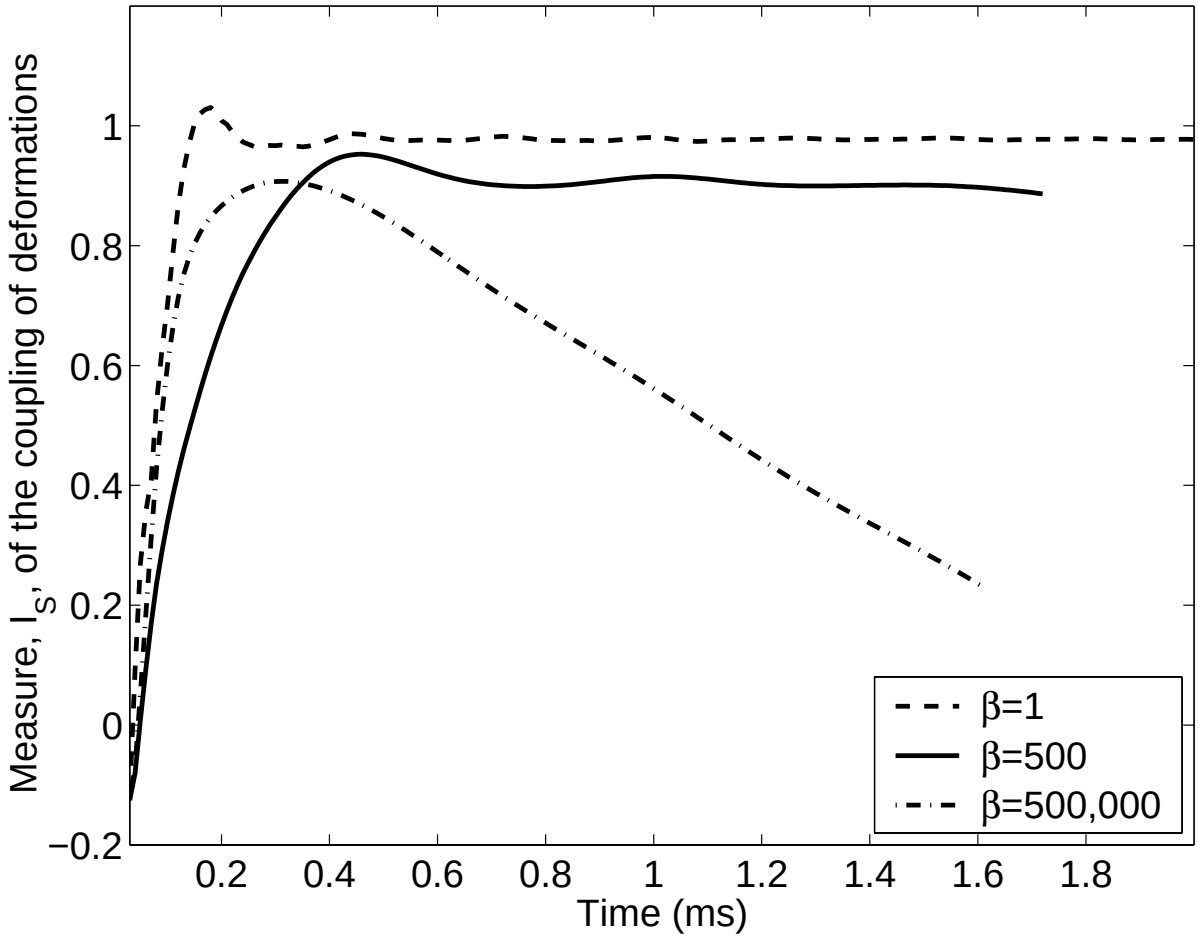

Figure 4.13: Time histories of I_S for three values of β.

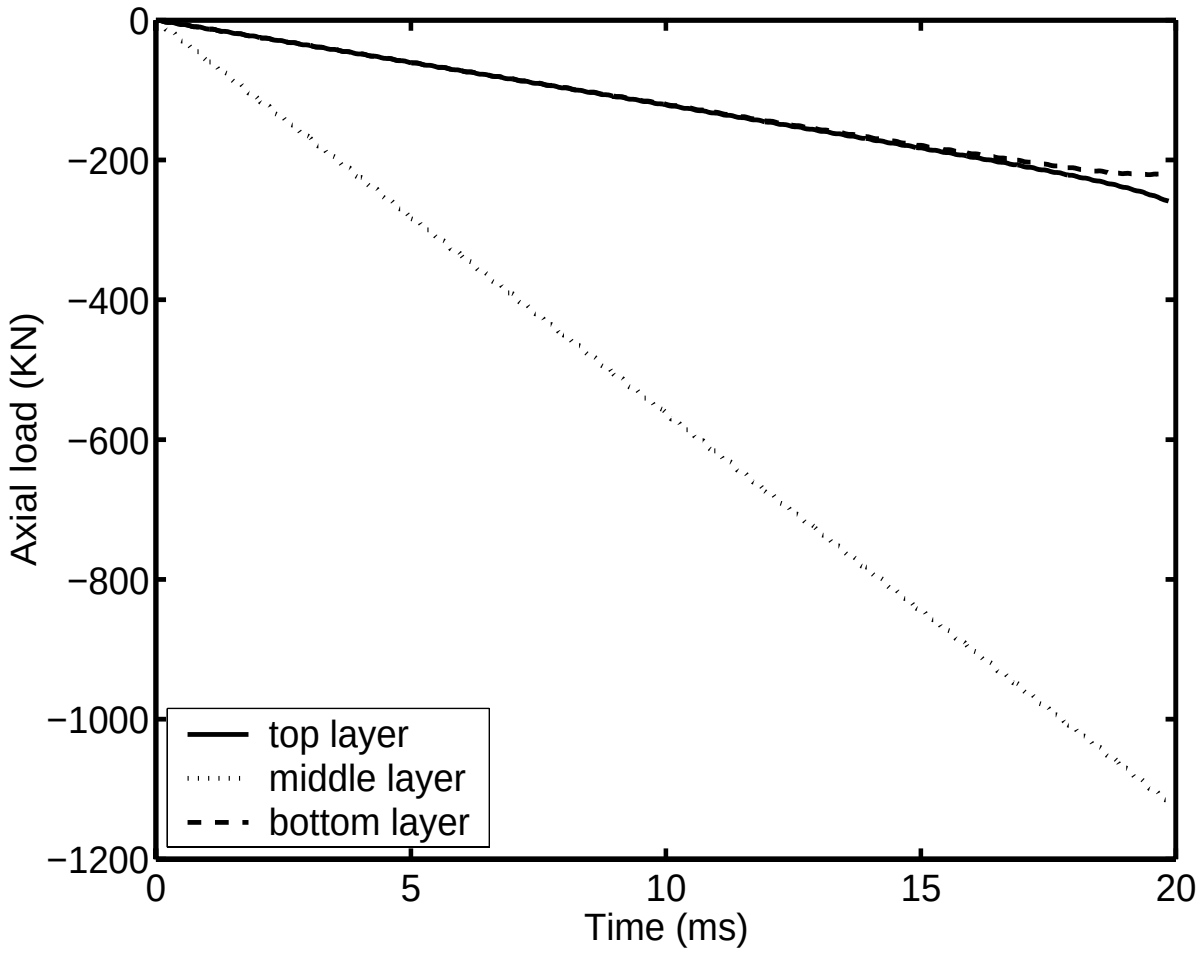

Figure 4.14: Time histories of the axial loads taken by the top, the bottom, and the intermediate layers for $\beta = 1$.

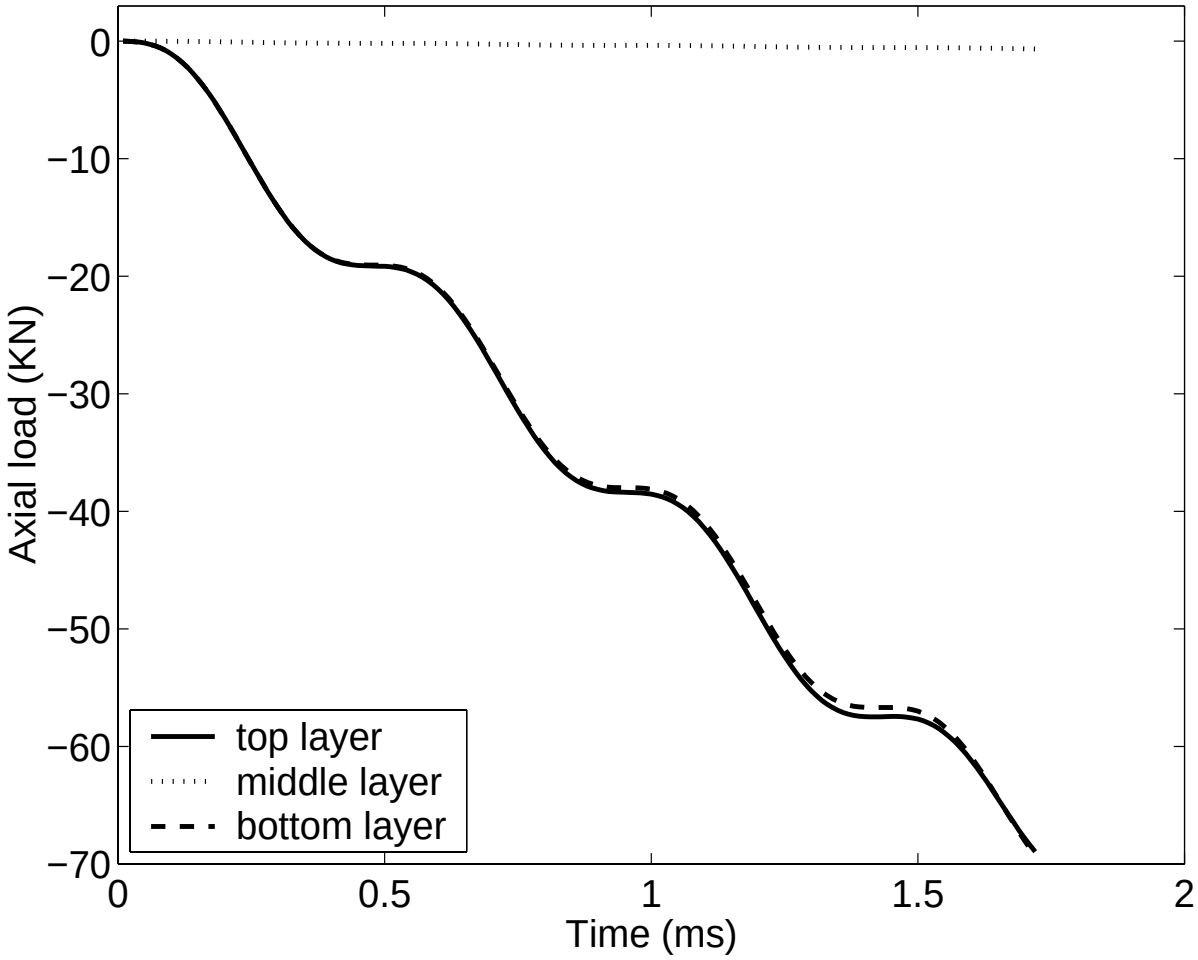

Figure 4.15: Time histories of the axial loads taken by the top, the bottom, and the intermediate layers for $\beta = 500$.

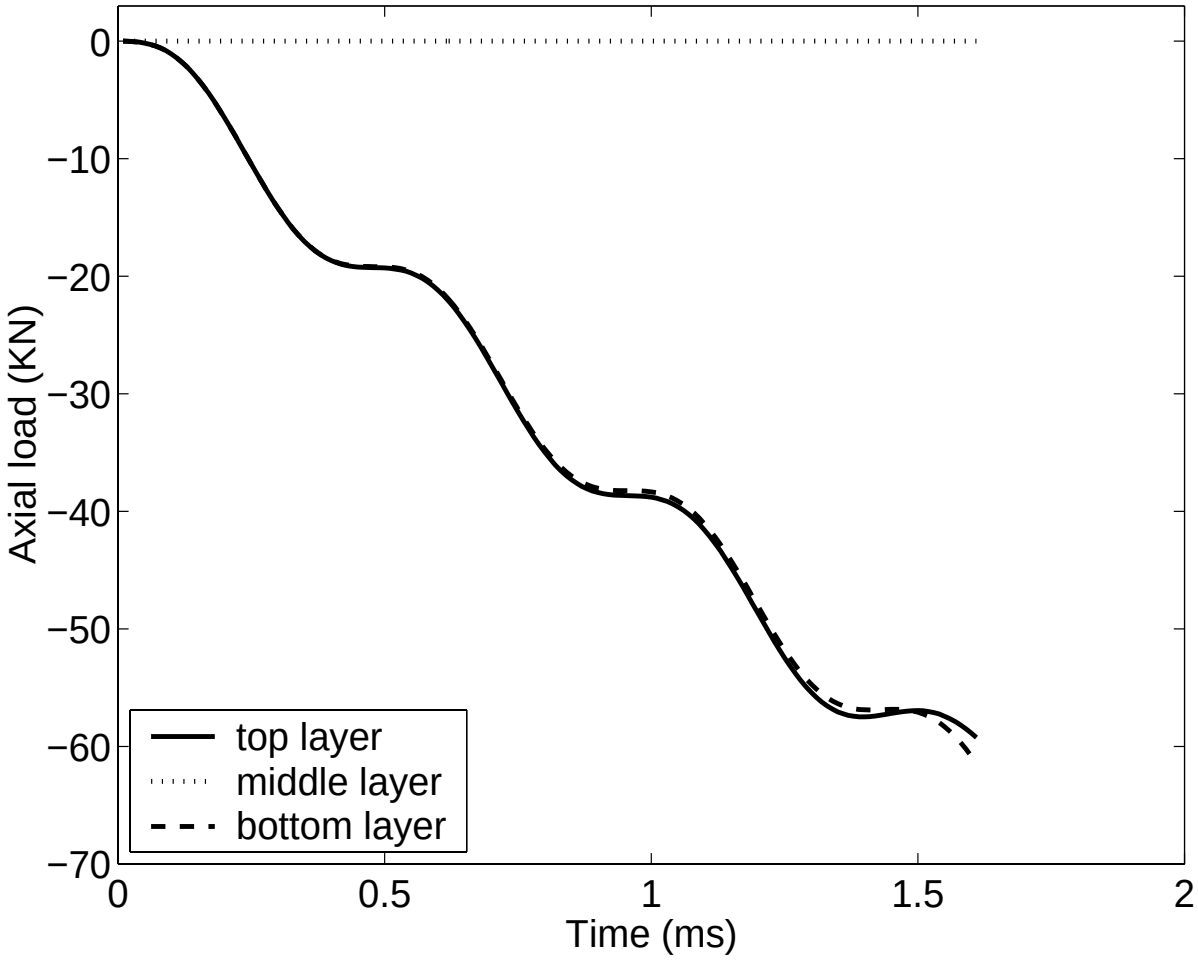

Figure 4.16: Time histories of the axial loads taken by the top, the bottom, and the intermediate layers for $\beta = 500,000$.

Table 3. For $\beta = 5 \times 10^5$, values of u_3^B and u_3^D when $u_3^A = -3$ mm for different thicknesses of the intermediate soft layer.

Thickness of the intermediate soft layer (cm)	u_3^B(mm)	u_3^D(mm)
0.4	-4.081	-3.924
0.6	-3.629	-3.375
0.8	-3.328	-2.974
1.0	-3.101	-2.695
1.2	-2.962	-2.454
1.4	-2.907	-2.231
1.6	-2.829	-2.106
1.8	-2.789	-1.987
2.0	-2.777	-1.899
2.2	-2.782	-1.811

When the thickness of the intermediate layer is increased from 0.6 to 2.2 cm, the transverse displacement of point B decreases by about 30% but that of point D by nearly 55%. Note that for a large thickness of the intermediate layer, it takes less time for point A to deflect by 3 mm.

Time histories of the axial loads taken by the top, the bottom, and the intermediate layers for three values of the thickness of the intermediate layer are plotted in Figs. 4.17-19. From these figures, we can see the load is taken equally by the top and the bottom layers.

Time histories of I_S are plotted in Fig. 4.20 for four values of the intermediate layer thickness. These time histories are virtually identical implying that the thickness of the intermediate layer between 4 mm and 22 mm has no effect on the rate of change of I_S.

Vertical displacements of points B and D for different values of the thickness of the intermediate layer when $\beta = 500$ are listed in Table 4.

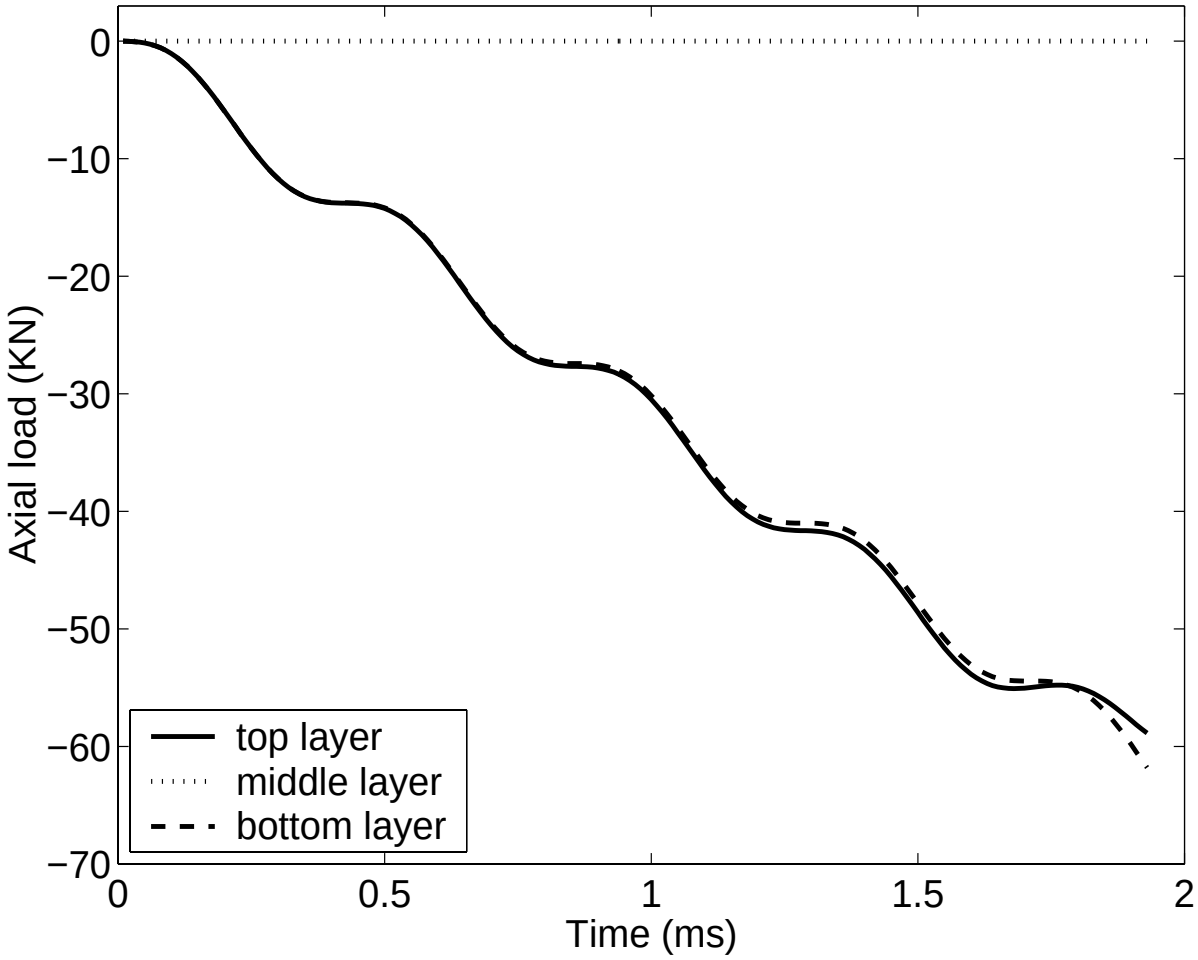

Figure 4.17: Time histories of the axial loads taken by the top, the bottom, and the intermediate layers for the intermediate layer thickness equal to 1.0 cm.

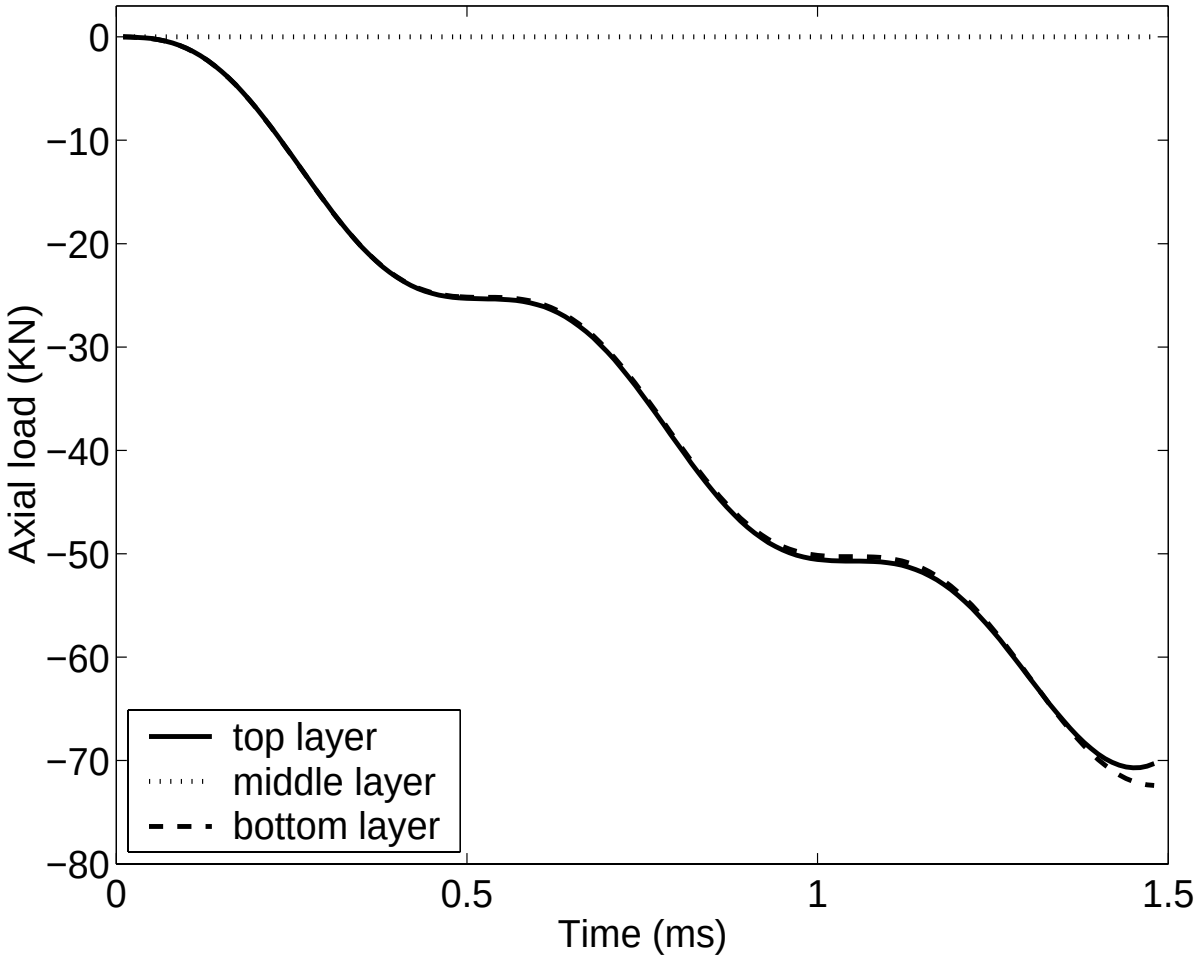

Figure 4.18: Time histories of the axial loads taken by the top, the bottom, and the intermediate layers for the intermediate layer thickness equal to 1.8 cm.

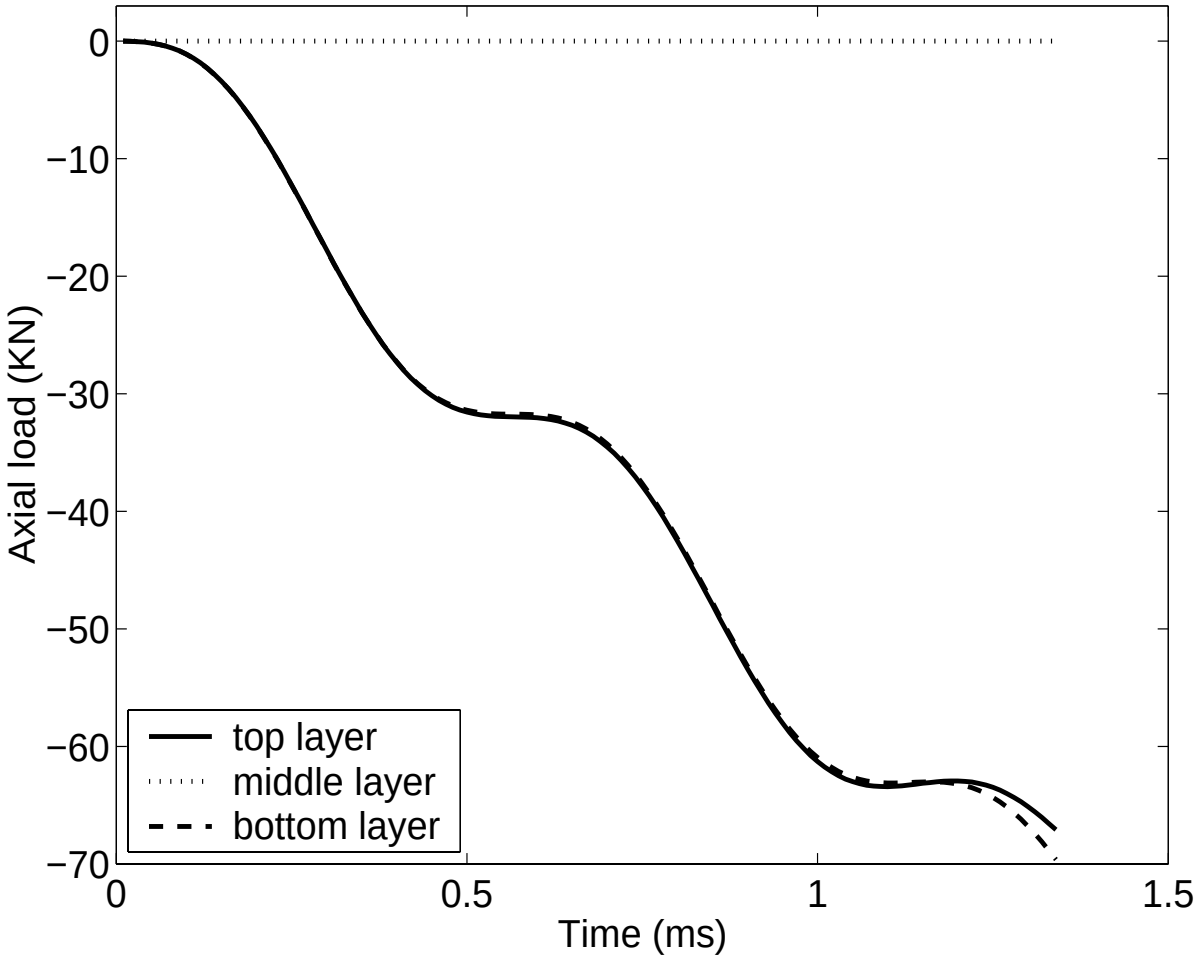

Figure 4.19: Time histories of the axial loads taken by the top, the bottom, and the intermediate layers for the intermediate layer thickness equal to 2.2 cm.

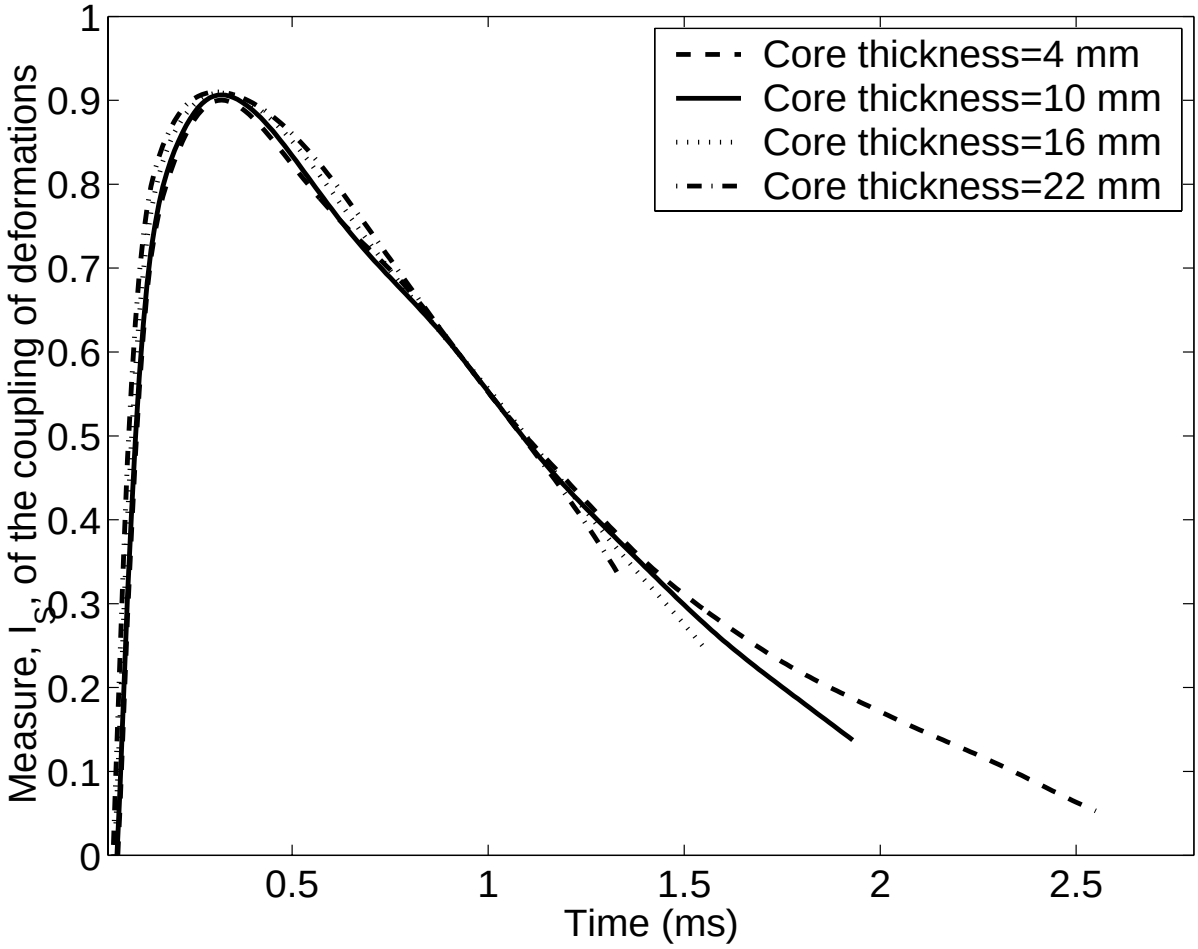

Figure 4.20: For $\beta = 5\times10^5$, time histories of I_S for four values of the intermediate layer thickness.

Table 4. For $\beta = 500$, values of u_3^B and u_3^D when $u_3^A = -3$ mm for different values of the thickness of the intermediate soft layer.

Thickness of the intermediate soft layer (cm)	u_3^B(mm)	u_3^D(mm)
0.4	-3.008	-0.113
1.0	-3.013	-0.245
1.6	-3.008	-0.381
2.2	-2.999	-0.517

When the thickness of the intermediate layer is increased from 0.4 to 2.2 cm, the transverse displacement of point B does not change much but that of point D increases by nearly 450%. Note that u_3^A reaches -3 mm faster for larger thickness of the intermediate layer.

Time histories of I_S are plotted in Fig. 4.21 for different values of the thickness of the intermediate layer.

4.2 Conclusions

Deformations of the top and the bottom layers sandwiching a soft layer start becoming uncoupled when the elastic moduli of the soft layer equal 1/200 of those of the top or the bottom layer and are totally uncoupled when this ratio of the elastic moduli equals 1/500,000. Larger thicknesses of the intermediate layer enhance this uncoupling effect.

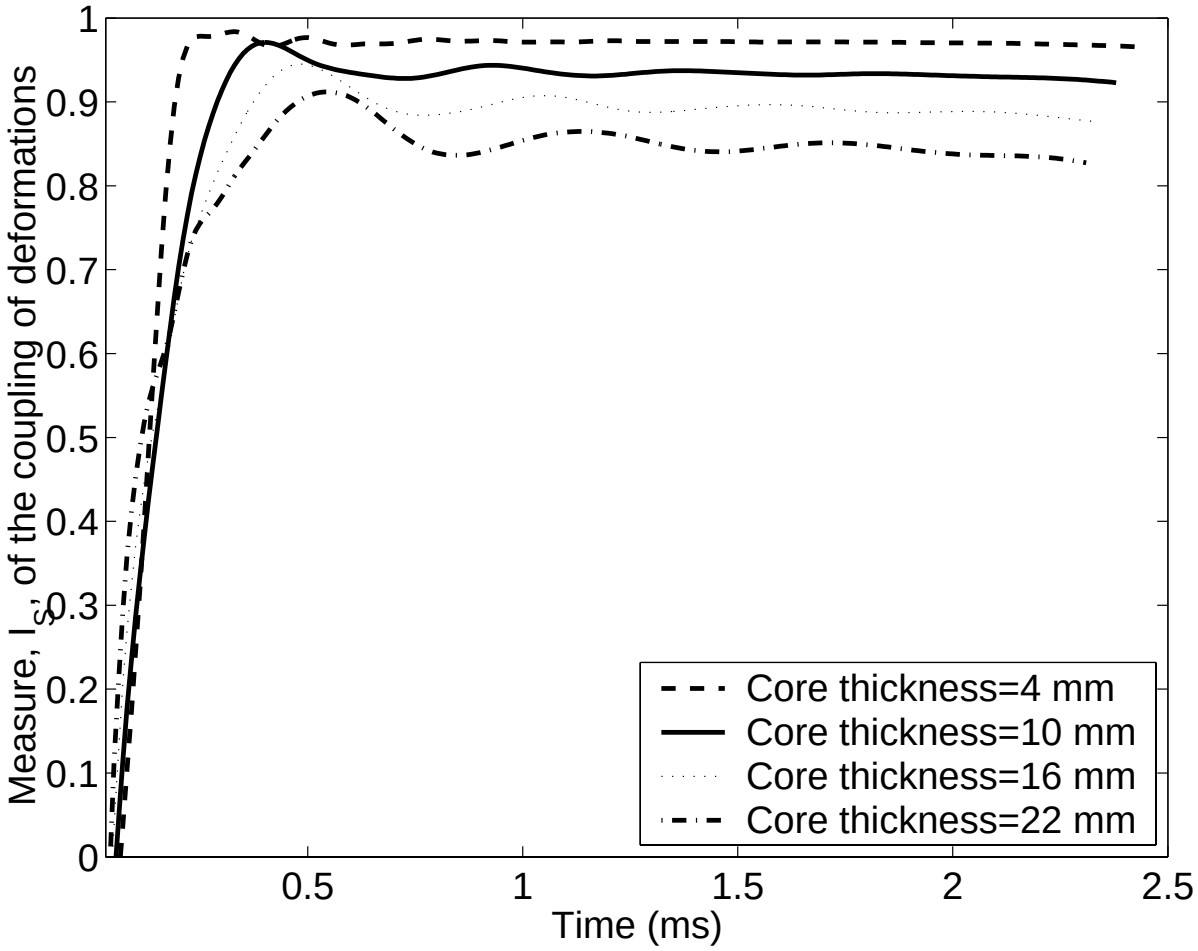

Figure 4.21: For $\beta = 500$, time histories of I_S for four values of the intermediate layer thickness.

Chapter 5

Contributions

The contributions of this study can be summarized as follows:

1. The computer code developed by Batra and Liang for analyzing three dimensional deformations of a piezoelectric body was modified to include viscoelastic effects. For a viscoelastic body, the second Piola-Kirchhoff stress tensor is expressed as a linear functional of the time history of the rate of change of the Green-St. Venant strain tensor.

2. Earlier numerical studies of the buckling enhancement problem by various researchers typically neglected inertia effects and the material and geometric nonlinearities. Here we considered these effects and also introduced a specific buckling criterion.

3. In contrast to the earlier studies of the active constrained layer damping that employed extension mode PZT actuators, we also investigated the enhancement in the energy dissipation caused by the shear mode PZT actuators. We used a three-dimensional continuum theory rather than a plate theory to analyze deformations of a hybrid laminated structure.

Chapter 6

Conclusions

We have used a 3-dimensional geometrically nonlinear theory to investigate the enhancement in the dynamic buckling load of a graphite-epoxy square plate sandwiched between two piezoceramic layers. The simply supported plate is loaded on two opposite edges by equal and opposite in-plane compressive time-dependent tractions with the other two edges kept traction free. The plate material is modeled as neo-Hookean and the piezoceramic by a second-order constitutive relation, i.e., the second Piola-Kirchhoff stress tensor and the electric polarization are expressed as second degree polynomials in the Green-St. Venant strain tensor and the electric field. The plate material is modeled as orthotropic and the PZT as transversely isotropic with the axis of transverse isotropy along the thickness direction. The transient problem is analyzed numerically by using the finite element code developed by Batra and Liang [3]. The plate is taken to have buckled when its centroidal deflection equaled three times the plate thickness.

The dynamic buckling load for the plate is found to strongly depend upon the rate of rise of the applied tractions and hence the inertia effects. With the maximum electric potential difference applied to the PZT layers limited to 1 kV/mm, the buckling load is enhanced by 18.3% when

the PZT elements are activated. For a maximum electric field of 30 kV/mm, the buckling load increased by 58.5%. When only a part of the top and bottom surfaces of the plate can be covered by PZT layers, then square PZT elements give a larger enhancement in the buckling load than rectangular shaped or cross-shaped PZT elements provided that the covered surface area exceeds 60%. Otherwise the cross-shaped and rectangular PZT elements fully covering the square plate in the loading direction result in higher buckling loads than the square shaped PZT actuators.

An increase in the plate thickness relative to that of the PZT layers decreases the effectiveness of the PZTs in enhancing the buckling load for the plate. Of course, design considerations may limit the thickness of the PZT layers that can be used.

Even though we have not verified it, we believe that other definitions of the dynamic buckling load will not alter the qualitative nature of results but may change the magnitude of the gain in the buckling load achieved by activating the PZTs.

We have compared the performance of two active constrained layer damping treatments (ACLD) in a thick laminated plate comprised of layers made of a piezoceramic (PZT) material, aluminum and a viscoelastic material. Effects of geometric nonlinearities and the dependence of stresses and electric displacements upon squares of the electric field are incorporated into the analysis of the problem. In one configuration, the PZT layer is at the center, and it's transverse shear deformations are predominant. In the other configuration, the PZT layers are at the outer surfaces and their extensional deformations are significantly more than their transverse shear deformations. Three-dimensional transient deformations of the composite system are analyzed in the time domain by the finite element method.

For each value of the thickness of the viscoelastic layer, the measure I_1 of energy dissipation for the shear mode PZT configuration is larger than that for the extension mode PZT configuration. It

implies that the shear mode PZTs are more effective in damping out vibrations of the hybrid plate. The energy of electric deformations of the shear mode PZT configuration is more than that of the extension mode configuration.

The maximum transverse shear strain induced in the viscoelastic layer increases with a decrease in it's thickness. The optimum thickness of the viscoelastic layers for maximum total energy dissipation is the same for each set-up. The thickness of the PZT layer which results in the maximum value of the index I_1 of energy dissipation is the same for the two set-ups. Both arrangements result in the largest value of I_1 for a plate of aspect ratio 10. When each viscoelastic layer was divided into four sublayers and values of the relaxation moduli of the sublayers were changed between 0.1 and 0.4 times their instantaneous values, the value of the logarithmic decrement was essentially unaffected. With the objective of simultaneously damping out quickly the first two modes of vibration, each of these four sublayers was assigned a relaxation time equal to the reciprocal of the first four frequencies. These numerical experiments reveal that subdividing each viscoelastic layer into two sublayers and assigning relaxation times to these sublayers equal to the reciprocal of the first two frequencies will damp out rapidly the first two modes of vibration.

Deformations of the top and the bottom layers sandwiching a soft layer start becoming uncoupled when the elastic moduli of the soft layer equal 1/200 of those of the top or the bottom layer and are totally uncoupled when this ratio of the elastic moduli equals 1/500,000. Larger thicknesses of the intermediate layer enhance this uncoupling effect.

Bibliography

[1] Yang J. S. and Batra R. C. (1995). A second-order theory for piezoelectric materials. *Journal of the Acoustical Society of America* **97** (1) 280-288

[2] Crawley E. F. and Anderson E. H. (1990). Detailed models of piezoceramics actuation of beams. *Journal of Intelligent Material Systems and Structures* **1** 4-24

[3] Batra R. C. and Liang X. Q. (1997). Finite dynamic deformations of smart structures. *Computational Mechanics* **20** (5) 427-438

[4] Chandrashekhara K. and Bhatia K. (1993). Active buckling control of smart composite plates - finite-element analysis. *Smart Materials and Structures* **2** 31-39

[5] Murali Krishna M. W. and Mei C. (1992). Finite element buckling and post-buckling analysis of a plate with piezoelectric actuator. *Proceedings of Conference on Recent Advances in Adaptive Sensory Materials and their Applications*, Blacksburg VA 301-313

[6] Thompson D. M. and Griffin O. H. Jr. (1993). Finite element predictions of active buckling control of stiffened panels. *Journal of Intelligent Material Systems and Structures* **4** 243-247

[7] Baz A. and Tempe L. (1989). Active control of buckling of flexible beams. In *Proceedings of ASME Design Technical Conference*, Montreal Canada 211-218

[8] Thompson S. P. and Loughlan J. (1995). The active buckling control of some composite column strips using piezoceramic actuators. *Computers and Structures* **32** 59-67

[9] de Faria A. R. and de Almeida S. F. M. (1999). Enhancement of pre-buckling behavior of composite beams with geometric imperfections using piezoelectric actuators. *Composites B* **30** 43-50

[10] Berlin A. A. and Sussman G. J. (1993). Increasing the compressive strength of a column via active control. In *Proceedings of International Conference on Adaptive Structures*, San Diego, Technomic Publishing Co. Inc., Lancaster PA 208-717.

[11] Meressi T. and Paden B. (1993). Buckling control of a flexible beam using piezoelectric actuators. *Journal of Guidance, Control and Dynamics* **16** 977-980.

[12] Jefferis R. P. (1968). Feedback control of the buckling instability in an axially compressed thin elastic beam. Ph.D. Thesis, Department of Electrical Engineering, University of Pennsylvania.

[13] Berlin A. A. (1995). Active control of buckling using piezoceramic actuators. *Industrial and Commercial Applications of Smart Materials* SPIE Smart Structures and Materials Workshop, San Diego, CA.

[14] Berlin A. A., Chase J. G., Yim M., Maclean B. J., Olivier M. and Jacobsen S. C. (1988). MEMS-based control of structural dynamic instability. *Journal of Intelligent Material Systems and Structures* **9** 574-586.

[15] Petry D. and Fahlbusch G. (2000). Dynamic buckling of thin isotropic plates subjected to in-plane impact. *Thin-Walled Structures* **38** 267-283.

[16] Budiansky B. and Hutchinson J. W. (1964). Dynamic buckling of imperfection-sensitive structures. *Proceedings of the 11th International Congress of Applied Mechanics*, Berlin, Springer 636-651.

[17] Cui S., Hao H. and Cheong H. K. (2001). Numerical analysis of dynamic buckling of rectangular plates subjected to intermediate-velocity impact. *International Journal of Impact Engineering* **25** 147-167.

[18] Batra R. C. (2000). Comparison of results from four linear constitutive relations in isotropic finite elasticity. *International Journal of Nonlinear Mechanics* **36** 29-40.

[19] Batra R. C. and Yang J. (1995). Second order constitutive relations for transversely isotropic porous piezoelectric materials. *Journal of the Acoustical Society of America* **97** 2595-2598.

[20] Hughes T. J. R. (1987). *The Finite Element Method, Linear Static and Dynamic Finite Element Analysis*, Prentice-Hall, Englewood NJ.

[21] Weller T., Abrmovich H. and Yaffe R. (1989). Dynamic buckling of beams and plates subjected to axial impact. *Computers and Structures* **32** (3/4) 835-851.

[22] Tiersten H. F. (1993). Electroelastic equations for electroded thin plates subjected to large driving voltages. *Journal of Applied Physics* **74** 3389-3393.

[23] Batra R. C. and Liang X. Q. (1996). Shape control of vibrating simply supported rectangular plates. *American Institute of Aeronautics and Astronautics Journal* **34** (1) 116-122

[24] Azvine, B., Tomlinson, G. and Wynne, R. (1994). Initial studies into the use of active constrained-layer damping for controlling resonant vibrations. *Proc. of Smart Structures and Materials Conference on Passive Damping*, C. Johnson ed., **2193**: 138-149, Orlando, Florida.

[25] Bailey, T., Gruzen, A. and Madden, P. (1988). RCS/piezoelectric distributed actuator study. AFAL-TR-88-038.

[26] Batra, R. C. and Yu, J.-H. (1999). Linear constitutive relations in isotropic finite viscoelasticity. *Journal of Elasticity*, **55**: 73-77.

[27] Batra, R. C. and Liang, X. Q. (1997). Finite dynamic deformations of smart structures. *Computational Mechanics*, **20**: 427-438.

[28] Baz, A. (1993). Active constrained layer damping. *DAMPING'93 Conference*, San Francisco, CA, pp. IBB 1-23.

[29] Baz, A. and Ro, J. (1993). Partial treatment of flexible beams with active constrained layer damping. *Annual Technical Meeting of the Engineering Sciences Society*, ASME-AMD-Vol. 167, pp. 61-80, Charlottesville, VA.

[30] Baz, A. and Ro, J. (1993). Finite element modeling and performance of active constrained layer damping. *Ninth VPI&SU Conference on Dynamics & Control of Large Structures*, pp. 345-358, Blacksburg, VA.

[31] Baz, A. and Ro., J. (1995). Performance characteristics of active constrained layer damping. *Shock and Vibration*, **2**: 33-42.

[32] Baz, A. and Ro., J. (1995). Optimum design and control of active constrained layer damping. *ASME Journal of Vibration and Acoustics*, **117**: 135-144.

[33] Boriseiko, V. A., Martynenko, V. S. and Ulitko, A. F., (1983). General Theory of Thin Piezoceramic Shells. Vestnik Kiev. Univ., *Mat. i Mekh.*, **25**, 26-40 (in Ukrainian).

[34] Cheng, Z. Q. and Batra, R. C. (2000). Three dimensional asymptotic analysis of multiple-electroded piezoelectric laminates. *American Institute of Aeronautics and Astronautics Journal*, **38**: 317-324.

[35] Christensen, R. M. (1971). *Theory of Viscoelasticity, An Introduction*, Academic Press, New York.

[36] Crawley, E. F. and Anderson, E. H. (1990). Detailed models of piezoceramic actuation of beams. *Journal of Intelligent Material Systems and Structures*, **1**: 4-24.

[37] DiTaranto, R. A. (1965). Theory of vibratory bending for elastic and viscoelastic layered finite length beams. *ASME Journal of Applied Mechanics*, **87**: 881-886.

[38] Edberg, D. and Bicos, A. (1992). Design and development of passive and active damping concepts for adaptive structures. *Conference on Active Materials and Adaptive Structures*, G. Knowles, ed., IoP Publishing Ltd., Bristol, UK, pp. 377-382.

[39] Mead, D. J. and Markus, S. (1969). The forced vibration of a three-layer, damped sandwich beam with arbitrary boundary conditions. *Journal of Sound and Vibration*, **10**: 163-175.

[40] Nostrand, W. C. (1994). Active constrained layer damping using PZT actuators. Ph.D. Dissertation, State University of New York at Buffalo.

[41] Liao, W. H. and Wang, K. W. (1995). On the active-passive hybrid vibration control actions of structures with active constrained layer treatments. *Proc. Design Eng'g Tech'l Conf.*, ASME DE84-3, 125-151.

[42] Liao, W. H. and Wang, K. W. (1997). On the analysis of viscoelastic materials for active constrained layer treatments. *Journal of Sound and Vibration*, **207**: 319-334.

[43] Plump, J. and Hubbard, J. E. (1986). Modeling of an active constrained layer damper. *Twelveth International Congress on Acoustics*, Paper #D41, Toronto, Canada, July 24-31.

[44] Shen, I. Y. (1994). Hybrid damping through intelligent constrained layer treatments. *ASME Journal of Vibration and Acoustics*, **116**: 341-349.

[45] Srinivas, S. and Rao, A. K. (1970). Bending, vibration and buckling of simply supported thick orthotropic rectangular plates and laminates. *International Journal of Solids and Structures*, **6**: 1463-1481.

[46] Sun, C. T. and Zhang, X. D. (1996). Formulation of an adaptive sandwich beam," *Smart Materials and Structures*, **5**: 814-823.

[47] Tiersten, H. F. (1975). Nonlinear electroelastic equations cubic in small field variables. *Journal of Acoustical Society of America*, **57**: 660-666.

[48] Timoshenko, S. (1993). *Vibration Problems in Engineering*, Butterworth, Heinemann, Oxford.

[49] Van Nostrand, W., Knowles, G. and Inman, D. (1994). Finite element modeling for active constrained-layer damping. *Proc. of Smart Structures and Materials Conference on Passive Damping*, C. Johnson, ed., **2193**, pp. 126-137, Orlando, Florida.

[50] Vel, S. S. and Batra, R. C. (2001). Exact solution for the cylindrical bending of laminated plates with embedded shear actuators. *Smart Materials & Structures*, **10**: 240-251.

[51] Vel, S. S. and Batra, R. C. (2001). Exact solution for rectangular sandwich plates with embedded piezoelectric shear actuators. *American Institute of Aeronautics and Astronautics Journal*, **39**: 1363-1373.

[52] Vel, S. S. and Batra, R. C. (2001). Analysis of piezoelectric bimorphs and plates with segmented actuators. *Thin-Walled Structures*, **39**: 23-44.

[53] Vidoli, S. and Batra, R. C. (2000). Derivation of plate and rod equations for a piezoelectric body from a mixed three-dimensional variational principle. *Journal of Elasticity*, **59**:23-50.

[54] Vidoli, S. and Batra, R. C. (2001). Coupled extensional and torsional deformations of a piezoelectric cylinder. *Smart Materials & Structures*, **10**: 300-304.

[55] Yang, J.S. and Batra, R. C. (1995). A second-order theory of piezoelectric materials, *Journal of Acoustical Society of America*, **97**: 280-288.

[56] Yu, J.-H. and Batra, R. C. (2000). Constrained layer damping in finite shearing deformations. *Journal of Sound & Vibration*, **229**: 879-895.

[57] Zhang, X. D. and Sun, C. T. (1999). Analysis of a sandwich plate containing a piezoelectric core. *Smart Materials and Structures*, **8**: 31-40.

[58] Mason, W. P. (1981). Piezoelectricity, its history and applications. *Journal of Acoustical Society of America*, **70**: (6) 1561-1566.

[59] Lok, Tat-Seng and Cheng, Qian-Hua (2001). Free and forced vibration of simply supported, orthotropic sandwich panel. *Computers and Structures*, **79**: 301-312.

[60] Hao, B., Cho, C. and Lee, S. W. (2000). Buckling and postbuckling of soft-core sandwich plates with composite facesheets. *Computational Mechanics*, **25**: 421-429.

[61] Sokolinsky, V. and Frostig, Y. (1999). Boundary condition effects in buckling of ”soft” core sandwich panels. *Journal of Engineering Mechanics*, **125**: (8) 865-874.

[62] Frostig, Y. and Sokolinsky, V. (2000). Higher-order buckling of debonded (delaminated) sandwich panels with soft core. *American Institute of Aeronautics and Astronautics Journal*, **38**: (11) 2147-2159.

Vita

Twzen-Shang Geng was born on October 31, 1964 in Taipei, Taiwan. He joined the Civil Engineering Department at Cheng-Kung University, Tainan, Taiwan in August 1983 and received his Bachelor of Science degree in June 1987. From September 1987 till August 1989 he worked as a construction engineer in Chinese Army. From September 1989 till June 1990 he worked as a construction engineer in Bureau of Engineering Service. In September 1990, he joined the Civil Engineering Department at Colorado State University and earned a Master of Science degree in May 1993. In January 1995 he enrolled in the doctoral program in the Engineering Science and Mechanics Department at Virginia Tech and successfully defended his dissertation on April 9, 2002, to earn a Doctor of Philosophy degree in Engineering Science and Mechanics.